

# Measurement of the Top Quark Mass with the Collider Detector at Fermilab

T. Affolder,<sup>21</sup> H. Akimoto,<sup>43</sup> A. Akopian,<sup>36</sup> M. G. Albrow,<sup>10</sup> P. Amaral,<sup>7</sup>  
 S. R. Amendolia,<sup>32</sup> D. Amidei,<sup>24</sup> K. Anikeev,<sup>22</sup> J. Antos,<sup>1</sup> G. Apollinari,<sup>10</sup>  
 T. Arisawa,<sup>43</sup> T. Asakawa,<sup>41</sup> W. Ashmanskas,<sup>7</sup> M. Atac,<sup>10</sup> F. Azfar,<sup>29</sup> P. Azzi-  
 Bacchetta,<sup>30</sup> N. Bacchetta,<sup>30</sup> M. W. Bailey,<sup>26</sup> S. Bailey,<sup>14</sup> P. de Barbaro,<sup>35</sup>  
 A. Barbaro-Galtieri,<sup>21</sup> V. E. Barnes,<sup>34</sup> B. A. Barnett,<sup>17</sup> M. Barone,<sup>12</sup>  
 G. Bauer,<sup>22</sup> F. Bedeschi,<sup>32</sup> S. Belforte,<sup>40</sup> G. Bellettini,<sup>32</sup> J. Bellinger,<sup>44</sup>  
 D. Benjamin,<sup>9</sup> J. Bensinger,<sup>4</sup> A. Beretvas,<sup>10</sup> J. P. Berge,<sup>10</sup> J. Berryhill,<sup>7</sup>  
 B. Bevensee,<sup>31</sup> A. Bhatti,<sup>36</sup> M. Binkley,<sup>10</sup> D. Bisello,<sup>30</sup> R. E. Blair,<sup>2</sup>  
 C. Blocker,<sup>4</sup> K. Bloom,<sup>24</sup> B. Blumenfeld,<sup>17</sup> S. R. Blusk,<sup>35</sup> A. Bocci,<sup>32</sup>  
 A. Bodek,<sup>35</sup> W. Bokhari,<sup>31</sup> G. Bolla,<sup>34</sup> Y. Bonushkin,<sup>5</sup> D. Bortoletto,<sup>34</sup> J.  
 Boudreau,<sup>33</sup> A. Brandl,<sup>26</sup> S. van den Brink,<sup>17</sup> C. Bromberg,<sup>25</sup> M. Brozovic,<sup>9</sup>  
 N. Bruner,<sup>26</sup> E. Buckley-Geer,<sup>10</sup> J. Budagov,<sup>8</sup> H. S. Budd,<sup>35</sup> K. Burkett,<sup>14</sup>  
 G. Busetto,<sup>30</sup> A. Byon-Wagner,<sup>10</sup> K. L. Byrum,<sup>2</sup> P. Calafiura,<sup>21</sup> M. Campbell,<sup>24</sup>  
 W. Carithers,<sup>21</sup> J. Carlson,<sup>24</sup> D. Carlsmith,<sup>44</sup> J. Cassada,<sup>35</sup> A. Castro,<sup>30</sup>  
 D. Cauz,<sup>40</sup> A. Cerri,<sup>32</sup> A. W. Chan,<sup>1</sup> P. S. Chang,<sup>1</sup> P. T. Chang,<sup>1</sup> J. Chapman,<sup>24</sup>  
 C. Chen,<sup>31</sup> Y. C. Chen,<sup>1</sup> M. -T. Cheng,<sup>1</sup> M. Chertok,<sup>38</sup> G. Chiarelli,<sup>32</sup>  
 I. Chirikov-Zorin,<sup>8</sup> G. Chlachidze,<sup>8</sup> F. Chlebana,<sup>10</sup> L. Christofek,<sup>16</sup>  
 M. L. Chu,<sup>1</sup> Y. S. Chung,<sup>35</sup> C. I. Ciobanu,<sup>27</sup> A. G. Clark,<sup>13</sup> A. Connolly,<sup>21</sup>  
 J. Conway,<sup>37</sup> J. Cooper,<sup>10</sup> M. Cordelli,<sup>12</sup> J. Cranshaw,<sup>39</sup> D. Cronin-Hennessy,<sup>9</sup>  
 R. Cropp,<sup>23</sup> R. Culbertson,<sup>7</sup> D. Dagenhart,<sup>42</sup> F. DeJongh,<sup>10</sup> S. Dell'Agnello,<sup>12</sup>  
 M. Dell'Orso,<sup>32</sup> R. Demina,<sup>10</sup> L. Demortier,<sup>36</sup> M. Deninno,<sup>3</sup> P. F. Derwent,<sup>10</sup>  
 T. Devlin,<sup>37</sup> J. R. Dittmann,<sup>10</sup> S. Donati,<sup>32</sup> J. Done,<sup>38</sup> T. Dorigo,<sup>14</sup> N. Eddy,<sup>16</sup>  
 K. Einsweiler,<sup>21</sup> J. E. Elias,<sup>10</sup> E. Engels, Jr.,<sup>33</sup> W. Erdmann,<sup>10</sup> D. Errede,<sup>16</sup>  
 S. Errede,<sup>16</sup> Q. Fan,<sup>35</sup> R. G. Feild,<sup>45</sup> C. Ferretti,<sup>32</sup> R. D. Field,<sup>11</sup> I. Fiori,<sup>3</sup>  
 B. Flaughner,<sup>10</sup> G. W. Foster,<sup>10</sup> M. Franklin,<sup>14</sup> J. Freeman,<sup>10</sup> J. Friedman,<sup>22</sup>  
 Y. Fukui,<sup>20</sup> I. Furic,<sup>22</sup> S. Galeotti,<sup>32</sup> M. Gallinaro,<sup>36</sup> T. Gao,<sup>31</sup> M. Garcia-

Sciveres,<sup>21</sup> A. F. Garfinkel,<sup>34</sup> P. Gatti,<sup>30</sup> C. Gay,<sup>45</sup> S. Geer,<sup>10</sup> D. W. Gerdes,<sup>24</sup>  
 P. Giannetti,<sup>32</sup> P. Giromini,<sup>12</sup> V. Glagolev,<sup>8</sup> M. Gold,<sup>26</sup> J. Goldstein,<sup>10</sup>  
 A. Gordon,<sup>14</sup> A. T. Goshaw,<sup>9</sup> Y. Gotra,<sup>33</sup> K. Goulianos,<sup>36</sup> C. Green,<sup>34</sup>  
 L. Groer,<sup>37</sup> C. Grosso-Pilcher,<sup>7</sup> M. Guenther,<sup>34</sup> G. Guillian,<sup>24</sup> J. Guimaraes  
 da Costa,<sup>14</sup> R. S. Guo,<sup>1</sup> R. M. Haas,<sup>11</sup> C. Haber,<sup>21</sup> E. Hafen,<sup>22</sup> S. R. Hahn,<sup>10</sup>  
 C. Hall,<sup>14</sup> T. Handa,<sup>15</sup> R. Handler,<sup>44</sup> W. Hao,<sup>39</sup> F. Happacher,<sup>12</sup> K. Hara,<sup>41</sup>  
 A. D. Hardman,<sup>34</sup> R. M. Harris,<sup>10</sup> F. Hartmann,<sup>18</sup> K. Hatakeyama,<sup>36</sup>  
 J. Hauser,<sup>5</sup> J. Heinrich,<sup>31</sup> A. Heiss,<sup>18</sup> M. Herndon,<sup>17</sup> B. Hinrichsen,<sup>23</sup>  
 K. D. Hoffman,<sup>34</sup> C. Holck,<sup>31</sup> R. Hollebeek,<sup>31</sup> L. Holloway,<sup>16</sup> R. Hughes,<sup>27</sup>  
 J. Huston,<sup>25</sup> J. Huth,<sup>14</sup> H. Ikeda,<sup>41</sup> J. Incandela,<sup>10</sup> G. Introzzi,<sup>32</sup> J. Iwai,<sup>43</sup>  
 Y. Iwata,<sup>15</sup> E. James,<sup>24</sup> H. Jensen,<sup>10</sup> M. Jones,<sup>31</sup> U. Joshi,<sup>10</sup> H. Kambara,<sup>13</sup>  
 T. Kamon,<sup>38</sup> T. Kaneko,<sup>41</sup> K. Karr,<sup>42</sup> H. Kasha,<sup>45</sup> Y. Kato,<sup>28</sup> T. A. Keaffaber,<sup>34</sup>  
 K. Kelley,<sup>22</sup> M. Kelly,<sup>24</sup> R. D. Kennedy,<sup>10</sup> R. Kephart,<sup>10</sup> D. Khazins,<sup>9</sup>  
 T. Kikuchi,<sup>41</sup> B. Kilminster,<sup>35</sup> M. Kirby,<sup>9</sup> M. Kirk,<sup>4</sup> B. J. Kim,<sup>19</sup> D. H. Kim,<sup>19</sup>  
 H. S. Kim,<sup>16</sup> M. J. Kim,<sup>19</sup> S. H. Kim,<sup>41</sup> Y. K. Kim,<sup>21</sup> L. Kirsch,<sup>4</sup>  
 S. Klimenko,<sup>11</sup> P. Koehn,<sup>27</sup> A. Köngeter,<sup>18</sup> K. Kondo,<sup>43</sup> J. Konigsberg,<sup>11</sup>  
 K. Kordas,<sup>23</sup> A. Korn,<sup>22</sup> A. Korytov,<sup>11</sup> E. Kovacs,<sup>2</sup> J. Kroll,<sup>31</sup> M. Kruse,<sup>35</sup>  
 S. E. Kuhlmann,<sup>2</sup> K. Kurino,<sup>15</sup> T. Kuwabara,<sup>41</sup> A. T. Laasanen,<sup>34</sup> N. Lai,<sup>7</sup>  
 S. Lami,<sup>36</sup> S. Lammel,<sup>10</sup> J. I. Lamoureux,<sup>4</sup> M. Lancaster,<sup>21</sup> G. Latino,<sup>32</sup>  
 T. LeCompte,<sup>2</sup> A. M. Lee IV,<sup>9</sup> K. Lee,<sup>39</sup> S. Leone,<sup>32</sup> J. D. Lewis,<sup>10</sup>  
 M. Lindgren,<sup>5</sup> T. M. Liss,<sup>16</sup> J. B. Liu,<sup>35</sup> Y. C. Liu,<sup>1</sup> N. Lockyer,<sup>31</sup> J. Loken,<sup>29</sup>  
 M. Loreti,<sup>30</sup> D. Lucchesi,<sup>30</sup> P. Lukens,<sup>10</sup> S. Lusin,<sup>44</sup> L. Lyons,<sup>29</sup> J. Lys,<sup>21</sup>  
 R. Madrak,<sup>14</sup> K. Maeshima,<sup>10</sup> P. Maksimovic,<sup>14</sup> L. Malferrari,<sup>3</sup> M. Mangano,<sup>32</sup>  
 M. Mariotti,<sup>30</sup> G. Martignon,<sup>30</sup> A. Martin,<sup>45</sup> J. A. J. Matthews,<sup>26</sup>  
 J. Mayer,<sup>23</sup> P. Mazzanti,<sup>3</sup> K. S. McFarland,<sup>35</sup> P. McIntyre,<sup>38</sup> E. McKigney,<sup>31</sup>  
 M. Menguzzato,<sup>30</sup> A. Menzione,<sup>32</sup> C. Mesropian,<sup>36</sup> A. Meyer,<sup>7</sup> T. Miao,<sup>10</sup>  
 R. Miller,<sup>25</sup> J. S. Miller,<sup>24</sup> H. Minato,<sup>41</sup> S. Miscetti,<sup>12</sup> M. Mishina,<sup>20</sup>  
 G. Mitselmakher,<sup>11</sup> N. Moggi,<sup>3</sup> E. Moore,<sup>26</sup> R. Moore,<sup>24</sup> Y. Morita,<sup>20</sup>  
 M. Mulhearn,<sup>22</sup> A. Mukherjee,<sup>10</sup> T. Muller,<sup>18</sup> A. Munar,<sup>32</sup> P. Murat,<sup>10</sup>

S. Murgia,<sup>25</sup> M. Musy,<sup>40</sup> J. Nachtman,<sup>5</sup> S. Nahn,<sup>45</sup> H. Nakada,<sup>41</sup> T. Nakaya,<sup>7</sup>  
 I. Nakano,<sup>15</sup> C. Nelson,<sup>10</sup> D. Neuberger,<sup>18</sup> C. Newman-Holmes,<sup>10</sup> C.-  
 Y. P. Ngan,<sup>22</sup> P. Nicolaidi,<sup>40</sup> H. Niu,<sup>4</sup> L. Nodulman,<sup>2</sup> A. Nomerotski,<sup>11</sup>  
 S. H. Oh,<sup>9</sup> T. Ohmoto,<sup>15</sup> T. Ohsugi,<sup>15</sup> R. Oishi,<sup>41</sup> T. Okusawa,<sup>28</sup>  
 J. Olsen,<sup>44</sup> W. Orejudos,<sup>21</sup> C. Pagliarone,<sup>32</sup> F. Palmonari,<sup>32</sup> R. Paoletti,<sup>32</sup>  
 V. Papadimitriou,<sup>39</sup> S. P. Pappas,<sup>45</sup> D. Partos,<sup>4</sup> J. Patrick,<sup>10</sup> G. Pauletta,<sup>40</sup>  
 M. Paulini,<sup>21</sup> C. Paus,<sup>22</sup> L. Pescara,<sup>30</sup> T. J. Phillips,<sup>9</sup> G. Piacentino,<sup>32</sup>  
 K. T. Pitts,<sup>16</sup> R. Plunkett,<sup>10</sup> A. Pompos,<sup>34</sup> L. Pondrom,<sup>44</sup> G. Pope,<sup>33</sup>  
 M. Popovic,<sup>23</sup> F. Prokoshin,<sup>8</sup> J. Proudfoot,<sup>2</sup> F. Ptohos,<sup>12</sup> O. Pukhov,<sup>8</sup>  
 G. Punzi,<sup>32</sup> K. Ragan,<sup>23</sup> A. Rakitine,<sup>22</sup> D. Reher,<sup>21</sup> A. Reichold,<sup>29</sup> W. Riegler,<sup>14</sup>  
 A. Ribon,<sup>30</sup> F. Rimondi,<sup>3</sup> L. Ristori,<sup>32</sup> W. J. Robertson,<sup>9</sup> A. Robinson,<sup>23</sup>  
 T. Rodrigo,<sup>6</sup> S. Rolli,<sup>42</sup> L. Rosenson,<sup>22</sup> R. Roser,<sup>10</sup> R. Rossin,<sup>30</sup> A. Safonov,<sup>36</sup>  
 W. K. Sakumoto,<sup>35</sup> D. Saltzberg,<sup>5</sup> A. Sansoni,<sup>12</sup> L. Santi,<sup>40</sup> H. Sato,<sup>41</sup>  
 P. Savard,<sup>23</sup> P. Schlabach,<sup>10</sup> E. E. Schmidt,<sup>10</sup> M. P. Schmidt,<sup>45</sup> M. Schmitt,<sup>14</sup>  
 L. Scodellaro,<sup>30</sup> A. Scott,<sup>5</sup> A. Scribano,<sup>32</sup> S. Segler,<sup>10</sup> S. Seidel,<sup>26</sup> Y. Seiya,<sup>41</sup>  
 A. Semenov,<sup>8</sup> F. Semeria,<sup>3</sup> T. Shah,<sup>22</sup> M. D. Shapiro,<sup>21</sup> P. F. Shepard,<sup>33</sup>  
 T. Shibayama,<sup>41</sup> M. Shimojima,<sup>41</sup> M. Shochet,<sup>7</sup> J. Siegrist,<sup>21</sup> G. Signorelli,<sup>32</sup>  
 A. Sill,<sup>39</sup> P. Sinervo,<sup>23</sup> P. Singh,<sup>16</sup> A. J. Slaughter,<sup>45</sup> K. Sliwa,<sup>42</sup> C. Smith,<sup>17</sup>  
 F. D. Snider,<sup>10</sup> A. Solodsky,<sup>36</sup> J. Spalding,<sup>10</sup> T. Speer,<sup>13</sup> P. Sphicas,<sup>22</sup>  
 F. Spinella,<sup>32</sup> M. Spiropulu,<sup>14</sup> L. Spiegel,<sup>10</sup> J. Steele,<sup>44</sup> A. Stefanini,<sup>32</sup>  
 J. Strologas,<sup>16</sup> F. Strumia,<sup>13</sup> D. Stuart,<sup>10</sup> K. Sumorok,<sup>22</sup> T. Suzuki,<sup>41</sup>  
 T. Takano,<sup>28</sup> R. Takashima,<sup>15</sup> K. Takikawa,<sup>41</sup> P. Tamburello,<sup>9</sup> M. Tanaka,<sup>41</sup>  
 B. Tannenbaum,<sup>5</sup> W. Taylor,<sup>23</sup> M. Tecchio,<sup>24</sup> P. K. Teng,<sup>1</sup> K. Terashi,<sup>36</sup>  
 S. Tether,<sup>22</sup> D. Theriot,<sup>10</sup> R. Thurman-Keup,<sup>2</sup> P. Tipton,<sup>35</sup> S. Tkaczyk,<sup>10</sup>  
 K. Tollefson,<sup>35</sup> A. Tollestrup,<sup>10</sup> H. Toyoda,<sup>28</sup> W. Trischuk,<sup>23</sup> J. F. de Troconiz,<sup>14</sup>  
 J. Tseng,<sup>22</sup> N. Turini,<sup>32</sup> F. Ukegawa,<sup>41</sup> T. Vaiciulis,<sup>35</sup> J. Valls,<sup>37</sup> S. Vej-  
 cik III,<sup>10</sup> G. Velev,<sup>10</sup> R. Vidal,<sup>10</sup> R. Vilar,<sup>6</sup> I. Volobouev,<sup>21</sup> D. Vucinic,<sup>22</sup>  
 R. G. Wagner,<sup>2</sup> R. L. Wagner,<sup>10</sup> J. Wahl,<sup>7</sup> N. B. Wallace,<sup>37</sup> A. M. Walsh,<sup>37</sup>  
 C. Wang,<sup>9</sup> C. H. Wang,<sup>1</sup> M. J. Wang,<sup>1</sup> T. Watanabe,<sup>41</sup> D. Waters,<sup>29</sup> T. Watts,<sup>37</sup>

R. Webb,<sup>38</sup> H. Wenzel,<sup>18</sup> W. C. Wester III,<sup>10</sup> A. B. Wicklund,<sup>2</sup> E. Wicklund,<sup>10</sup>  
H. H. Williams,<sup>31</sup> P. Wilson,<sup>10</sup> B. L. Winer,<sup>27</sup> D. Winn,<sup>24</sup> S. Wolbers,<sup>10</sup>  
D. Wolinski,<sup>24</sup> J. Wolinski,<sup>25</sup> S. Wolinski,<sup>24</sup> S. Worm,<sup>26</sup> X. Wu,<sup>13</sup> J. Wyss,<sup>32</sup>  
A. Yagil,<sup>10</sup> W. Yao,<sup>21</sup> G. P. Yeh,<sup>10</sup> P. Yeh,<sup>1</sup> J. Yoh,<sup>10</sup> C. Yosef,<sup>25</sup> T. Yoshida,<sup>28</sup>  
I. Yu,<sup>19</sup> S. Yu,<sup>31</sup> Z. Yu,<sup>45</sup> A. Zanetti,<sup>40</sup> F. Zetti,<sup>21</sup> and S. Zucchelli<sup>3</sup>

(CDF Collaboration)

<sup>1</sup> *Institute of Physics, Academia Sinica, Taipei, Taiwan 11529, Republic of China*

<sup>2</sup> *Argonne National Laboratory, Argonne, Illinois 60439*

<sup>3</sup> *Istituto Nazionale di Fisica Nucleare, University of Bologna, I-40127 Bologna, Italy*

<sup>4</sup> *Brandeis University, Waltham, Massachusetts 02254*

<sup>5</sup> *University of California at Los Angeles, Los Angeles, California 90024*

<sup>6</sup> *Instituto de Fisica de Cantabria, CSIC-University of Cantabria, 39005 Santander, Spain*

<sup>7</sup> *Enrico Fermi Institute, University of Chicago, Chicago, Illinois 60637*

<sup>8</sup> *Joint Institute for Nuclear Research, RU-141980 Dubna, Russia*

<sup>9</sup> *Duke University, Durham, North Carolina 27708*

<sup>10</sup> *Fermi National Accelerator Laboratory, Batavia, Illinois 60510*

<sup>11</sup> *University of Florida, Gainesville, Florida 32611*

<sup>12</sup> *Laboratori Nazionali di Frascati, Istituto Nazionale di Fisica Nucleare, I-00044 Frascati, Italy*

<sup>13</sup> *University of Geneva, CH-1211 Geneva 4, Switzerland*

<sup>14</sup> *Harvard University, Cambridge, Massachusetts 02138*

<sup>15</sup> *Hiroshima University, Higashi-Hiroshima 724, Japan*

<sup>16</sup> *University of Illinois, Urbana, Illinois 61801*

<sup>17</sup> *The Johns Hopkins University, Baltimore, Maryland 21218*

<sup>18</sup> *Institut für Experimentelle Kernphysik, Universität Karlsruhe, 76128 Karlsruhe, Germany*

<sup>19</sup> *Korean Hadron Collider Laboratory: Kyungpook National University, Taegu 702-701; Seoul National University, Seoul 151-742; and SungKyunKwan University, Suwon 440-746; Korea*

<sup>20</sup> *High Energy Accelerator Research Organization (KEK), Tsukuba, Ibaraki 305, Japan*

<sup>21</sup> *Ernest Orlando Lawrence Berkeley National Laboratory, Berkeley, California 94720*

- <sup>22</sup> *Massachusetts Institute of Technology, Cambridge, Massachusetts 02139*
- <sup>23</sup> *Institute of Particle Physics: McGill University, Montreal H3A 2T8; and University of Toronto,  
Toronto M5S 1A7; Canada*
- <sup>24</sup> *University of Michigan, Ann Arbor, Michigan 48109*
- <sup>25</sup> *Michigan State University, East Lansing, Michigan 48824*
- <sup>26</sup> *University of New Mexico, Albuquerque, New Mexico 87131*
- <sup>27</sup> *The Ohio State University, Columbus, Ohio 43210*
- <sup>28</sup> *Osaka City University, Osaka 588, Japan*
- <sup>29</sup> *University of Oxford, Oxford OX1 3RH, United Kingdom*
- <sup>30</sup> *Universita di Padova, Istituto Nazionale di Fisica Nucleare, Sezione di Padova, I-35131 Padova, Italy*
- <sup>31</sup> *University of Pennsylvania, Philadelphia, Pennsylvania 19104*
- <sup>32</sup> *Istituto Nazionale di Fisica Nucleare, University and Scuola Normale Superiore of Pisa, I-56100 Pisa,  
Italy*
- <sup>33</sup> *University of Pittsburgh, Pittsburgh, Pennsylvania 15260*
- <sup>34</sup> *Purdue University, West Lafayette, Indiana 47907*
- <sup>35</sup> *University of Rochester, Rochester, New York 14627*
- <sup>36</sup> *Rockefeller University, New York, New York 10021*
- <sup>37</sup> *Rutgers University, Piscataway, New Jersey 08855*
- <sup>38</sup> *Texas A&M University, College Station, Texas 77843*
- <sup>39</sup> *Texas Tech University, Lubbock, Texas 79409*
- <sup>40</sup> *Istituto Nazionale di Fisica Nucleare, University of Trieste/ Udine, Italy*
- <sup>41</sup> *University of Tsukuba, Tsukuba, Ibaraki 305, Japan*
- <sup>42</sup> *Tufts University, Medford, Massachusetts 02155*
- <sup>43</sup> *Waseda University, Tokyo 169, Japan*
- <sup>44</sup> *University of Wisconsin, Madison, Wisconsin 53706*
- <sup>45</sup> *Yale University, New Haven, Connecticut 06520*

This report describes a measurement of the top quark mass in  $p\bar{p}$  collisions at a center of mass energy of 1.8 TeV. The data sample was collected with the CDF detector during the 1992–95 collider run at the Fermilab Tevatron, and corresponds to an integrated luminosity of  $106 \text{ pb}^{-1}$ . Candidate  $t\bar{t}$  events in the “lepton+jets” decay channel provide our most precise measurement of the top quark mass. For each event a top mass is determined by using energy and momentum constraints on the production of the  $t\bar{t}$  pair and its subsequent decay. A likelihood fit to the distribution of reconstructed masses in the data sample gives a top mass in the lepton+jets channel of  $176.1 \pm 5.1(\text{stat.}) \pm 5.3(\text{syst.}) \text{ GeV}/c^2$ . Combining this result with measurements from the “all-hadronic” and “dilepton” decay topologies yields a top mass of  $176.1 \pm 6.6 \text{ GeV}/c^2$ .

PACS numbers 14.65.Ha, 13.85.Qk, 13.85.Ni

# Section 1

## INTRODUCTION

This paper describes a measurement of the top quark mass using events produced in proton-antiproton ( $p\bar{p}$ ) collisions at the Fermilab Tevatron with a center-of-mass energy of 1.8 TeV and reconstructed through the decay mode  $t\bar{t} \rightarrow W^+b + W^-\bar{b} \rightarrow \ell^+\nu b + q\bar{q}'\bar{b}$  (and charge conjugate mode). Throughout this paper the symbol  $\ell$  will be used to denote either an electron or a muon exclusively. We present results from two data samples with integrated luminosities of 19.7 pb<sup>-1</sup> (Run 1a) and 86.3 pb<sup>-1</sup> (Run 1b) collected with the Collider Detector at Fermilab (CDF) from September 1992 to June 1993 and from February 1994 to July 1995, respectively.

The existence of the top quark was established by direct experimental observation at the Fermilab Tevatron by the CDF [1, 2] and DØ collaborations [3]. These analyses led to  $t\bar{t}$  cross section and top quark mass measurements. Additional analyses showed that the kinematics of the observed events were inconsistent with being solely from background sources and were consistent with standard model  $t\bar{t}$  [4]. With substantially larger data samples and improved understanding of systematic uncertainties, more precise measurements of the top quark mass [5, 6] and  $t\bar{t}$  production cross section [7, 8] in  $p\bar{p}$  collisions were recently reported. The larger data samples were used to per-

form detailed comparisons of kinematic variables between  $t\bar{t}$  candidate events and simulated standard model  $t\bar{t}$  and background events [9]. The data samples were also used in the identification and analysis of  $t\bar{t}$  production into fully hadronic final states [10, 11] and final states involving two leptons,  $\ell\bar{\ell}$  [12, 13] or  $\ell\tau$  [18].

The top quark is defined as the  $I_3 = +1/2$  member of a weak SU(2) isodoublet that also contains the  $b$  quark. In  $p\bar{p}$  collisions, top quarks are expected to be produced primarily in  $t\bar{t}$  pairs via quark-antiquark annihilation ( $\approx 90\%$ ) or gluon fusion ( $\approx 10\%$ ) and decay through the electroweak interaction to a final state consisting of a  $W$  boson and  $b$  quark. In the standard model, the branching fraction for  $t \rightarrow Wb$  is expected to be nearly 100%. The decay width is calculated to be  $1.6 - 1.7$  GeV for masses between 150 and 180 GeV/ $c^2$  [14]. The top quark mass is sufficiently large that top-flavored hadrons are not expected to form [15].

The mass of the top quark,  $M_{top}$ , is an important parameter in calculations of electroweak processes since it is approximately 35 times larger than that of the next heaviest fermion. Like other fermion masses,  $M_{top}$  is not predicted in the standard model [16]. On the other hand, the standard model relates the masses of the top quark and  $W$  boson to that of the Higgs boson, so that precise measurements of the former imply bounds on the latter. With the assumption of the validity of the standard model, experimental studies of the electroweak interaction can alternatively be used to estimate the value of  $M_{top}$ . For instance, a fit to LEP (including LEP-II) data, leaving the top quark mass and the Higgs mass as free parameters, yields an inferred top quark mass of  $160^{+13}_{-9}$  GeV/ $c^2$  and a Higgs mass of  $60^{+127}_{-35}$  GeV/ $c^2$  [17].

The decay modes of the  $W$  bosons into either lepton-neutrino ( $\ell\nu$ ), ( $\tau\nu$ ) or quark-antiquark ( $q\bar{q}'$ ) final states classify candidate  $t\bar{t}$  events into four main categories. All-hadronic final states, which comprise approximately 44% of  $t\bar{t}$  decays, correspond to those events in which both  $W$  bosons decay hadron-



ically. Lepton+jet events are those events in which only one of the two  $W$  bosons decays hadronically while the other decays into  $\ell\nu$  and form 30% of  $t\bar{t}$  decays. Dilepton events are defined as those in which the  $W$  bosons decay into either  $e\nu$  or  $\mu\nu$  final states and occur only about 5% of the time. Lastly, there is an additional 21% of events for which the final state includes one or more  $\tau$  leptons. The  $\tau$  events are particularly difficult to identify because  $\tau$ 's decay into leptons or hadrons and are often indistinguishable from the other final states, thus contaminating the other samples. Each  $t\bar{t}$  decay mode is characterized by a final state consisting of two  $b$  hadrons and either zero, two, or four additional jets, depending on the decay mode of the  $W$ 's in the event. Additional jets beyond those from the  $t\bar{t}$  decay may also arise from initial and final state radiation of the incoming and outgoing partons.

The direct experimental determination of  $M_{top}$  through analysis of  $t\bar{t}$  pairs produced in  $p\bar{p}$  collisions can be obtained by comparing observed kinematic features of top events to those predicted for different top quark masses [9]. While any kinematic variable which exhibits sensitivity to the mass of the top quark may be used to measure  $M_{top}$ , the lowest statistical uncertainty is achieved by explicitly reconstructing the top mass from the  $t\bar{t}$  daughter decay products. In this paper, we discuss the complete reconstruction of top events in the lepton+jets topology and report the measurement of  $M_{top}$  obtained using the distribution of the reconstructed top quark masses from the data sample.

This paper is structured as follows. Section 2 presents a description of the CDF detector, emphasizing the subsystems most important to this analysis. Section 3 discusses the reconstruction of jets and leptons in the CDF detector and defines the sample of events which are used in the measurement of the top quark mass. Section 4 describes the simulations used and discusses the details of the background calculation. Section 5 describes the corrections which are applied to the raw calorimeter measurements. Section 6 presents

the algorithm used to estimate the top quark mass on an event-by-event basis and describes the results of the algorithm when applied to simulated samples of both  $t\bar{t}$  and background events. The description of the likelihood procedure and the subsequent extraction of  $M_{top}$  are the subjects of Sections 7 and 8. Section 9 describes the systematic uncertainties associated with the top quark mass measurement. Combining the measurements from the lepton+jets, dilepton, and all-hadronic analyses is the focus of Section 10. Conclusions are given in Section 11.

# Section 2

## THE CDF DETECTOR

The CDF detector is an azimuthally symmetric general purpose detector. It consists of independent subsystems designed for distinct tasks. The three most relevant subsystems to  $t\bar{t}$  detection are the tracking chambers, the calorimetry, and the muon chambers. In this section, we briefly describe these subsystems. The various subsystems are shown in the side view of one quadrant of the detector in Fig. 2.1. A more detailed description of each of these components can be found in Refs. [1, 19]

### 2.1 Detector subsystems

The tracking system consists of three subsystems that are all immersed in a 1.4 T solenoidal magnetic field. The outermost system, the central tracking chamber (CTC) [20], is a wire drift chamber consisting of 84 concentric cylindrical layers of sense wires. The CTC has a length of 3.2 m and an outer radius of 1.32 m which results in full acceptance for charged particles in the region  $|\eta| < 1$  [21]. The momentum transverse to the beamline ( $P_T$ ) is measured by the CTC with a precision given by  $\delta(P_T)/P_T = 0.0011P_T$  ( $P_T$

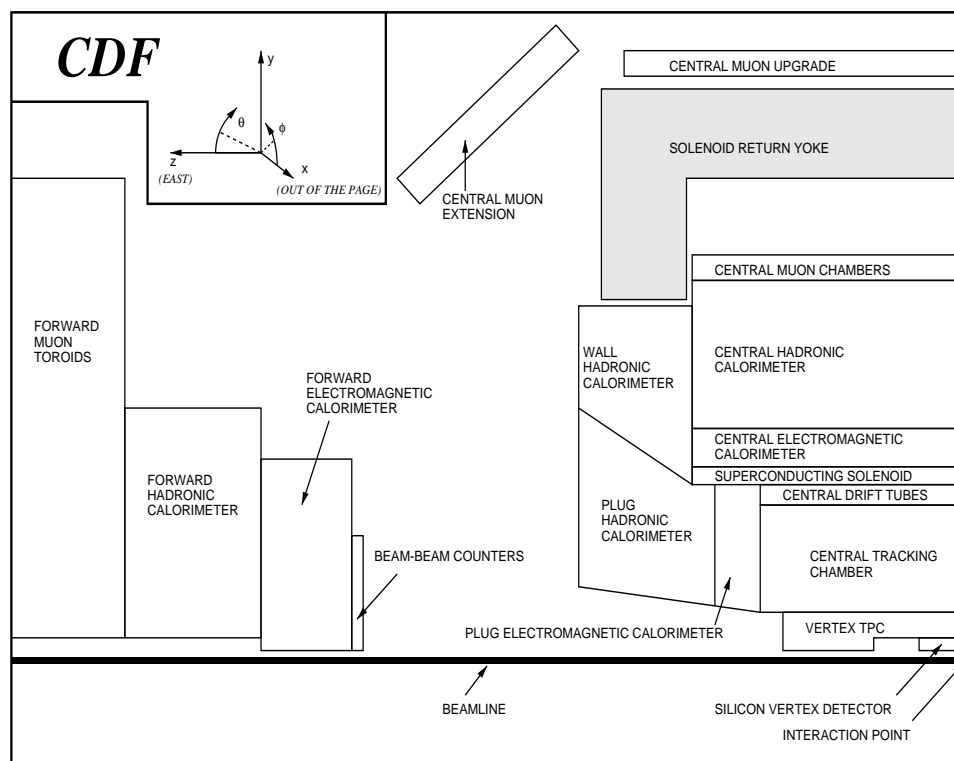


Figure 2.1: Side view of one quadrant of the CDF detector for Run 1. The detector is symmetric about the interaction point.

in  $\text{GeV}/c$ ), when the track is constrained to go through the beam position determined for each run.

Inside the CTC is a set of time projection chambers (TPC) [22], with tracking coverage in the region  $|\eta| < 3.25$ . This detector, referred to as the VTX, is used to measure the position of the  $p\bar{p}$  interaction vertex along the  $z$ -axis with a resolution of 1 mm. In events with more than one reconstructed vertex, the primary vertex is taken to be the one with the largest number of VTX hits on its associated tracks. Primary collisions are spread with an approximately Gaussian density along the  $z$ -axis with  $\sigma \sim 30$  cm. The primary vertex is required to be within  $\pm 60$  cm of  $z = 0.0$ . The efficiency of this requirement is evaluated using the same techniques described in Ref. [23] and is estimated to be 95.6%.

The innermost tracking system, the silicon vertex detector, SVX, consists of four layers of single-sided silicon detectors (the Run 1a detector was replaced for Run 1b due to radiation damage) [24], mounted inside two cylindrical barrels having a combined length of 51.0 cm. The four layers are located at radii of approximately 3.0, 4.2, 6.8 and 7.9 cm from the beam-line. The axial strips of the three innermost layers have  $60 \mu\text{m}$  pitch, and the outermost layer has  $55 \mu\text{m}$  pitch. The silicon detector measures hits in the transverse plane with a precision of  $13 \mu\text{m}$  and the impact parameter of tracks relative to the primary vertex has a precision of  $(13 + 40/P_T) \mu\text{m}$  ( $P_T$  in  $\text{GeV}/c$ ). Secondary vertices (from weak decays, for example) are identified and reconstructed by augmenting reconstructed CTC tracks with hits found in the SVX. The precision of the SVX enables efficient identification of secondary vertices from the decays of  $b$  hadrons ( $c\tau \sim 400 \mu\text{m}$ ). The momentum resolution of a track reconstructed using both the SVX and CTC detectors is given by  $\delta P_T/P_T = \sqrt{(0.0009 P_T)^2 + (0.0066)^2}$ , where  $P_T$  is in  $\text{GeV}/c$  and the second term is due to multiple scattering.

Muons are identified by the association of reconstructed track seg-

ments in the proportional wire chambers of either of the three muon systems, the central muon system (CMU) [25], the central muon upgrade (CMP), or the central muon extension (CMX), with charged particle tracks observed in the CTC. The CMU and CMP, separated by 0.6 m of steel, each cover the pseudorapidity region  $|\eta| < 0.6$ . In that region CMU covers  $\approx 84\%$  of the solid angle, CMP  $\approx 63\%$ , and both combined  $\approx 53\%$ . At larger pseudorapidities the CMX provides  $\approx 71\%$  coverage of the solid angle for  $0.6 < |\eta| < 1$ .

The CDF calorimeters are segmented into projective towers. The towers are further divided into compartments designed to separately measure electromagnetic and hadronic energy. Three separate regions of calorimetry provide coverage in  $\eta$  from  $-4.2$  to  $4.2$ . All of the electromagnetic calorimeters use lead as the absorber, while the hadronic calorimeters use iron. In the central region, coverage is provided by electromagnetic and hadronic calorimeters, CEM [26] and CHA/WHA [27], respectively. The CEM is composed of alternating layers of lead and scintillator, whereas the CHA and WHA are composed of alternating layers of iron and scintillator. Coverage at larger pseudorapidities is provided by calorimeters PEM and PHA, and in the far forward regions by the FEM and FHA. These calorimeters use gas proportional chambers, instead of scintillators, as the active sampling medium. The calorimeters provide identification of, and energy measurement for jets, electrons, photons, unclustered energy [28], and missing transverse energy ( $\cancel{E}_T$ ) [29]. The coverage in pseudorapidity and the energy resolution for the calorimeters are given in Table 2.1.

## 2.2 Luminosity and triggers

The events used in this analysis are extracted from two data samples with integrated luminosities of  $19.7 \text{ pb}^{-1}$  (Run 1a) and  $86.3 \text{ pb}^{-1}$  (Run 1b) collected during the period from September 1992 to June 1993, and from

Detector	$\eta$ range	Energy resolution
CEM	$ \eta  < 1.1$	$13.5\%/\sqrt{E_T} \oplus 2\%$
PEM	$1.1 <  \eta  < 2.4$	$22\%/\sqrt{E_T} \oplus 2\%$
FEM	$2.2 <  \eta  < 4.2$	$26\%/\sqrt{E_T} \oplus 2\%$
CHA	$ \eta  < 0.9$	$50\%/\sqrt{E_T} \oplus 3\%$
WHA	$0.7 <  \eta  < 1.3$	$75\%/\sqrt{E_T} \oplus 4\%$
PHA	$1.3 <  \eta  < 2.4$	$106\%/\sqrt{E_T} \oplus 6\%$
FHA	$2.4 <  \eta  < 4.2$	$137\%/\sqrt{E_T} \oplus 3\%$

Table 2.1: Coverage in pseudorapidity and energy resolution for the various calorimeters. The symbol  $\oplus$  signifies that the constant term is added in quadrature with the sampling (first) term. Energy resolutions for the electromagnetic calorimeters are for incident electrons and photons. For the hadronic calorimeters, they are for incident pions.  $E_T$  should be expressed in GeV.

February 1994 to July 1995 respectively. Instantaneous luminosities varied between  $1 \times 10^{30}$  to  $2 \times 10^{31} \text{cm}^{-2} \text{sec}^{-1}$  during the data taking period, with averages that increased from  $\approx 3.3 \times 10^{30} \text{cm}^{-2} \text{sec}^{-1}$  during Run 1a to  $\approx 1 \times 10^{31} \text{cm}^{-2} \text{s}^{-1}$  for Run 1b. The corresponding average number of interactions per crossing increased from 0.6 to 1.8. Since the measured jet energies increase in the presence of additional interactions, the corrections to the jet energies differ between Run 1a and Run 1b (see Section 5.1.1).

A multi-level trigger is used to select events containing high- $P_T$  leptons [1, 7]. To increase the  $t\bar{t}$  acceptance in the muon channel, a trigger based on the missing transverse energy ( $\cancel{E}_T$ ) was added for Run 1b [7]. For the high- $P_T$  inclusive lepton sample, only triggers from the central region are used in this analysis. The CEM trigger efficiency for fiducial [30] electrons from  $t\bar{t}$  events with  $E_T > 20 \text{ GeV}$  and  $|\eta| < 1$  is essentially 100%. The muon trigger is measured to be 85.4% efficient for fiducial muons from  $t\bar{t}$  events that have  $P_T > 20 \text{ GeV}/c$ .

# Section 3

## DATA SAMPLES

The data sample selection for this analysis is based on standard model decay of top quark pairs through the  $t\bar{t} \rightarrow \ell\nu q\bar{q}'b\bar{b}X$  channel. The final state should therefore include a high- $E_T$  ( $P_T$ ) electron (muon), significant missing transverse energy and four jets. The momenta of these objects are measured from data recorded with each detector subsystem, sometimes in combination. The four-momenta of electrons are expressed in terms of  $(E_T, \phi, \eta, m)$  where  $E_T$  is the transverse energy ( $E_T \equiv E \sin \theta$ ),  $\phi$  is the azimuthal angle,  $\eta$  is the pseudorapidity and  $m$  is the mass. For muons and jets  $P_T$  is used rather than  $E_T$ . In all cases, the direction of these objects is measured with much greater precision than their energies. In this section, we first describe the identification and reconstruction of leptons and jets, and then we define the data samples.

### 3.1 High- $P_T$ leptons

We are most interested in identifying charged leptons which are produced from the decay of a  $W$  boson. These leptons are distinguished from those produced in semileptonic decay of  $b$  or  $c$  quarks because leptons from  $W$ -boson decay are not part of a jet and have typically much higher  $P_T$ . A



sample of high- $P_T$  leptons is used to select leptons which are consistent with having come from  $W$ -boson decay.

A sample of events which contain high- $E_T$  electrons are selected from the Run 1 data sample by requiring the electron to have  $E_T > 20$  GeV/ $c$  and be in the central region of the detector ( $|\eta| < 1$ ). Backgrounds from photon conversions and charged hadrons are rejected by cutting on several variables. Here we describe those cuts which provide the largest discrimination against background. A detailed discussion of other selection criteria can be found in Ref. [1]. Electrons are required to have a CTC track pointing to the electron shower in the CEM. The energy in the hadronic calorimeter divided by the energy detected in the electromagnetic calorimeter ( $HAD/EM$ ) is required to be less than 5%. We also require that the energy of the shower divided by the momentum of the associated track is less than 1.8. Electrons from photon conversions are removed with an efficiency of 88% [1] by requiring each electron to have a matching track in the VTX, and the invariant mass of this track with any other CTC track to be greater than 0.5 GeV/ $c^2$ . The energy of high- $E_T$  electrons is measured using the calorimeter energy in the tower to which the CTC track points plus the adjacent towers [31]. High- $E_T$  electrons are measured with a resolution of  $\sigma(E_T)/E_T = 13.5\%/\sqrt{E_T} \oplus 2\%$ , where  $E_T$  is in GeV.

The high- $P_T$  muon sample is selected by requiring that each event contain at least one muon candidate which has  $P_T > 20$  GeV/ $c$  and is in the central region of the detector ( $|\eta| < 1$ ). Muon candidates are identified by a match between a track segment in CMU, CMP, or CMX and the CTC. The primary backgrounds are from secondary particles in charged hadron showers which “punch through” the calorimeter and produce tracks in the muon chambers, and cosmic rays. To reject the charged hadron background, the muon is required to have an energy deposition in the calorimeters which is characteristic of a minimum ionizing particle. Backgrounds from cosmic rays

are rejected by requiring that the track extrapolates back (in  $r - \phi$ ) to within 3 mm of the beamline and that in the  $r - z$  plane it is within 5 cm (at  $r=0$ ) of the primary vertex. A number of other selection requirements are made which are described in Ref. [1]. The momentum of high- $P_T$  muons is measured by constraining the CTC track to the average beam position. Its transverse momentum is measured with a resolution of  $\sigma(P_T)/P_T = 0.11\%P_T$ , where  $P_T$  is in GeV/ $c$ .

From these high- $P_T$  lepton samples, we further select those events in which the high- $P_T$  lepton is isolated [32] from jet activity. For the lepton+jets analysis, we require that there is only one  $W \rightarrow \ell\nu$  candidate in the event. The lepton  $\ell$  is referred to as the primary lepton in the event.

## 3.2 Jet reconstruction

Jets are constructed from calorimeter tower information using a cone algorithm with cone radius  $\Delta R \equiv \sqrt{\Delta\eta^2 + \Delta\phi^2} = 0.4$ . The jet transverse energy is defined as the sum of the energy deposited in calorimeter towers within the cone, multiplied by  $\sin\theta$ , where  $\theta$  is the polar angle of the  $E_T$ -weighted centroid of the clustered towers. After correcting for the various energy losses (see Section 5), jets which do not contain heavy flavor, and have  $P_T > 80$  GeV, have a transverse momentum resolution of  $\delta P_T/P_T \approx 12\%$ . A discussion of the jet reconstruction algorithm can be found in Ref. [33, 49].

### 3.2.1 Identification of $b$ -quark jets

The identification of jets that arise from  $b$  quarks ( $b$ -quark jets or simply  $b$  jets) plays an important role in the analysis described in this report. The identification relies on finding evidence for a  $B$ -hadron decay, using two separate tagging algorithms.

The silicon vertex (SVX) tag algorithm [1, 7] searches within a jet for

displaced vertices due to  $B$ -hadron decays. It is applied to jets that have raw  $E_T > 15$  GeV and uses tracks which are within  $\Delta R < 0.4$  of the jet axis and have hits in the silicon vertex detector. The algorithm allows for two passes. In the first pass, a secondary vertex is required to have at least three tracks with  $P_T > 0.5$  GeV/ $c$ , at least one of which has  $P_T > 2.0$  GeV/ $c$ . In the second pass, tighter track quality cuts are applied, and a secondary vertex is required to have at least two tracks with  $P_T > 1.0$  GeV/ $c$ , including at least one with  $P_T > 2.0$  GeV/ $c$ . This algorithm has an efficiency of about 48% for tagging at least one  $b$  jet in a  $t\bar{t}$  event.

The soft lepton tag (SLT) algorithm [1, 34] searches for additional leptons which are consistent with having come from a semileptonic  $B$ -hadron decay. The lepton is required to have  $P_T > 2$  GeV/ $c$  and to be within  $\Delta R < 0.4$  of a jet with raw jet  $E_T > 8$  GeV. The efficiency for tagging at least one  $b$  jet in a  $t\bar{t}$  event with this algorithm is about 15%.

The SVX algorithm obtains both higher purity and higher efficiency than the SLT algorithm. However, the SLT algorithm is also employed for tagging  $b$  jets because it uses nearly uncorrelated information and adds significantly to the acceptance.

### 3.3 Top mass candidate sample

Full reconstruction of candidate  $t\bar{t}$  events is possible if the event has at least four jets and a  $W$  candidate decaying into either  $e\nu$  or  $\mu\nu$ . The majority of such events are not from  $t\bar{t}$  production but rather from the production of a  $W$  boson in association with jets. The fraction of these background events containing at least one  $b$  jet is of the order of 1% [1], while standard model  $t\bar{t}$  decays are expected to always have two  $b$  jets. Data samples with larger fractions of  $t\bar{t}$  events can therefore be formed by requiring evidence of  $b$  hadrons in one or more jets.

To facilitate the measurement of the top quark mass, we apply selection criteria which are expected to increase the fraction of  $t\bar{t}$  events in the sample. We refer to these events as the Top Mass Candidate Sample, and they satisfy the following cuts:

1. High- $E_T$  lepton trigger satisfied; The event should have an electron (muon) with  $E_T > 20$  GeV ( $P_T > 20$  GeV/ $c$ ) and  $|\eta| < 1$ .
2.  $\cancel{E}_T$ , as calculated using the raw tower energies, is greater than 20 GeV. For events with a primary muon this  $\cancel{E}_T$  includes a correction for the muon momentum.
3. The candidate primary electron or muon track must be isolated and of good quality (see Section 3.1). Only one isolated lepton should be present.
4. Candidate dilepton ( $t\bar{t} \rightarrow \ell^+ \bar{\nu} \ell^- \nu b \bar{b} X$ ) events, defined according to the selection criteria of Ref. [12], are rejected.
5. Events with  $Z$ -boson candidates are removed. A  $Z$ -boson candidate is defined by two oppositely charged, same flavor high- $P_T$  leptons ( $P_T > 20$  GeV/ $c$ ) that have an invariant mass between 75 and 105 GeV/ $c^2$ . Also, we remove the event if it includes a high- $P_T$  photon [35] and the  $\ell\bar{\ell}\gamma$  invariant mass falls in the  $Z$  mass window.
6. The primary vertex of the event must be within 60 cm of  $z = 0.0$ .
7. At least three jets with  $E_T > 15$  GeV and  $|\eta| < 2.0$ .
8. For events with exactly three jets satisfying criterion 7 above, we require at least one additional jet with  $E_T > 8$  GeV and  $|\eta| < 2.4$ .
9. After the mass reconstruction is performed, events are required to pass a goodness-of-fit cut,  $\chi^2 < 10.0$ , where the variable  $\chi^2$  is defined in Section 6.

A sample of 324 events pass criteria 1–7, and are the same as those used in the CDF measurement of the  $t\bar{t}$  production cross section [7]. Criteria 1–9 are identical to those used in all our previous measurements of the top quark mass [1, 2]. After imposing criteria 1–8, our sample consists of 163 events. The last requirement removes 12 events, from which we obtain an inclusive sample of 151  $W$ +multi-jet events. Thirty-four of the events have SVX or SLT tagged jets. As discussed below, the Top Mass Candidate Sample is estimated to consist of approximately 74% background. Requiring the presence of  $b$ -tagged jets improves considerably the signal-to-background ratio (see Section 3.3.1).

### 3.3.1 Mass subsamples

To describe the mass subsamples which are used in this analysis, it is helpful to decompose the Top Mass Candidate Sample into two classes of events which are expected to have different signal-to-background ratios (S/B). Class I events have exactly three jets with  $E_T > 15$  GeV and  $|\eta| < 2$  and one or more additional jets with  $E_T > 8$  GeV and  $|\eta| < 2.4$ . Class II events have four or more jets with  $E_T > 15$  GeV and  $|\eta| < 2$ . Because of the larger amount of energy contained in the four leading (i.e., four highest  $E_T$ ) jets, class II events have a larger S/B than class I.

Previous measurements of the top quark mass at CDF used a combined sample of  $b$ -tagged events [1, 2] that contained events from both class I and class II. Monte Carlo simulations show that the statistical uncertainty on the measured top quark mass is reduced by 10% by combining the results of separate fits on three non-overlapping subsamples of events. The first subsample consists of events that have one and only one SVX tag. The second subsample consists of events in which there are two SVX tags. The third one includes events that have one or two SLT tags, but no SVX tags. Further Monte Carlo studies show that an additional 7% improvement is obtained by including the No Tag events from class II. The 75 No Tag events excluded from

the Top Mass Candidate Sample are expected to have a background fraction of 93%. Inclusion of these events does not improve the statistical uncertainty on the top quark mass measurement. To summarize, the four mass subsamples are [36]:

- SVX Double: Events with two SVX tags;
- SVX Single: Events with one and only one SVX tag;
- SLT: Events with one or two SLT tags, but no SVX tags;
- No Tags:  $\geq 4$  jets with  $E_T > 15$  GeV and  $|\eta| < 2$ .

The numbers of data events in each of these subsamples are shown in Table 3.1. In categorizing the events into the subsamples, tags are only counted if they are on one of the four highest  $E_T$  jets. This choice is made because the four leading jets are assumed to be the primary partons from the  $t\bar{t}$  decay (see Section 6). Also shown in the table are the expected S/B ratios, using the background estimates presented in Section 4.3.3. The measurement of the top quark mass in the lepton+jets channel is based on these four subsamples.

Data Sample	Number of Events	Expected S/B
SVX Double	5	24
SVX Single	15	5.3
SLT	14	0.8
No Tags	42	0.4

Table 3.1: Subsamples used in the lepton+jets mass analysis and the expected signal to background ratio (S/B) for each. See Section 4.3.3 for background estimates for these subsamples.

# Section 4

## SIMULATION AND BACKGROUND

This section describes the Monte Carlo methods used to simulate the signal and background events, and the estimation of the background in the four mass subsamples. For this purpose we use Monte Carlo programs that generate the signal and background processes contributing to the data sample, and a detector simulation which models the response of the detector to the final state particles. Unless otherwise noted, the Monte Carlo programs use the MRSD0' [37] set of structure functions. Detailed properties of  $b$ -hadron decay, based on observations from the CLEO experiment [38], are included in all the Monte Carlo generators. The response of the detector to the final state particles is parametrized using distributions observed in data. See Section 5 for details on the calorimeter simulation.

### 4.1 Signal modeling

The simulation of  $t\bar{t}$  events relies mainly on the HERWIG [39] (Version 5.6) Monte Carlo program. Additional checks are provided by both

PYTHIA [40] (Version 5.7) and ISAJET [41] (Version 6.36). HERWIG is based on the leading order QCD matrix elements for the hard process, followed by coherent parton shower evolution, cluster hadronization, and an underlying event model based on data. PYTHIA is similar to HERWIG in that it is based on leading order QCD matrix elements; however, partons are fragmented using the Lund string model. ISAJET is a parton shower Monte Carlo program based on the leading-order QCD matrix elements for the hard-scattering subprocess, incoherent gluon emission, and independent fragmentation of the outgoing partons.

## 4.2 Background modeling

The Monte Carlo program used to study the kinematics of the background is VECBOS [42]. This is a parton-level program based on tree-level matrix element calculations for  $W$ +jets production. The simulated events produced by VECBOS contain a  $W$  boson and up to four additional final state partons. These partons are subsequently evolved and hadronized using a separate program [43] derived from the parton shower model contained in the HERWIG Monte Carlo generator. The CDF simulation program is then used to simulate the detector response and produce the final sample of background events for further analysis.

The VECBOS events generated for this analysis use the  $W + 3$  parton matrix elements, with the required additional jet being produced during parton showering. The  $Q^2$  scale of the hard scatter is set to the square of the average  $P_T$  ( $\langle P_T \rangle^2$ ) of the outgoing partons unless otherwise noted.

The VECBOS Monte Carlo generator has been shown to reproduce distributions of a wide range of kinematic variables in a large sample of  $W$ +jets events [44] in this experiment. In addition, distributions of kinematic variables have been studied in  $t\bar{t}$ -depleted and  $t\bar{t}$ -enriched subsamples of  $W + \geq 3$  jet



events in this experiment [9]. The Monte Carlo simulations reproduce the distributions in both subsamples when we use the expected fractions of HERWIG (for  $t\bar{t}$ ) and VECBOS (for background) events. Further checks which demonstrate that VECBOS is appropriate for background modeling are given in Section 6.5.

### 4.3 Background estimation

In the measurement of the top quark mass, we constrain the fraction of background events in each of the mass subsamples to an expected value. The computation of the expected value for each mass subsample is achieved by first computing the expected number of background events from relevant background processes for both class I and class II events (see Section 3.3.1). Some of the background processes are computed as absolute predictions while others are given as a fraction of the number of background  $W$ -candidates in the data sample. The expected  $t\bar{t}$  and background fractions (which sum to unity) in the Top Mass Candidate Sample are then estimated by using a maximum likelihood fit which compares the observed rates of events with SVX and SLT tags with predicted rates. The predicted rates, which use estimates of the tagging probabilities for  $t\bar{t}$  and background events, depend on these fractions. The  $t\bar{t}$  fraction is a free parameter in the fit, and is allowed to vary to optimize the agreement between the observed and predicted numbers of tagged events. The fitted  $t\bar{t}$  fraction in the Top Mass Candidate sample is then combined with SVX and SLT tagging probabilities to evaluate the expected  $t\bar{t}$  and background contribution in each of the mass subsamples. The same principle has been used to measure the  $t\bar{t}$  cross section using  $W + \geq 3$  jets events [7, 45].

The tagging probabilities we use, and the contributions of various background channels, are similar to those in Ref. [45], but are not identical because of differences in the event selections and the exact tagging rules. The

event selections used in this paper require a fourth jet and impose a  $\chi^2$  cut on the kinematic mass fit (described in Section 6). The tagging rule used here, requires that the SVX and SLT tags are counted only if they are on one of the four leading jets in the event. The resulting differences in tagging probabilities and backgrounds are determined using the HERWIG and VECBOS Monte Carlo simulations.

### 4.3.1 Inputs into the background calculation

The inputs into the calculation are the background processes, their expected rates, and the corresponding SVX and SLT tagging probabilities. The rates and tagging probabilities are estimated for both the class I and class II events of the Top Mass Candidate Sample. Of the 151 events in the Top Mass Candidate Sample, 87 are in class I and 64 in class II.

The background processes are classified into two categories: contributions which are computed as an absolute number of events, and contributions which are calculated as a fraction of the number of background candidate  $W$ +jets events ( $N_W$ ) in the data sample. In the latter case, the contribution includes  $Z$ +jets events that pass the lepton+jets selection criteria. The background processes considered are listed in Tables 4.1 and 4.2 for the two classes (the processes are the same for both classes). The expected numbers of background events from the different processes are also given in the tables.

For the first six processes we have absolute predictions. For the  $W$ +jets and  $Z$ +jets processes we have predictions for each process relative to their sum. The last two columns in Tables 4.1 and 4.2 give the SVX and SLT tagging probabilities per event for each background process. The probabilities in rows 1–13 are for cases where there is a real displaced vertex or a real soft lepton. Each of the background processes can also contribute fake SVX and SLT tags (mistags), and these probabilities are given in row 14. In either case, the SVX and SLT tagging probabilities include the requirement that the tag

is on one of the four leading jets and take into account the  $\chi^2$  cut on the kinematic mass fit.

Item #	Background process	Number of events	$\epsilon_{SVX}$ (%)	$\epsilon_{SLT}$ (%)
Absolute backgrounds				
1	non- $W/Z$	$5.7 \pm 0.8$	$4.3 \pm 2.2$	$2.5 \pm 1.8$
2	$WW$	$0.7 \pm 0.1$	$5.8 \pm 1.7$	$1.3 \pm 0.7$
3	$WZ$	$0.1 \pm 0.0$	$5.8 \pm 1.7$	$1.3 \pm 0.7$
4	$ZZ$	$0.0 \pm 0.0$	$5.8 \pm 1.7$	$1.3 \pm 0.7$
5	$Z \rightarrow \tau\tau$	$0.9 \pm 0.1$	$3.5 \pm 2.5$	$4.6 \pm 4.6$
6	Single Top	$0.4 \pm 0.1$	$30.6 \pm 7.0$	$9.0 \pm 2.4$
$W/Z$ +jets backgrounds				
7	$Wb\bar{b}$	$(0.028 \pm 0.004)N_W^I$	$22.7 \pm 3.1$	$7.0 \pm 1.9$
8	$Wc\bar{c}$	$(0.056 \pm 0.013)N_W^I$	$5.7 \pm 1.0$	$5.5 \pm 1.2$
9	$Wc$	$(0.053 \pm 0.016)N_W^I$	$3.7 \pm 0.5$	$6.3 \pm 1.8$
10	$Zb\bar{b}$	$(0.005 \pm 0.002)N_W^I$	$22.7 \pm 2.0$	$7.0 \pm 1.9$
11	$Zc\bar{c}$	$(0.005 \pm 0.002)N_W^I$	$5.7 \pm 1.0$	$5.5 \pm 1.2$
12	$Zc$	$(0.001 \pm 0.001)N_W^I$	$3.7 \pm 0.5$	$6.3 \pm 1.8$
13	$W/Z + u, d, s$	$0.85N_W^I$	0.0	0.0
Mistag probabilities				
14	1-13		$0.4 \pm 0.1$	$3.2 \pm 0.4$

Table 4.1: Backgrounds which contribute to class I events in the Top Mass Candidate Sample. Shown are the contributing processes, their estimated contribution, and the SVX and SLT tagging probabilities per event for each process. Backgrounds whose absolute rate is calculable (a total of  $N_{abs}^I$  events) are given by 1–6. Backgrounds that are given as fractions of the number of  $W/Z$ +jets events in the data sample are given by 7–13.  $N_W^I$  is the total number of  $W/Z$ +jets background events in class I. All background processes contribute to SVX and SLT mistags, with the probabilities listed in row 14. There are 87 events in class I.

The expected backgrounds and tagging probabilities are calculated as follows. The non- $W/Z$  background is calculated directly from the data [7]. The  $WW$ ,  $WZ$ , and  $ZZ$  background rates are evaluated by multiplying the acceptances for these processes as determined from the PYTHIA Monte Carlo

Item #	Background process	Number of events	$\epsilon_{SVX}$ (%)	$\epsilon_{SLT}$ (%)
Absolute background calculations				
1	non- $W/Z$	$5.5 \pm 1.7$	$4.3 \pm 2.2$	$2.5 \pm 1.8$
2	$WW$	$0.7 \pm 0.2$	$5.8 \pm 1.7$	$1.3 \pm 0.7$
3	$WZ$	$0.1 \pm 0.0$	$5.8 \pm 1.7$	$1.3 \pm 0.7$
4	$ZZ$	$0.1 \pm 0.0$	$5.8 \pm 1.7$	$1.3 \pm 0.7$
5	$Z \rightarrow \tau\tau$	$0.7 \pm 0.3$	$3.5 \pm 2.5$	$4.6 \pm 4.6$
6	Single Top	$0.3 \pm 0.1$	$30.6 \pm 7.0$	$9.0 \pm 2.4$
$W/Z$ +jets backgrounds				
7	$Wbb$	$(0.054 \pm 0.012)N_W^{II}$	$27.4 \pm 2.7$	$7.5 \pm 2.6$
8	$Wc\bar{c}$	$(0.087 \pm 0.025)N_W^{II}$	$6.0 \pm 1.0$	$5.6 \pm 1.2$
9	$Wc$	$(0.073 \pm 0.022)N_W^{II}$	$3.8 \pm 0.5$	$6.3 \pm 1.8$
10	$Zb\bar{b}$	$(0.003 \pm 0.003)N_W^{II}$	$27.4 \pm 2.7$	$7.5 \pm 2.6$
11	$Zc\bar{c}$	$(0.003 \pm 0.003)N_W^{II}$	$6.0 \pm 1.0$	$5.6 \pm 1.2$
12	$Zc$	$(0.001 \pm 0.001)N_W^{II}$	$3.8 \pm 0.5$	$6.3 \pm 1.8$
13	$W/Z + u, d, s$	$0.78N_W^{II}$	0.0	0.0
Mistag probabilities				
14	1-13		$0.4 \pm 0.1$	$4.2 \pm 0.5$

Table 4.2: Backgrounds which contribute to class II events in the Top Mass Candidate Sample. Shown are the contributing processes, their estimated contribution, and the SVX and SLT tagging probabilities per event for each process. Backgrounds whose absolute rate is calculable (a total of  $N_{abs}^{II}$  events) are given by 1–6. Backgrounds that are given as fractions of the number of  $W/Z$ +jets events in the data sample are given by 7–13.  $N_W^{II}$  is the total number of  $W/Z$ +jets background events in class II. All background processes contribute to SVX and SLT mistags with the probabilities shown in row 14. There are 64 events in class II.

simulation by their production cross sections [46]. The  $Z \rightarrow \tau\tau$  background is estimated using the PYTHIA Monte Carlo simulation. The normalization is obtained by scaling the number of reconstructed  $Z \rightarrow \ell\ell + \geq 1$ -jet events in the simulation to the number observed in the Run 1 data sample. For single top quark production, we use the PYTHIA and HERWIG Monte Carlo programs to evaluate the acceptances for the  $W^* \rightarrow tb$  and  $W$ -gluon fusion processes respectively. The production cross sections are normalized to the published theoretical values [47].

The expected fractions of  $Wb\bar{b}$  and  $Wc\bar{c}$  events in the data sample are evaluated using the HERWIG and VECBOS Monte Carlo programs. For each jet multiplicity bin, the expected background is given by the product of the corresponding background fraction, tagging probability and the number of  $W$ -candidate events. The  $Wc$  background is estimated from HERWIG in an analogous way to what is done for the  $Wb\bar{b}$  and  $Wc\bar{c}$  backgrounds. The  $Zb\bar{b}$ ,  $Zc\bar{c}$  and  $Zc$  backgrounds are calculated using a combination of HERWIG, PYTHIA and VECBOS. The simulations show that in both the  $Z+1$  jet and  $Z+2$  jet multiplicity bins  $Zb\bar{b}$  events are approximately twice as likely to pass our kinematic cuts as  $Wb\bar{b}$ . The corresponding ratio for  $Zc\bar{c}$  to  $Wc\bar{c}$  is approximately 1, and  $Zc/Wc$  is about 0.3. We assume that these scalings also hold in the higher jet multiplicity bins. The  $Zb\bar{b}$ ,  $Zc\bar{c}$  and  $Zc$  background rates are thus obtained by scaling the  $Wb\bar{b}$ ,  $Wc\bar{c}$ , and  $Wc$  rates by  $2.0 \pm 0.5$ ,  $1.0 \pm 0.3$ , and  $0.3 \pm 0.15$  respectively. The overall  $Z/W$  normalization is determined from the data sample, and is  $0.092 \pm 0.020$  for events in class I and  $0.030 \pm 0.030$  for events in class II.

The SVX and SLT tagging probabilities in lines 1-13 in Tables 4.1 and 4.2 give the probability per event, that one or more jets will be tagged due to the decay of a long-lived particle (i.e., a  $b$  hadron, a  $c$  hadron, or a  $\tau$ ). For backgrounds which are computed using Monte Carlo programs, the tagging probabilities are evaluated by simulation of the detector's response

to the final state particles of each of the background processes. For SVX tags, the probabilities are calculated using only jets which have an uncorrected  $E_T > 15$  GeV and  $|\eta| < 2$ . For SLT tags the probabilities include all jets which have an uncorrected  $E_T > 8$  GeV and  $|\eta| < 2.4$ . The tagging probabilities for  $W + u, d, s$  are set to zero since these events have a negligible contribution from long-lived particles.

The SVX and SLT mistag probabilities (line 14 in Tables 4.1 and 4.2) are estimated by applying “mistag-matrices” to the jets in each event of the Top Mass Candidate Sample. The mistag matrices [1] for SVX and SLT tags are measured from inclusive jet data and describe the probability for a jet that does not contain heavy flavor to be tagged by the SVX and SLT algorithms respectively. Monte Carlo simulations show a lower mistag rate in background events than in  $t\bar{t}$  events, with a ratio of  $0.70 \pm 0.05$  for both SVX and SLT tags. This ratio is included in the mistag probabilities shown in Tables 4.1-4.3. The effect of using equal mistag probabilities for  $t\bar{t}$  and background has been investigated, and the resulting background numbers change by a negligible amount.

Tagging probabilities for  $t\bar{t}$  events were determined using the HERWIG Monte Carlo program. Additional checks of these probabilities were provided by both the PYTHIA and ISAJET simulations. The probabilities for tagging at least one  $b$ -quark jet in a  $t\bar{t}$  event are shown in Table 4.3. Also shown are the probabilities for tagging a jet which does not contain heavy flavor (mistags). As before, the SVX and SLT tagging probabilities include the requirement that the tag is on one of the four leading jets and require the  $\chi^2$  cut on the kinematic mass fit.

### 4.3.2 $t\bar{t}$ and background fractions in each event class

We first estimate the fractions of background and  $t\bar{t}$  events in each of the two event classes defined in the preceding section. For each event class,

	Tagging probabilities per $t\bar{t}$ event			
	$\epsilon_{SVX}(\%)$		$\epsilon_{SLT}(\%)$	
	Class I	Class II	Class I	Class II
Real tags	44.8 $\pm$ 4.5	49.9 $\pm$ 5.0	14.9 $\pm$ 1.5	14.8 $\pm$ 1.5
Mistags	0.6 $\pm$ 0.1	0.7 $\pm$ 0.1	4.8 $\pm$ 0.5	6.4 $\pm$ 0.7

Table 4.3: SVX and SLT tagging probabilities in  $t\bar{t}$  events for class I and class II events. Shown are the probabilities for tagging one or more jets which contain  $b$  or  $c$  quarks (real tags) and the probabilities for tagging one or more jets which do not contain  $b$  or  $c$  quarks (mistags).

we compare the expected rates of tags with the observed rates in each of four subsamples. The subsamples are events with (i) only SVX tags, (ii) only SLT tags, (iii) both SVX and SLT tags, and (iv) No Tags. The division into these subsamples was chosen to optimize, according to Monte Carlo studies, the background fraction estimate, and is not identical to the mass subsample division. Note that for subsample (iii) the tags can be on the same jet or on different jets.

The expected numbers of events in each of these subsamples (indexed by  $j$ ) can be calculated as a function of the numbers of  $t\bar{t}$  events ( $N_{t\bar{t}}$ ) and non-top  $W$ +jets events in the event class, using an expression of the form:

$$N_j^{exp} = a_j \times N_{t\bar{t}} + \sum_k c_j^k \times N_{abs,j}^k + \sum_i d_j^i b_j^i \times N_W \quad (4.1)$$

Here the first term gives the expected contribution from  $t\bar{t}$  events, and the last two terms give the expected number of events from background processes. The indices  $k$  and  $i$  refer to the background processes 1-6 and 7-13, respectively, in Tables 4.1 and 4.2. The parameter  $a_j$  is the (SVX or SLT) tagging probability for  $t\bar{t}$  events in the  $j^{th}$  subsample, while  $c_j^k$  and  $b_j^i$  are the tagging probabilities, including those for mistags, for background processes  $k$  and  $i$ . The quantities represented by  $d_j^i$  are the coefficients of  $N_W^I$  and  $N_W^{II}$  in Tables 4.1 and 4.2.

The parameter  $N_{abs,j}^k$  is the expected number of background events from the  $k^{th}$  process. Equation 4.1 applies separately to both class I and class II events.

The tagging probabilities in the expression above are derived from the values in Tables 4.1–4.3, apart from some correlation terms. Correlation terms between real and mistag probabilities and between SVX and SLT tag probabilities are included in the calculations, but these terms are relatively small and their effect on the final result is negligible.

To determine the background and  $t\bar{t}$  contributions to class I and class II events, we constrain the total number of  $t\bar{t}$  and background events (i.e., summed over the subsamples) to be equal to the observed number of events in each class. Then we have just one parameter for each class, the fraction,  $f_{t\bar{t}}$ , of  $t\bar{t}$  events (or, equivalently, the fraction of background events). A given value of  $f_{t\bar{t}}$  determines values of  $N_{t\bar{t}}$  and  $N_W$  to be used in Eq. 4.1. A maximum likelihood method is used to determine a best estimate of  $f_{t\bar{t}}$ . The likelihood has the form:

$$L = \prod_i F_j^i(f_{t\bar{t}}) \quad (4.2)$$

where the  $i^{th}$  event falls into subsample  $j$  and the expected fraction of events in subsample  $j$  is  $F_j^i(f_{t\bar{t}})$ .

The results of the maximum likelihood fit are  $f_{t\bar{t}} = 0.13_{-0.06}^{+0.07}(stat.) \pm .01(syst.)$  for class I, and  $f_{t\bar{t}} = 0.45_{-0.11}^{+0.12}(stat.) \pm .05(syst.)$  for class II. The statistical uncertainties correspond to changes in  $\ln L$  from the maxima by 0.5 units. The systematic uncertainties result from adding in quadrature the many contributions due to changing all the relevant input rates and probabilities one at a time by their stated uncertainties. These  $f_{t\bar{t}}$  values imply that  $t\bar{t}$  events comprise  $11.5_{-5.2}^{+6.4}$  of the 87 class I events and  $28.5_{-7.6}^{+8.2}$  of the 64 class II events. The numbers of  $t\bar{t}$  and background events are summarized in Table 4.4.

To check that the model we are using is reasonable, we compare the expected numbers of events in each subsample with the observed numbers.



The comparison is presented in Table 4.5, and shows reasonable agreement between expected and observed numbers.

Process	Class I	Class II
$t\bar{t}$	$11.5^{+6.4}_{-5.2}$	$28.5^{+8.2}_{-7.6}$
Absolute Backgrounds	$7.9 \pm 0.9$	$7.4 \pm 1.8$
$W/Z$ +jets	$67.6^{+5.2}_{-6.4}$	$28.1^{+7.6}_{-8.2}$

Table 4.4: Estimated composition of the Top Mass Candidate Sample for class I and class II events using the background likelihood fit described in the text. Shown are the expected contributions from  $t\bar{t}$  events, absolute backgrounds (as listed in lines 1-6 in Tables 4.1 and 4.2) and  $W/Z$ +jets events. The sum of each column is constrained to the number of observed events in the Top Mass Candidate Sample.

Subsample	Observed		Expected	
	Class I	Class II	Class I	Class II
Only SVX tags	3	10	5.6	12.4
Only SLT tags	6	8	4.2	4.8
Both SVX and SLT tags	3	4	1.1	3.0
No tags	75	42	76.0	43.8
Total	87	64	87	64

Table 4.5: The number of observed and expected events in the four subsamples. The expectation values are based on the background likelihood fit described in the text. The events are separated into class I and class II events.

### 4.3.3 $t\bar{t}$ and background events in the $\ell$ +jets mass subsamples

Having found the numbers of  $t\bar{t}$  and background events for the samples in class I and class II, we can go to the next step, i.e., compute the

expected numbers of top and background events in the mass subsamples. To arrive at estimated  $t\bar{t}$  fractions in the mass subsamples, we need probabilities for two SVX tags in an event. We must also combine the  $t\bar{t}$  fractions for class I and class II events in each tagged subsample. The untagged mass subsample only contains class II events.

For most of the background channels the probabilities for two real SVX tags (i.e., tags due to  $b$ -hadron,  $c$ -hadron, or  $\tau$  decays) are very small or zero. The non-negligible probabilities are given in Table 4.6. Our calculations for the SVX Double subsample do allow appropriately for real and fake tags in all channels. The probabilities for events to enter into one of the four mass subsamples use the probabilities in Tables 4.1, 4.2, and 4.6, and are computed as follows:

$$P(\text{SVX Single}) = P(\text{SVX}) - P(\text{SVX Double}) \quad (4.3)$$

$$P(\text{SLT (no SVX)}) = P(\text{SLT}) - P(\text{SVX} \otimes \text{SLT}) \quad (4.4)$$

$$P(\text{No Tag}) = 1 - P(\text{SVX}) - P(\text{SLT (no SVX)}) \quad (4.5)$$

The symbol  $\otimes$  in the second line is used to signify the probability of obtaining both an SVX and SLT tag in the same event.

Double SVX Tag Probability per Event (%)		
Process	Class I	Class II
$W(Z)b\bar{b}$	$1.9 \pm 0.5$	$3.7 \pm 1.0$
$t\bar{t}$	$12.0 \pm 2.4$	$16.4 \pm 3.2$

Table 4.6: The probability per event to have two SVX-tagged jets for  $W(Z)b\bar{b}$  background processes and for  $t\bar{t}$  events. Double SVX-tag probabilities for all other background processes are negligible and are set to zero. The probabilities are evaluated for class I and class II events.

The computation of the expected  $t\bar{t}$  fraction in each of the mass subsamples proceeds as follows. First, for each mass subsample, we calculate

the expected  $t\bar{t}$  fraction in each event class. Then, the  $t\bar{t}$  fractions for class I and II events are combined into a single  $t\bar{t}$  fraction. For each class, the expected  $t\bar{t}$  fraction,  $g^m$ , in mass subsample  $m$  is given by the following expression:

$$g^m = \frac{N_{t\bar{t},exp}^m}{N_{tot,exp}^m} \quad (4.6)$$

An expression of this form applies to both class I and class II events in each mass subsample. The numerator,  $N_{t\bar{t}}^m$  is the expected number of  $t\bar{t}$  events in mass subsample  $m$ , and the denominator is the expected total number ( $t\bar{t}$  + background) of events. The expected total number of events in subsample  $m$  is calculated using an expression of the form shown in Eq. 4.1 (replace  $j$  with  $m$ , and use the tagging probabilities appropriate for the mass subsamples). The  $t\bar{t}$  fractions for each event class in mass subsample  $m$  are then combined into a single  $t\bar{t}$  fraction,  $f_{t\bar{t}}^m$ , using the following expression:

$$f_{t\bar{t}}^m = \frac{N_I^m g_I^m + N_{II}^m g_{II}^m}{N_I^m + N_{II}^m}. \quad (4.7)$$

Here,  $N_I^m$  and  $N_{II}^m$  are the observed numbers of events, and  $g_I^m$  and  $g_{II}^m$  are the predicted fractions of  $t\bar{t}$  events in the two event classes in subsample  $m$ . The expected number of  $t\bar{t}$  events is given simply by the numerator of Eq. 4.7. For the No Tag mass subsample we have  $f_{t\bar{t}}^m = g_{II}^m$ , because only class II events contribute. Table 4.7 shows the observed number of events, the expected total number of events ( $t\bar{t}$  + background) and the expected contribution from  $t\bar{t}$  alone. Note that the total number of  $t\bar{t}$  events in each class is the same as that of Table 4.4 as expected.

The  $f_{t\bar{t}}^m$  have both statistical and systematic uncertainties. The statistical uncertainties are asymmetric, and are convoluted with the systematic uncertainties separately for classes I and II, and the results are in turn convoluted. The systematic uncertainties are assumed to be Gaussian. The end result is a likelihood function for each  $f_{t\bar{t}}^m$ , which is used in the mass likeli-

Subsample	Class I			Class II		
	Total	Total	$t\bar{t}$	Total	Total	$t\bar{t}$
	Obs.	Exp.	Exp.	Obs.	Exp.	Exp.
SVX Double	3	1.5	1.4	2	4.8	4.7
SVX Single	3	5.3	3.7	12	10.7	9.6
SLT (no SVX)	6	4.2	1.2	8	4.8	2.8
No Tags	75	76.0	5.2	42	43.8	11.4
Total	87	87	11.5	64	64	28.5

Table 4.7: The number of observed events,  $N_{obs}$ , in the mass subsamples, the total expected number of events, and the expected number of  $t\bar{t}$  events. Events in class I with No Tags are not used in the top quark mass analysis.

hood fit described in Section 7. These negative-log-likelihood distributions as a function of the expected number of background events are shown in Fig. 4.1.

Finally, the estimated composition of each mass subsample can be calculated from the  $f_{t\bar{t}}^m$  values and the various tagging probabilities and event rates. The result is shown in Table 4.8. The contributions from mistags are included in the sums for each process. From the Table we see that 80% of the background is from  $W$ +jets and  $Z$ +jets, and another 15% is from non- $W/Z$  events, i.e., from multijets (including  $b\bar{b}$  events). The remaining 5% is from diboson events,  $Z \rightarrow \tau\tau$ , and single-top production. The background fraction per subsample varies from 4% for SVX Double tagged events to 73% for No Tag events.

Item		SVX	SVX	SLT		
#	Process	Single	Double	(no SVX)	No Tags	Total
1	non- $W/Z$	0.5	0.0	1.0	4.6	6.1
2	$WW$	0.1	0.0	0.1	0.6	0.8
3	$WZ$	0.0	0.0	0.0	0.1	0.1
4	$ZZ$	0.0	0.0	0.0	0.1	0.1
5	$Z \rightarrow \tau\tau$	0.1	0.0	0.2	0.5	0.8
6	Single Top	0.2	0.0	0.1	0.2	0.4
7	$Wc + Zc$	0.2	0.0	0.8	1.7	2.7
8	$Wb\bar{b} + Zb\bar{b}$	0.8	0.2	0.4	1.1	2.5
9	$Wc\bar{c} + Zc\bar{c}$	0.4	0.0	0.8	2.0	3.2
10	$W/Z + u, d, s$	0.2	0.0	4.1	19.6	23.9
Background sum		$2.4^{+0.8}_{-0.7}$	$0.2 \pm 0.1$	$7.6 \pm 1.3$	$30.4^{+4.3}_{-4.7}$	40.7
11	$t\bar{t}$	12.6	4.8	6.4	11.6	35.3
Observed events		15	5	14	42	76

Table 4.8: Expected composition (in events) for the four mass subsamples from various processes. The  $W$ +jets and  $Z$ +jets processes have been summed together. The No Tag subsample only includes contributions from class II, as only these events are used in the top quark mass analysis.

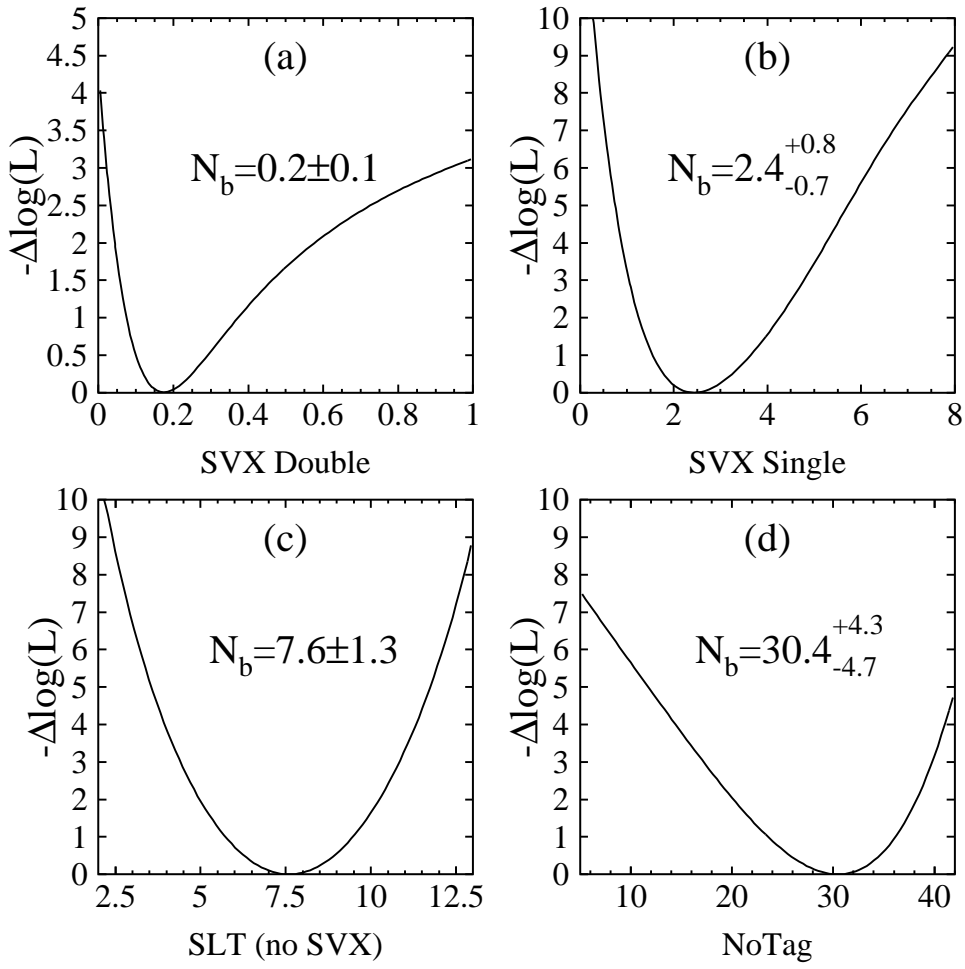


Figure 4.1: The negative log-likelihood function for obtaining a given number of background events in each mass subsample: (a) SVX Double tags, (b) SVX Single tags, (c) SLT (no SVX) tags, and (d) No Tag events.

# Section 5

## CORRECTIONS TO RAW CALORIMETER ENERGIES

Calorimeter information is used to estimate the jet momenta and the net transverse momentum of the particles recoiling against the  $t\bar{t}$  system. This section details how those estimates are made. The signal from each calorimeter tower is converted into a raw [48] energy estimate. Tower energies are then used to evaluate the total energy in the event and other quantities used in the top mass analysis. The raw measurements are corrected for non-instrumented regions, non-linear response of the calorimeter, multiple interactions at high luminosity, and other effects, before a constrained fit is applied to the  $t\bar{t}$  candidate events. Also in this section checks of the jet energy scale are discussed, this being the source of the largest systematic uncertainty in the measurement of the top quark mass.

### 5.1 Jet corrections and their uncertainties

The raw momentum of a jet is calculated by adding vectorially the momenta from all the towers belonging to the jet cluster (see Section 3.2).

Tower momenta are calculated from tower energies with the assumption that they are energies of particles with zero mass [49] that originate from the reconstructed primary vertex and are located at the center of the tower. To measure the top quark mass from candidate  $t\bar{t}$  events, corrections are applied to the raw jet momenta in order to obtain estimates of the momenta of the daughter partons in the  $t\bar{t}$  decay. The corrections occur in two stages.

- A set of “flavor-independent” corrections [33] is applied to all jets with raw  $E_T > 8$  GeV.
- A second set of corrections, specific to  $t\bar{t}$  events, is applied to the leading four jets which are assumed to be the daughter jets from the  $t\bar{t}$  decay. These corrections are applied after the flavor-independent corrections, and map the measured jet momenta to the momenta of the partons in the  $t\bar{t}$  decay.

A description of the corrections to the raw jet momenta is the focus of this section.

### 5.1.1 Flavor-independent jet corrections

To account for detector and reconstruction effects, raw jet transverse momenta are corrected using a set of “flavor-independent” jet corrections [33]. The following expression includes all the corrections applied:

$$P_T(R) = (P_T^{raw}(R) \times f_{rel} - UEM(R)) \times f_{abs}(R) - UE(R) + OC(R). \quad (5.1)$$

The parameter  $R = \sqrt{(\Delta\eta)^2 + (\Delta\phi)^2}$  is the cone radius chosen for the jet measurement;  $R=0.4$  for this analysis. The corrections are described below:

- $f_{rel}$ , the relative energy scale, corrects for non-uniformities in calorimeter response as a function of  $\eta$ .



- $UEM(R)$  takes into account energy due to multiple interactions in the event.
- $f_{abs}(R)$ , the absolute energy scale, maps the raw jet energy observed in a cone of radius  $R$  into the average true jet energy. This average is determined in the central calorimeter assuming a flat  $P_T$  spectrum.
- $UE(R)$  takes into account the energy due to the underlying event, i.e., the energy from the primary  $p\bar{p}$  interaction due to fragmentation of partons not associated with the hard scattering,
- $OC(R)$ , corrects for the energy expected to be outside the cone radius of 0.4.

The  $f_{abs}(R)$  and the  $OC(R)$  corrections are functions of the transverse momentum of the jet. The relative correction is primarily dependent on the pseudorapidity of the jet, with only a weak dependence on the jet momentum.

The reconstruction of jets starts with the raw clustered energy,  $P_T^{raw}(0.4)$ . An uncertainty of  $\pm 1\%$  is assigned to the stability of the calorimeter over the course of the data taking period. This systematic uncertainty was evaluated by comparing the response of the calorimeter to single charged tracks between data from Run 1 and data from the 1988–1989 run, which was used for the energy calibration discussed later. No systematic difference was observed. Also the raw inclusive jet cross section [50] obtained with the 1988-1989 data run was compared with that of the Run 1a data (after correcting for multiple interactions) and it was found that the ratio was consistent with unity at the 5% level. Because of the rapidly falling  $E_T$  spectrum, this corresponds to an upper limit on a difference in the energy scale of 1%.

The relative correction is derived from di-jet balancing data and corrects for the relative response of the different calorimeter sections to that of the calorimeter in the central region ( $0.2 < |\eta| < 0.7$ ) [49]. The plug

Uncertainty on	
$ \eta $ range	relative correction
0.0 – 0.1	2.0 %
0.1 – 1.0	0.2 %
1.0 – 1.4	4.0 %
1.4 – 2.2	0.2 %
2.2 – 2.6	4.0 %
2.6 – 3.4	0.2 %

Table 5.1: The percentage uncertainty on the relative jet energy correction for various detector  $\eta$  ranges. The cracks in  $\eta$  between different detectors are located near  $\eta=0$ , 1.2, and 2.4, and have larger uncertainties than the regions away from the cracks.

( $1.1 < |\eta| < 2.4$ ) and forward ( $2.4 < |\eta| < 4.2$ ) regions are thus calibrated. The precision to which this calibration is known is limited mostly by the number of di-jet events available. The effects of different resolutions of the central and plug calorimeters on the energy measurements were studied using Monte Carlo simulation and are properly included. The uncertainty is larger near the cracks between the different detectors due to smaller statistics and worse energy resolution. Table 5.1 gives the uncertainty (in %) on the relative corrections for various detector  $\eta$  ranges.

The corrections for multiple interactions ( $UEM$ ) in the same event and the underlying event ( $UE$ ) in the primary interaction are derived from minimum bias data. The average number of interactions in Run 1a ( $N_v=0.6$ ) is different from that of Run 1b ( $N_v=1.8$ ), hence a different procedure is used for the two samples. For the Run 1a sample, 0.72 GeV/ $c$  is subtracted from the jet  $P_T$  after the absolute correction and accounts for both effects on average. For Run 1b, the effects of the underlying event and additional interactions are separated. To account for multiple interactions, prior to the absolute correction, 0.297 GeV/ $c$  is subtracted from the jet  $P_T$  for each additional

reconstructed vertex in the event. This correction is obtained by studying the amount of energy in the event as a function of the number of vertices over the course of the run. For the underlying event ( $UE$ ), we subtract 0.65 GeV/ $c$  from each jet after the absolute correction.

The uncertainty on the  $UEM$  correction is estimated to be 100 MeV/ $c$  for each vertex in the event. The uncertainty in the  $UE$  correction is evaluated by looking at variations in the energy density at  $\pm 90^\circ$  with respect to the two jets in di-jet events when varying the maximal  $E_T$  threshold on the third jet from 5 to 15 GeV. Based on these studies, we assign a  $\pm 30\%$  relative uncertainty to the underlying event correction [49, 33]. For jets with  $P_T > 20$  GeV/ $c$  the uncertainty is typically less than 0.5% of the jet's  $P_T$ , as shown in Fig. 5.1.

The absolute correction is derived from data and Monte Carlo plus detector simulation. The simulation includes many features of the CDF calorimeters, the main ones being: non-linearity, cracks and less sensitive regions, single tower thresholds. The response of the calorimeter to incident pions and electrons is studied using testbeam data, minimum bias runs, special runs which triggered on events containing single isolated tracks, as well as standard data runs. The detector simulation has been tuned to agree with these data. The step from individual particle response to jets is achieved by tuning the Monte Carlo (ISAJET) fragmentation parameters to reproduce a number of distributions observed in di-jet data: number of charged particles, spectra and invariant mass of charged particles, and the ratio of charged to neutral energy [33]. The derived correction then accounts for non-linearity of the calorimeter, energy losses near the boundaries of different calorimeter wedges, response variation as a function of the position along the wedge and all the other effects included in the simulation. The absolute correction,  $f_{abs}(0.4)$ , as a function of corrected jet  $P_T$ ,  $P_T^{cor}$ , is shown in Fig. 5.2(a).

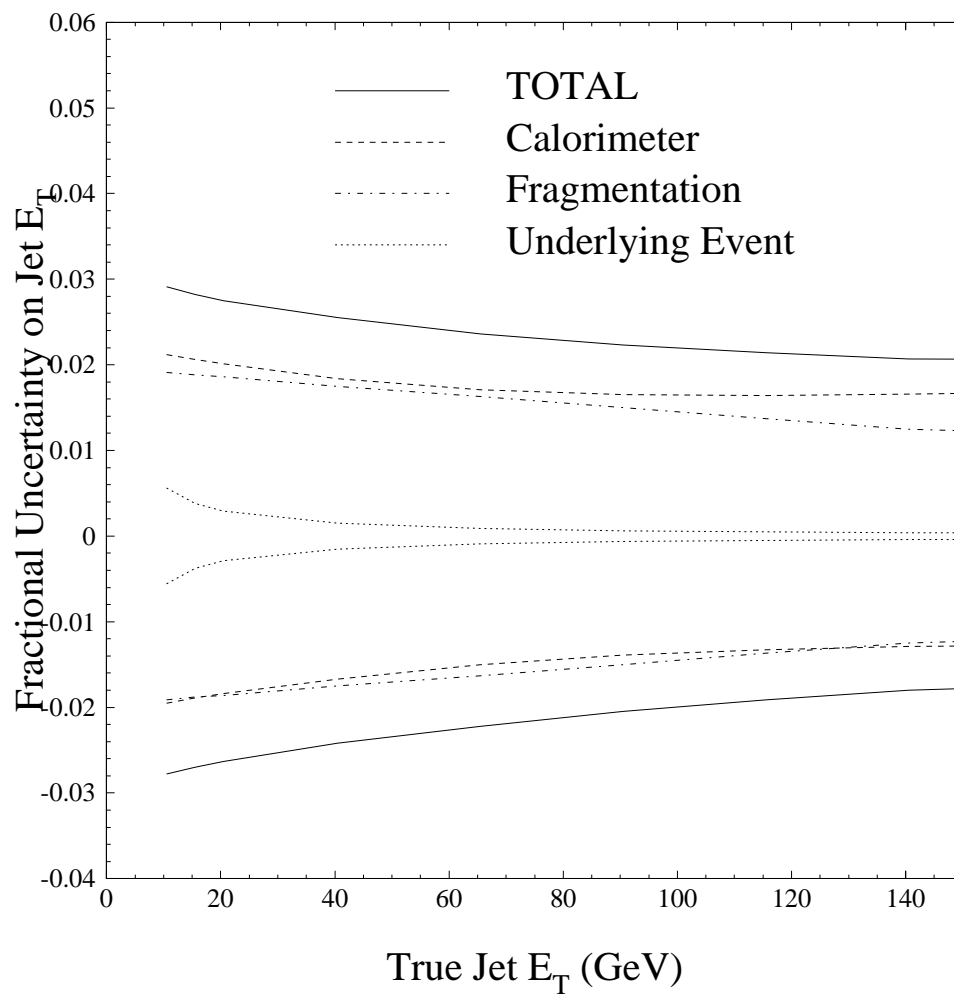


Figure 5.1: Uncertainty in jet  $E_T$  scale as measured with a jet clustering cone of size 0.4. The vertical axis shows the extent to which the measured jet  $E_T$  response varies due to different systematic effects.

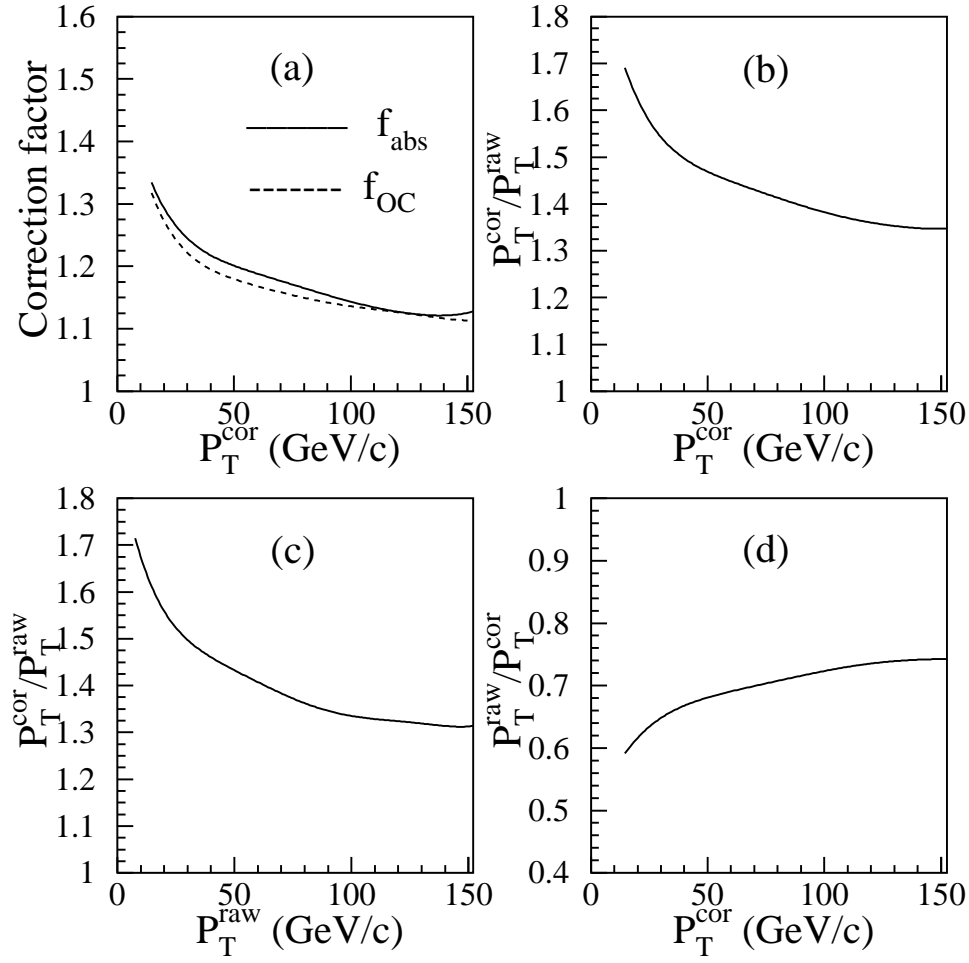


Figure 5.2: “Flavor-independent” jet corrections, for a jet clustering cone of  $R=0.4$ . (a) Absolute correction,  $f_{abs}$ , and out-of-cone correction factor,  $1+OC/P_T$ , versus corrected jet  $P_T$ ,  $P_T^{cor}$ . (b) Total correction,  $P_T^{cor}/P_T^{raw}$ , as a function of  $P_T^{cor}$ . (c) total correction,  $P_T^{cor}/P_T^{raw}$ , as a function of  $P_T^{raw}$ . (d) fraction of measured momentum,  $P_T^{raw}/P_T^{cor}$  versus  $P_T^{cor}$ .

The systematic uncertainty in the absolute correction is attributed to (a) calorimeter response, and (b) fragmentation related effects [49, 33] (see Fig. 5.1). The parameters that describe the calorimeter's response to incident electrons, photons and pions have uncertainties due to finite statistics and assumptions which are made. For example, at low momentum ( $|p| < 5 \text{ GeV}/c$ ), the largest source of uncertainty in the charged pion response comes from the estimation of the amount of energy in the shower from  $\pi^0$ 's. Additional uncertainty comes from the uncertainty in the relative response across the face of a calorimeter cell and the energy deposition in cracks between calorimeter cells. The uncertainty in the calorimeter's response to photons is assigned to be the same as for electrons. Uncertainty in the fragmentation parameters comes from the modeling of the tracking efficiency in jets, and the level of agreement between the simulation and data.

The contributions to the jet  $E_T$  uncertainty from these sources are evaluated by shifting the input values of these parameters by  $+1$  and  $-1$  standard deviation ( $+1\sigma$  and  $-1\sigma$ ), and calculating the resulting shift in the reconstructed jet energies. For (a) we separately vary the pion, electron, and photon responses by  $+1\sigma$  and  $-1\sigma$ , and add the resulting shifts in the jet energies in quadrature. For (b), we vary the charged tracking efficiency by its uncertainty and reevaluate a new set of fragmentation parameters. These new fragmentation parameters are in turn varied one at a time, and the resulting deviations in the jet energies are added in quadrature.

The systematic uncertainties in the jet  $E_T$  scale from the sources (a) and (b), as well as from the UE correction are shown in Fig. 5.1. The total systematic uncertainty from these three sources is obtained by adding in quadrature the three curves, and is shown as the solid curve in Fig. 5.1.

The out-of-cone correction was derived from a Monte Carlo simulation and accounts for the energy falling outside the jet cone [49]. This study was done with light quarks; the  $t\bar{t}$  specific corrections take into account dif-

ferences with heavy flavor jets. The amount of energy outside the cone of  $R=0.4$  is related to emission of low energy gluons from the initial partons, and is referred to as “soft gluon” radiation. The correction factor,  $f_{OC} = 1 + OC(0.4)/P_T(0.4)$ , is a function of the jet  $P_T$  corrected for all other effects and is given by the equation,

$$f_{OC} = 1.0 + \frac{23.0 (1.0 - 0.915 e^{-0.0074 P_T})}{P_T}. \quad (5.2)$$

The correction factor is shown in Fig. 5.2(a).

The systematic uncertainty on the jet momentum from the OC correction originates from the uncertainty in modeling the radiation of low energy gluons in parton showers. To estimate this uncertainty, we use  $W+1$  jet data and a HERWIG Monte Carlo simulation of  $W+1$  jet events to compare the energy contained in an annulus with radii of 0.4 and 1.0 around the jet direction. We define a variable  $F$ ,

$$F = \frac{P_T(1.0) - P_T(0.4)}{P_T(0.4)} \quad (5.3)$$

where  $P_T(0.4)$  and  $P_T(1.0)$  are the jet momenta corrected using the corrections described above (note that Eq. 5.2 is used for  $R=0.4$ ; for  $R=1.0$  the correction is much smaller). The quantity  $F$  is the fractional difference of the momentum in an annulus with radii between 0.4 and 1.0, calculated for each event using the calorimeter towers in that annulus or using the average OC correction. A comparison of data and Monte Carlo tests the agreement between the Monte Carlo soft gluon radiation modeling and what is observed in the data in that annulus. Figure 5.3 shows the mean value of  $F$  as a function of the corrected  $P_T$  (corrected using a cone size of 0.4) for data and Monte Carlo. There is a clear difference between the two distributions. This implies that the jet shapes in data and Monte Carlo disagree at the few % level. The difference between HERWIG and data is shown in Fig. 5.4. We take this difference as

the uncertainty on the out-of-cone correction. Its effect on the top quark mass measurement is referred to as the systematic uncertainty from soft gluon radiation.

Similar distributions have been obtained for other sets of data, namely  $Z + 1$  jet data and jet data with two  $b$ -tagged jets. Since the statistics for the latter sets of data are low, only the  $W+1$  jet data are used. A fit to the points of Fig. 5.4 gives a maximum (upper dotted curve) uncertainty of  $\delta P_T/P_T = \exp(2.467 - 0.074P_T) + 1.438$  (in %). It can be seen that for jets typical of those produced in  $t\bar{t}$  events ( $\approx 30 - 90$  GeV for  $M_{top} = 175$  GeV/ $c^2$ ), the difference between HERWIG and data is  $< 2\%$ . For softer jets, the difference is closer to 4%.

The systematic uncertainty assigned to the soft gluon radiation accounts for differences in the energy contained in the annulus  $0.4 < R < 1.0$  between data and the Monte Carlo simulation. For the additional energy which falls outside a cone of 1.0, we assign an uncertainty of  $\pm 1$  GeV. We refer to this energy as “splash-out”.

In summary, Figure 5.2 shows some of the flavor-independent jet corrections and their  $P_T$  dependence. Figure 5.2(a) shows the absolute and out-of-cone correction factors as a function of the corrected jet  $P_T$ . They vary from  $\approx 1.3$  at  $P_T = 15$  GeV/ $c$  to  $\approx 1.12$  for  $P_T > 100$  GeV/ $c$ . Figure 5.2(b) shows the ratio of the fully corrected jet  $P_T$  ( $P_T^{\text{cor}}$ ) to the raw jet  $P_T$  ( $P_T^{\text{raw}}$ ) as a function of the fully corrected jet  $P_T$ . Jets from  $t\bar{t}$  events typically have a  $P_T$  of  $\approx 30 - 90$  GeV/ $c$ , for which the average jet correction factor is  $\approx 1.45$ . Figure 5.2(c) shows the correction factor as a function of  $P_T^{\text{raw}}$ . Finally, Fig. 5.2(d) shows the fraction of momentum measured in the detector before the jet corrections as a function of the corrected jet  $P_T$ . Figure 5.5 shows the overall systematic uncertainty as a function of the corrected  $P_T$  of the jets. In the 30-90 GeV/ $c$  range, the systematic uncertainty on jet energies is about 4%.



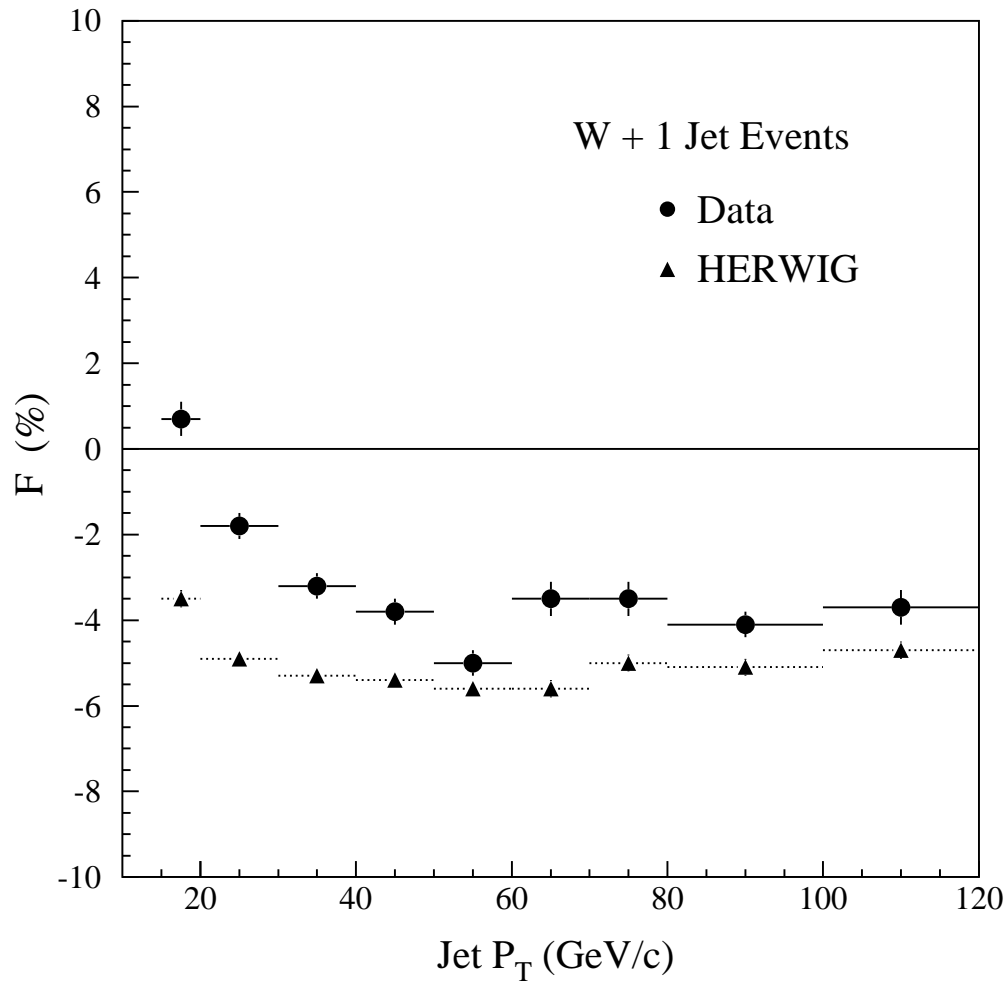


Figure 5.3: Fractional difference in corrected jet  $P_T$  obtained using cone radii of 0.4 and 1.0 as a function of the corrected jet  $P_T$  from  $W+1$  jet events. The circles are the results from the data sample and the triangles are from a sample of HERWIG Monte Carlo events which have been processed through the CDF detector simulation.

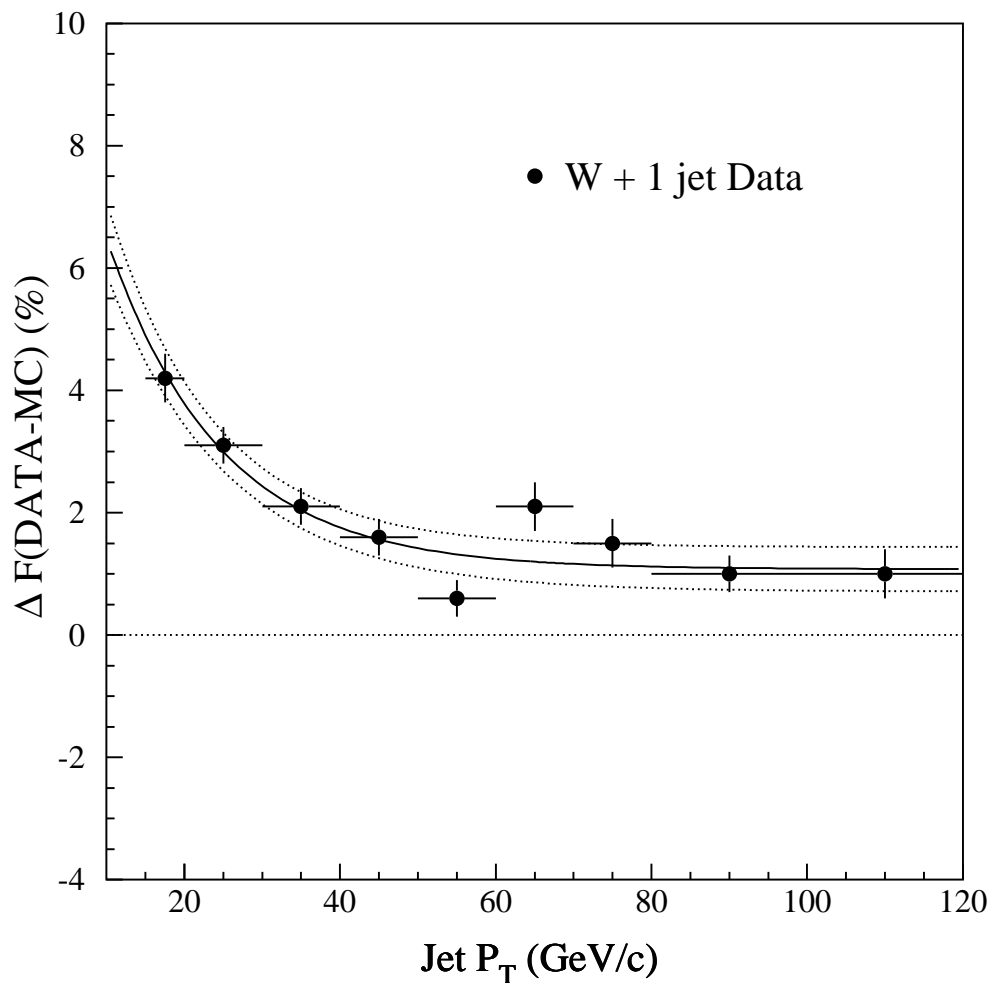


Figure 5.4: Systematic uncertainty on the out-of-cone correction as obtained in  $W+1$  jet events. The abscissa is the fully corrected jet  $P_T$  using a clustering cone of 0.4. The vertical axis is the difference between data and Monte Carlo of the variable  $F$  described in the text. The full curve represents a fit through the data points, the dotted curves were obtained using the one standard deviation values of the fit parameters.

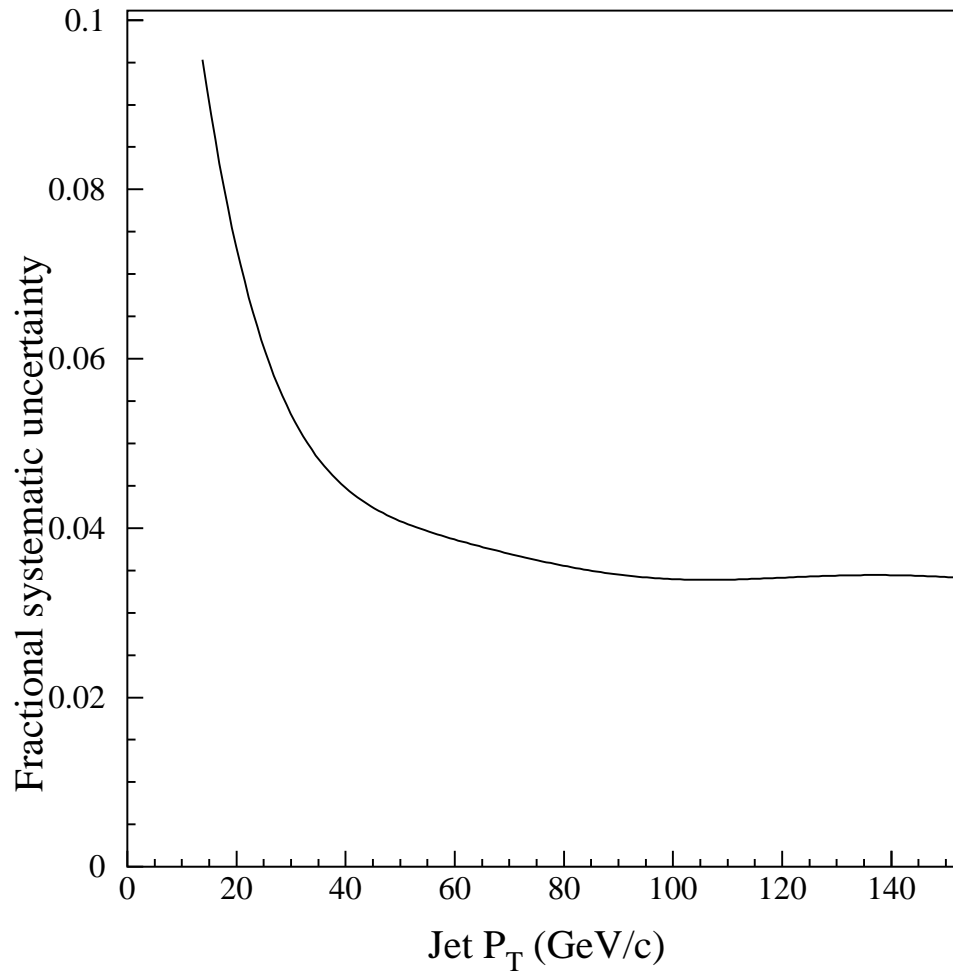


Figure 5.5: Total systematic uncertainty on jets as a function of the corrected jet  $P_T$ .

### 5.1.2 Checks on the jet $E_T$ scale and its uncertainty

The procedures used to obtain the jet corrections and their systematics have been checked by applying them to  $Z + 1$  jet events, where the  $Z$ -boson decays into either  $e^+e^-$  or  $\mu^+\mu^-$ . The energy scale for electrons and the momentum scale for muons are known to a precision of 0.14% and 0.065% respectively [31]. In the absence of initial state radiation, such events are expected to have zero net transverse momentum. The jet in each event is corrected according to the previous prescription, and the quantity

$$F_b = \frac{P_T(Z) - P_T(\text{jet})}{P_T(Z)} \quad (5.4)$$

is calculated, where  $P_T(Z)$  is in the range 30-150 GeV/ $c$ . The lower limit was chosen to avoid biases due to the sample selection. The jet recoiling against the  $Z$  boson is required to have an uncorrected  $E_T \geq 8$  GeV and  $|\eta| < 2.4$ . To test the jet energy scale we need a clean environment, i.e., events in which there is only one jet recoiling against the  $Z$  boson. We therefore require that any additional calorimeter cluster have an uncorrected energy  $E_T < 6.0$  GeV (at any  $\eta$ ).

To separate detector effects from those due to gluon radiation in the initial state, we use the component analysis first suggested in Ref [51]. We compute the direction of the bisector between the  $Z$  and the jet directions in the transverse plane. The “parallel component” of  $F_b$  is then defined to be the component perpendicular to the bisector. Balancing the jet against the  $Z$  along this component will give information about the jet energy scale. Figure 5.6 shows the distribution of this component of  $F_b$  in  $Z + 1$  jet events for data and Monte Carlo. The difference in the medians of the two distributions is:

$$(\Delta F_b)_\parallel = (3.2 \pm 1.5(stat) \pm 4.1(syst))\%. \quad (5.5)$$

The 4.1% systematic uncertainty was calculated using the jet energy uncertainties discussed in the previous section. We conclude that any possible energy

scale shift detected by this check is compatible with zero within the evaluated uncertainties.

### 5.1.3 Jet momentum corrections for $t\bar{t}$ events

The  $t\bar{t}$  specific jet momentum corrections are designed to make an average correction to the jet momenta to obtain an estimate of the original parton momenta [1]. The  $P_T$  spectra of partons from HERWIG generated  $t\bar{t}$  events which pass our experimental selection cuts are shown in Fig. 5.7. The  $t\bar{t}$ -specific corrections account for (a) the difference in the  $P_T$  spectrum between top induced jets and the flat spectrum used to derive the flavor-independent corrections, (b) the energy lost through semileptonic  $b$  and  $c$ -hadron decays, and (c) the multi-jet final state of  $t\bar{t}$  events as compared to di-jet final state used to derive the flavor-independent corrections. The correction for these three effects are derived using the HERWIG Monte Carlo generator with an input top quark mass of 170 GeV/ $c^2$ . The generated events are processed using the CDF simulation and reconstructed in the same way as the data sample. An average correction factor is determined by first matching (in  $\eta - \phi$  space) the reconstructed jets with the generated partons, and then comparing the reconstructed jet  $P_T$  (after the flavor-independent corrections) with the original parton  $P_T$ . The correction is given by the median of the distribution of  $\Delta = (P_T(parton) - P_T(jet))/P_T(jet)$ . This is done as a function of the reconstructed jet  $P_T$ .

Figure 5.8 shows the size of the  $t\bar{t}$ -specific correction factors for four types of jets: (A) jets from hadronic  $W$  decays, (B) average  $b$  jets (no selection on decay mode) (C)  $b$  jets containing an electron, and (D)  $b$  jets containing a muon. The general shape of each curve is primarily a result of the difference between using a flat jet  $P_T$  spectrum and the spectrum appropriate for top decays. In particular, this difference is responsible for the rising values of the curves at low  $P_T$ , and the asymptotic values at large  $P_T$ . The larger

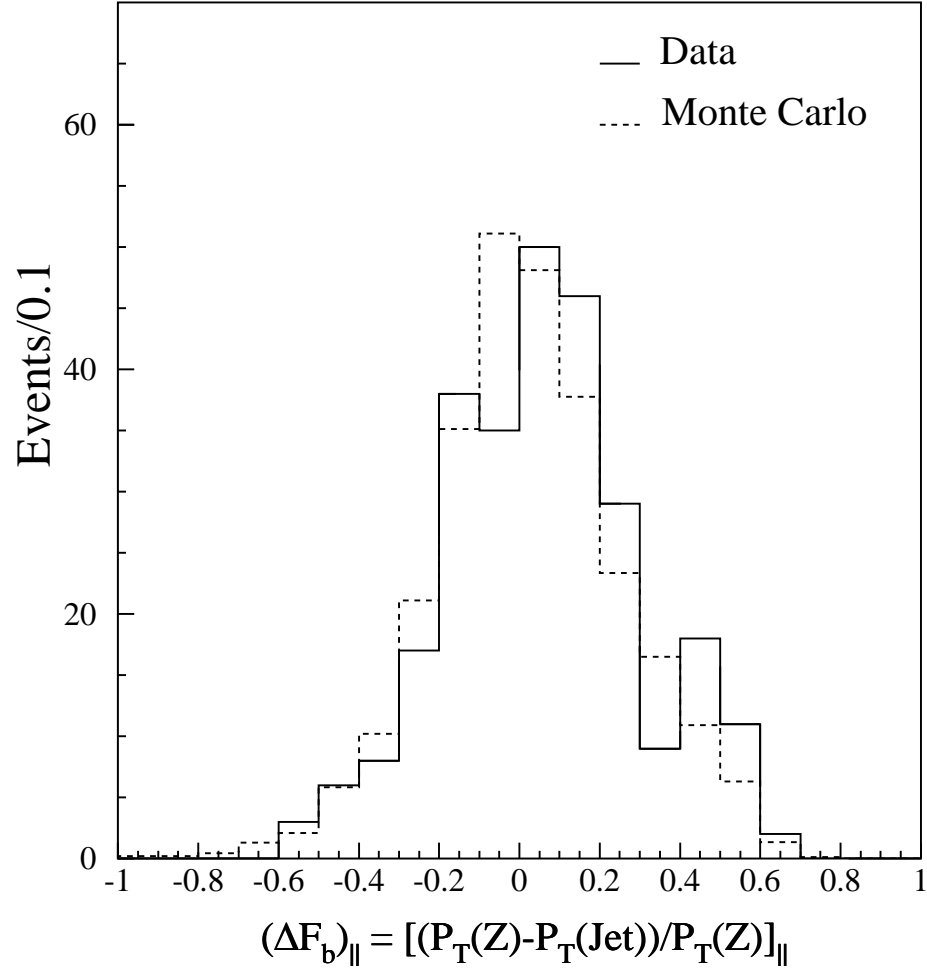


Figure 5.6: Parallel component of transverse momentum imbalance between the  $Z$  and the jet in reconstructed  $Z + 1$  jet candidate events. Both data (solid) and Monte Carlo (dashed) are shown (see text).

corrections applied to the  $b$  jets with a soft lepton are a consequence of the amount of energy carried off by undetected neutrinos, and, for jets containing a  $b \rightarrow \mu\nu X$  decay, of the fact that muons deposit only  $\approx 2$  GeV, on average, in the calorimeter.

The flavor-independent and  $t\bar{t}$ -specific corrections bring the median reconstructed jet  $P_T$  into agreement with the initial parton  $P_T$  in  $t\bar{t}$  events. The uncertainty on the jet  $P_T$  after these corrections is given by the  $\sigma$  of the  $\Delta$  distribution, defined as one half of the separation of the 16th and 84th percentiles of the distribution. For each bin of reconstructed jet  $P_T$ , we obtain the  $\sigma$  of the  $\Delta$  distribution, which is then parametrized as a function of the reconstructed jet  $P_T$ . These uncertainties are shown in Fig. 5.9 for jets from  $W$  decay and  $b$  jets. As above, we display curves for generic  $b$  jets (no selection on decay mode), for jets containing an electron, and for jets containing a muon. These jet  $P_T$  uncertainties are input into the kinematic mass fitter (see Section 6) and dictate how much the jet energies can be altered to accommodate the applied constraints.

The jet corrections described above are applied only to the four highest  $P_T$  jets in the event, which are assumed to be daughters of the  $t$  and  $\bar{t}$  decays. Any additional jets beyond the leading four jets are corrected only with the “flavor-independent” corrections (excluding the out-of-cone corrections, see Section 5.2) and are assigned an uncertainty of  $0.1P_T \oplus 1$  GeV/ $c$ . This curve is also shown in Fig. 5.9.

#### 5.1.4 Summary of systematic uncertainties on jet energy measurements

A number of corrections are performed to estimate the original parton momenta from the observed jets. The jet energy scale uncertainty is evaluated from the uncertainties in the corrections for calorimeter stability, multiple

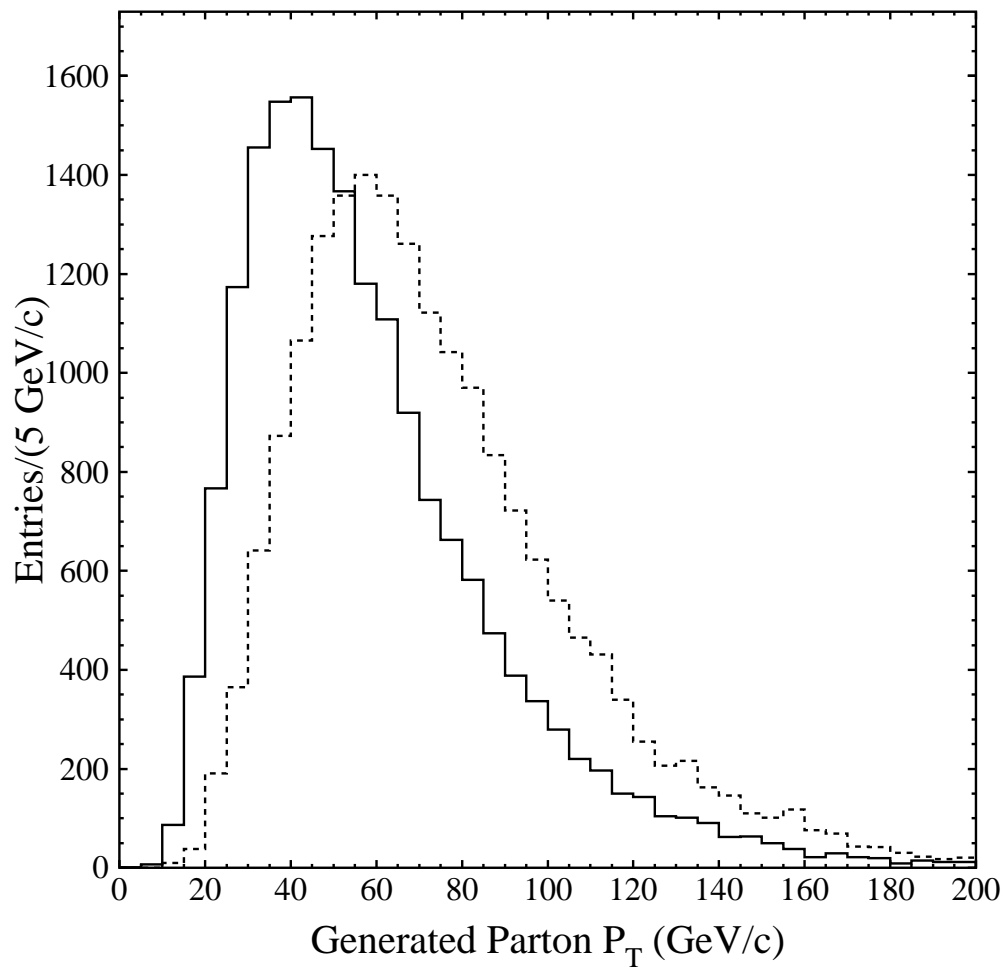


Figure 5.7:  $P_T$  distributions for partons from top quark decays obtained from the HERWIG Monte Carlo program after simulation of detector response and including the effects of the Top Mass Candidate Sample data selection. The solid line indicates the distribution for light quarks from the  $W \rightarrow q\bar{q}'$  decay and the dashed line is the distribution for  $b$  quarks.



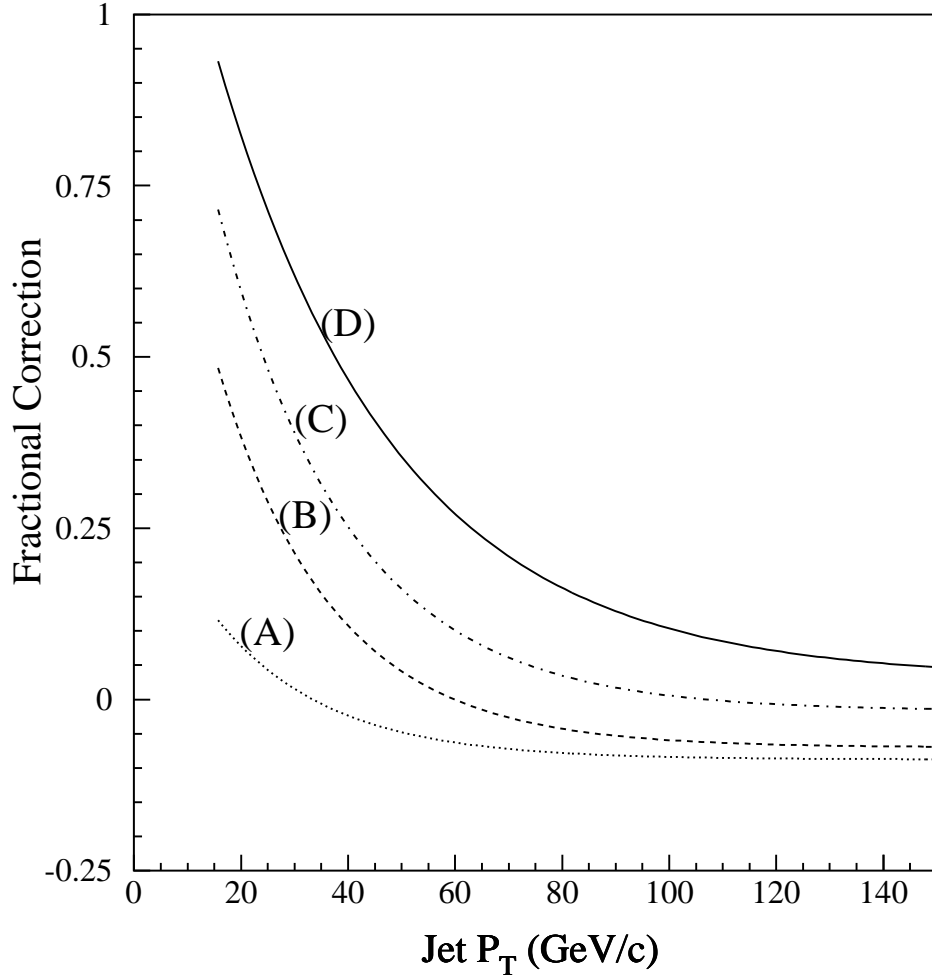


Figure 5.8: The  $t\bar{t}$ -specific corrections applied to jets according to available  $b$ -jet information. The curves show the fractional change to the corrected jet  $P_T$  after all “flavor-independent” jet corrections have been applied. The curves are for: (A) jets from the decay of  $W$  bosons, (B) jets from all  $b$  quarks (no selection on decay mode), (C) jets from  $b$  quarks containing an electron, and (D) jets from  $b$  quarks containing a muon.

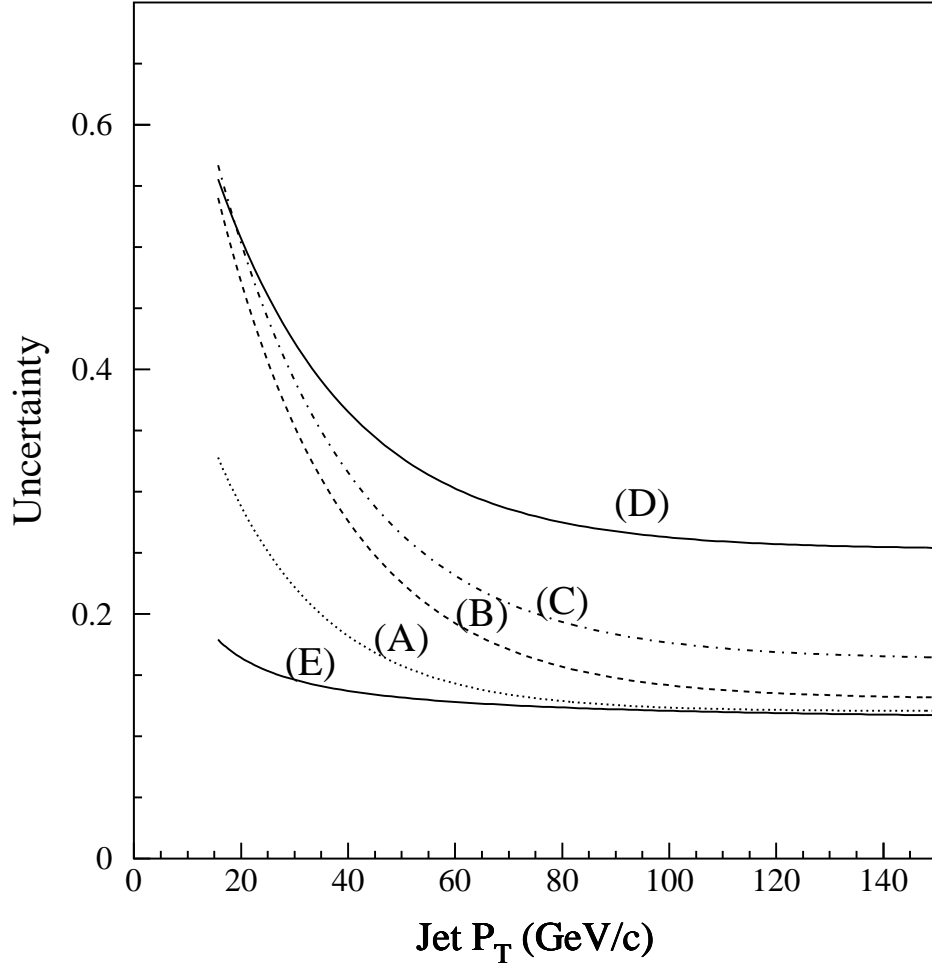


Figure 5.9: Fractional uncertainty in the estimated parton  $P_T$  as a function of the jet  $P_T$  after the flavor-independent jet corrections are applied. The uncertainty shown on the vertical axis is given as a fraction of the jet  $P_T$ . Curves (A) through (D) have the same meaning as for the previous figure. The curve labeled (E) is used for the jets beyond the four highest- $P_T$  jets and is applied only to the  $P_T$  within the cone of radius  $R=0.4$ .

interactions, calorimeter response, jet fragmentation, underlying event, out-of-cone correction, and splash out. Figure 5.5 shows the dependence of the overall jet energy scale uncertainty on the corrected jet  $P_T$ . The total systematic uncertainty varies between 7% for jets with corrected  $P_T$  of 20 GeV/ $c$  and 3.5% for jets with  $P_T=150$  GeV/ $c$ .

We do not assign a separate systematic uncertainty to the top specific corrections. Such uncertainties may arise from modeling of initial and final state gluon radiation, and modeling of the primary parton collision. We discuss these uncertainties in Section 9.

## 5.2 Measurement of other calorimeter variables

To measure the top mass we apply energy-momentum conservation to the process  $p\bar{p} \rightarrow t\bar{t} + X$ , with subsequent decay of the  $t$  ( $\bar{t}$ ) into  $W + b$  ( $\bar{b}$ ) (see Section 6). Here,  $X$  is the unspecified particles which recoil against the  $t\bar{t}$  system. The calorimeter provides the measurement of  $X_T$ , the transverse momentum of  $X$ . The quantity  $X_T$  is computed from the energy left over after the lepton and the four jets from the  $t\bar{t}$  system are removed from the total measured energy. This leaves two terms:

$$\vec{X}_T = \vec{U}_T + \sum_{i=5}^{N_{jets}} \vec{E}_T(jet) \quad (5.6)$$

Each component of the unclustered energy,  $\vec{U}_T$ , is defined as the vector sum of the energies in the calorimeter towers after excluding the primary lepton and all the jets with raw  $E_T > 8$  GeV and  $|\eta| < 3.4$  in the event. Using a  $t\bar{t}$  Monte Carlo ( $M_{top}=175$  GeV/ $c^2$ ) we find a distribution in  $U_x$  with  $\langle U_x \rangle \sim 0$  and  $\sigma = 15.8$  GeV for events which enter into the mass subsamples. The same distribution for the data has a mean consistent with 0 and a  $\sigma = 14.9$  GeV. The Monte Carlo and data distributions in  $U_x$  are shown in Fig. 5.10. Similar results are obtained for the  $y$  component.

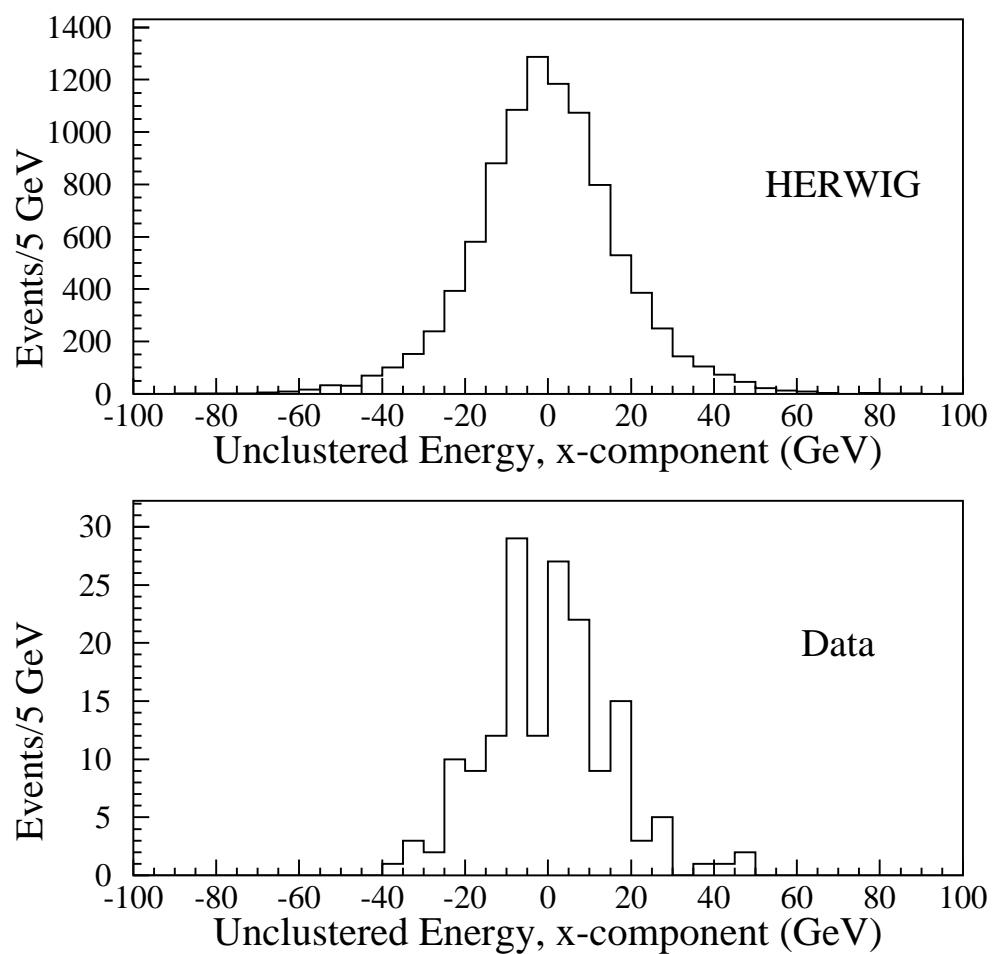


Figure 5.10: Unclustered energy for the mass sample used here and for  $t\bar{t}$  Monte Carlo ( $M_{top} = 175 \text{ GeV}/c^2$ ). Only the  $x$  component is shown.

Each component of the unclustered energy is corrected with a single factor  $f_{u.e.} = 1.6$ , based on studies of the recoil energy that the calorimeter measures in  $Z$ -boson events with no extra jets, where the  $Z$  boson is well measured by the two leptons it decays into [52]. The final mass value is not sensitive to the value of  $f_{u.e.}$ . For example, using  $f_{u.e.} = 2.0$  makes a negligible change in the reconstructed top quark mass ( $0.2 \text{ GeV}/c^2$ ), hence it is not included in the Table of systematics in Section 9.7. The uncertainty with which each component of  $\vec{U}_T$  is measured is taken to be 100% (added in quadrature to 1 GeV). The jets beyond the four with the highest  $E_T$  are corrected only within the cone of 0.4, so as to avoid counting the out of cone energy twice (it is already included in the unclustered energy). The uncertainties on these jet energies were discussed in Section 5.1.3 and shown in Figure 5.9.

Another quantity that can be estimated from the calorimeter measurement is the  $\cancel{E}_T$ . It is calculated using the following expression:

$$-\vec{\cancel{E}}_T = \vec{E}_T(lepton) + \sum_{i=1}^4 \vec{E}_T(jet) + \vec{X}_T \quad (5.7)$$

The above expression shows that the  $\cancel{E}_T$  measurement is highly correlated with the jet energy measurements, and therefore it is not considered as an independent measurement in the mass fitting. As discussed in Section 6, it is only used as a starting value for the neutrino's transverse momentum when the overall mass fit is performed.

# Section 6

## MASS FITTING

The kinematics of events in the decay channel  $p\bar{p} \rightarrow t\bar{t} \rightarrow \ell\nu q\bar{q}'b\bar{b}X$  are over-constrained by the number of measured quantities and the number of applicable energy-momentum conservation equations of production and decay. This allows for complete reconstruction of the four-momenta of the particles in the decay chain and hence an event-by-event top mass determination.

In this section we discuss the methods used for event reconstruction and then study the validity of the algorithms using  $t\bar{t}$  Monte Carlo events. Effects due to combinatorics, wrong parton assignments and shapes of backgrounds on the top mass measurement are also discussed.

### 6.1 Event reconstruction

The first step in the reconstruction is the estimation of the four-momenta of the decay products of the  $t\bar{t}$  pair: the lepton and the four jets. Electron and muon measurements, resolutions and identification are discussed in section 3.1. The four leading jets, as defined in Section 3.3, are assumed to be the  $q$ ,  $\bar{q}$ ,  $b$ , and  $\bar{b}$  quarks from the  $t\bar{t}$  decay chain. According to a HERWIG Monte Carlo plus detector simulation, this assumption is correct 55–72% of the

time, depending on the number and type (SVX or SLT) of tags (see Table 6.1). The momenta of the reconstructed jets are corrected as described in Section 5. The direction (i.e.,  $\eta$  and  $\phi$ ) of each parton is assumed to be the same as the direction of the associated jet. The masses of the partons are assumed to be  $0.5 \text{ GeV}/c^2$ , except for  $b$  and  $\bar{b}$  quarks which are assigned a mass of  $5.0 \text{ GeV}/c^2$ . The resolutions on the jet energy measurements are discussed in Section 5.

The mass fitting algorithm applies the constraints implied by the production and decay of a  $t\bar{t}$  pair to evaluate an event-by-event mass. The hypothesis of standard model  $t\bar{t}$  implies the production process

$$p\bar{p} \rightarrow t + \bar{t} + X, \quad (6.1)$$

followed by the decays

$$t \rightarrow W^+ + b, \quad (6.2)$$

$$\bar{t} \rightarrow W^- + \bar{b}, \quad (6.3)$$

$$W^\pm \rightarrow \ell^\pm + \nu, \quad (6.4)$$

$$W^\mp \rightarrow q + \bar{q}'. \quad (6.5)$$

The quantity  $X$ , in  $p\bar{p} \rightarrow t + \bar{t} + X$ , represents the unspecified particles recoiling against the  $t\bar{t}$  system. Only two components of  $X$  are measured, as discussed in Section 5.2.

An estimate of the top quark mass is obtained on an event-by-event basis after minimizing a  $\chi^2$ . In general, the  $\chi^2$  definition is not unique, in that any formulation which expresses the constraints implied by the measurements and four-momentum conservation is equally valid. We have chosen a particular formulation of the  $\chi^2$ , which is minimized using the program MINUIT [53]. An alternate method, the SQUAW kinematic fit [54], has also been used and the results are essentially identical. We describe here both of these fitters.

### 6.1.1 Mass fitting using MINUIT

The  $\chi^2$  expression which uses the MINUIT minimization routines applies energy and momentum constraints to the above production and decay chain to obtain six effective constraints: (1,2) the two transverse momentum components of the  $t\bar{t} + X$  system must be zero, (3) the invariant mass of the  $\ell\nu$  system must equal the  $W$ -boson mass,  $M_W$ , (4) the invariant mass of the  $q\bar{q}'$  system must equal  $M_W$ , and (5,6) the two three-body invariant masses must each equal the top quark mass,  $M_t$ . The relevant unmeasured quantities are then the three momentum components of the neutrino and the top quark mass. The system may therefore be solved by minimizing a two-constraint chisquare. The chisquare expression used to obtain the present results is:

$$\begin{aligned} \chi^2 = & \sum_{\ell, jets} \frac{(\hat{P}_T - P_T)^2}{\sigma_{P_T}^2} + \sum_{i=x,y} \frac{(\hat{U}'_i - U'_i)^2}{\sigma_{U'_i}^2} + \frac{(M_{\ell\nu} - M_W)^2}{\sigma_{M_W}^2} \\ & + \frac{(M_{jj} - M_W)^2}{\sigma_{M_W}^2} + \frac{(M_{\ell\nu j} - M_t)^2}{\sigma_{M_t}^2} + \frac{(M_{jjj} - M_t)^2}{\sigma_{M_t}^2}. \end{aligned} \quad (6.6)$$

The notation is as follows:  $\ell$  signifies the primary lepton in the event,  $\nu$  refers to the inferred neutrino, and  $j$  refers to one of the four leading jets in the event. The first sum is over the primary lepton and all jets with raw  $E_T > 8$  GeV and  $|\eta| < 2.4$ . The second sum is over the transverse components of the unclustered energy [28], discussed in Section 5.2, plus those of the energies of jets with  $2.4 < |\eta| < 3.4$ . The hatted symbols in the sums represent quantities altered by the fit procedure, whereas unhatted symbols represent the input values. The uncertainties on the energy of the primary lepton, the jets, and the unclustered energy are discussed in Sections 3.1 and 5. The  $W$ -boson mass,  $M_W$ , is taken to be  $80.4 \text{ GeV}/c^2$  [31],  $\sigma_{M_W}$  is set to  $2.1 \text{ GeV}/c^2$  [55], and  $\sigma_{M_t}$  is set to  $2.5 \text{ GeV}/c^2$ . The results are insensitive to the values used for  $\sigma_{M_W}$  and  $\sigma_{M_t}$ . The quantity  $M_{\ell\nu}$  is the invariant mass of the primary lepton and the neutrino and  $M_{\ell\nu j}$  is the invariant mass of the primary lepton, neutrino, and one of the four leading jets. Of the remaining three jets, we assign two to



the decay products of the  $W$  boson in order to calculate  $M_{jj}$ . The third jet is then combined with the other two jets to form the three body mass  $M_{jjj}$ . The issue of combinatorics is discussed in Section 6.2.

The first two constraints are that the total transverse momentum components of the  $t\bar{t} + X$  system are zero. These constraints are imposed by setting the neutrino transverse momenta to exactly balance the sum of the current  $\hat{P}_T$  and  $\hat{U}'_T$  values. The other four constraints appear as explicit terms in the  $\chi^2$ . This  $\chi^2$  yields two minima which correspond to the two solutions for the neutrino longitudinal momentum in the  $W$  decay. This is referred to as the  $P_z^\nu$  ambiguity. After minimizing this  $\chi^2$  with respect to the collective set of transverse momenta,  $\hat{P}_T$ , for the jets and the charged lepton, the unclustered energy,  $\hat{U}_T$ , the  $z$ -component of the neutrino momentum, and the top mass,  $M_t$ , for the event, we obtain an event-by-event determination of the top quark mass.

### 6.1.2 The SQUAW fitter

The SQUAW fitter is a general kinematic fitting program that can be used for any production and decay processes, provided that there are enough constraints [1, 54]. It has been used to measure the top quark mass in the lepton+jets channel and for the all-hadronic decay channel [10].

In brief, it applies energy-momentum conservation to the five processes (6.1)–(6.5), thus providing 20 equations, i.e., 20 constraints, for the measured quantities and their uncertainties. It uses the measured  $W$  mass,  $M_W = 80.4 \text{ GeV}/c^2$ . In the fit an uncertainty is assigned to the  $W$  mass in order to take into account the expected  $W$  width of  $2.1 \text{ GeV}/c^2$ . Additional ingredients of the kinematic fit:

- The measured quantities are: the lepton, the four leading jet momenta, and  $X_T$ .

- For each event there are 18 unknowns. These are: energy and  $P_z$  of  $X$  (2), 3-momenta of  $t$  and  $\bar{t}$  plus the top mass (7), 3-momenta of the  $W$  bosons (6), and the 3-momenta of the  $\nu$  (3).

This is then a 5-vertices, 2-constraints fit, 5V-2C in SQUAW's language. Notice that the  $\nu$  momentum is considered an unknown quantity. This is because the  $\cancel{E}_T$  is highly correlated with the jet momentum measurements. The calculated value of  $\cancel{E}_T$  is used as a starting point to help with the convergence of the fit. Lagrange multiplier techniques are used to solve the 20 equations. The final  $\chi^2$  has contributions from all 20 equations.

One of the differences with the MINUIT algorithm is that SQUAW works with the 4-vectors, hence it allows the angles of the lepton and jets to vary within their uncertainties. The momentum magnitude and angles are assumed to be uncorrelated.

The results of the two methods for a given event are very close. In the 76 event data sample the masses obtained with the two methods (using the mass from the lowest  $\chi^2$  solution in each case) differ on the average by 0.1 GeV/ $c^2$ , and in 70% of the events the absolute value of the mass difference is less than 0.5 GeV/ $c^2$ .

## 6.2 Combinatorics

There is always some ambiguity in how to assign the four leading jets to the four relevant partons. If none of the jets is tagged as a  $b$  candidate, by either the SVX or SLT algorithm, then there are 12 different ways of assigning jets to the  $b$  and  $\bar{b}$  partons. Combined with the  $P_z^\nu$  ambiguity, there are then 24 combinations, or configurations, per event. If one jet is tagged as a  $b$  candidate, we require that it is assigned to a  $b$  or  $\bar{b}$  parton, and this reduces the number of allowed combinations to 12. If two jets are  $b$  tagged, there are four combinations. Of the above combinations the solution with the

lowest  $\chi^2$  is chosen, and that solution is required to have  $\chi^2 < 10$ . The latter requirement defines criterion 9 of the Top Mass Candidate Sample described in Section 3.3. We have not found a satisfactory method for improving the top mass resolution by including any solutions with  $\chi^2$  values larger than the lowest one, and therefore we take the lowest  $\chi^2$  solution as the best estimate of the top mass for each event.

### 6.3 Impact of gluon radiation

A substantial fraction of  $t\bar{t}$  events are expected to contain extra jets resulting from gluon radiation. From a HERWIG Monte Carlo plus detector simulation, we find that  $\approx 40\%$  of events have one or more jets which do not correspond to the partons from the  $t\bar{t}$  decay. These extra jets may be produced during the production of the  $t\bar{t}$  pair (initial state radiation) or in the decay stage (final state radiation) [56]. From a theoretical perspective, whether or not the extra jet(s) are to be included in the fit depends on whether the gluon was radiated during production of the  $t\bar{t}$  pair or during its decay. If the radiation comes from the production stage, then it should not be included in the mass fit. If the radiation is produced from a quark in the decay stage, then it should be included as one of the decay products [56].

From an experimental perspective, the radiation results in jets which may or may not have been produced in the  $t\bar{t}$  decay process. On an event-by-event basis, production and decay stage radiation cannot be differentiated from each other or, for that matter, from the partons from the  $t\bar{t}$  decay (unless the jet is  $b$  tagged). Gluon jets which come from decay stage radiation are more correlated with the partons emerging from the hard scatter, and therefore one can consider merging jets which are close in  $\eta-\phi$  space. It is also possible to try all unique permutations of four jets among all the reconstructed jets. However, taking a fifth jet into consideration increases the number of combinations by a

factor of 3, 4, and 5 for the 2, 1, and 0  $b$ -tag cases respectively. This increase in the number of solutions reduces the probability for choosing the correct jet assignment. The mass reconstruction presented here does not implement either of these possibilities. Our approach is to assume the model of initial and final state radiation in the Monte Carlo simulation is correct, and to associate a systematic uncertainty with this assumption.

## 6.4 Results of the kinematic fit on simulated $t\bar{t}$ events

The reconstructed-mass distribution obtained by fitting simulated  $t\bar{t}$  events depends on the intrinsic resolution of the detector, and, more importantly, the ability to correctly associate the daughter partons from a  $t\bar{t}$  decay with the observed jets. Both combinatorics and gluon radiation play a role in degrading the resolution of the top quark mass measurement. In this section, we discuss the performance of the mass fitter by dividing events (which enter into one of the four mass subsamples) into three categories:

1. **Correctly Assigned Events:** Each of the four leading jets are within  $\Delta R < 0.4$  of a parton from the  $t\bar{t}$  decay and are correctly associated with the appropriate quark by the lowest  $\chi^2$  solution satisfying any imposed tagging requirements. The jet-parton match is required to be unique.
2. **Incorrectly Assigned Events:** Each of the four leading jets are within  $\Delta R < 0.4$  of a parton from the  $t\bar{t}$  decay and each jet-parton match is unique, but the configuration with the lowest  $\chi^2$  is not the correct one.
3. **Ill-Defined Events:** The four leading partons from the  $t\bar{t}$  decay cannot be uniquely matched ( $\Delta R < 0.4$ ) to the four leading jets in the event. Such events often have extra jets produced from either initial state or final state radiation.

The fractions of events falling into each of these categories are estimated using a HERWIG  $t\bar{t}$  Monte Carlo plus detector simulation. These fractions depend on the  $b$ -tagging information in the event. For example, having two  $b$ -tagged jets in an event reduces the probability that one (or more) of the leading four jets is a gluon jet. The fractions of events falling into categories 1–3 above, and the width of the reconstructed-mass distribution for each of the four mass subsamples are shown in Table 6.1. The widths are calculated as half the difference between the 16<sup>th</sup> and 84<sup>th</sup> percentiles of the reconstructed-mass distributions. The reconstructed-mass distributions for the four mass subsamples are shown in Fig. 6.1.

Data sample	Event fractions (%)			Width (GeV/ $c^2$ )
	1	2	3	
SVX Double	$49 \pm 2$	$23 \pm 2$	$28 \pm 2$	19.9
SVX Single	$30 \pm 1$	$26 \pm 1$	$44 \pm 1$	24.2
SLT	$26 \pm 2$	$31 \pm 2$	$43 \pm 2$	25.0
No Tags	$23 \pm 1$	$32 \pm 1$	$45 \pm 1$	26.9

Table 6.1: Fractions of  $t\bar{t}$  events falling into categories 1–3 described in the text. The last column shows the width of the distribution of reconstructed masses for each subsample. The width is taken to be half the difference between the 16<sup>th</sup> and 84<sup>th</sup> percentiles of the relevant mass distribution.

As Table 6.1 shows, the fraction of correctly assigned jets increases as the number and purity of  $b$  tags increase. Figure 6.2 shows the reconstructed-mass distributions for events in each of these three categories. When the correct jet-parton assignments are made (category 1), the resolution is  $\approx 13$  GeV/ $c^2$ , while for categories 2 and 3 it is  $\approx 36$  and  $34$  GeV/ $c^2$  respectively. As Fig. 6.2 demonstrates, the mass resolution is dominated by incorrect assignment of jets to partons from the  $t\bar{t}$  decay. For Double SVX tagged events, where nearly half of the events have the four leading jets correctly assigned

to the  $t\bar{t}$  decay products, we obtain the best resolution on the reconstructed mass.

A priori, it is not obvious whether events which have the jets misassigned to the  $t\bar{t}$  daughter partons contain information on the top quark mass. This is quantified by studying the sensitivity of the distribution of reconstructed masses to changes in the input value of the top quark mass. We examine the events in categories 1–3 separately in order to determine if the misassigned events contribute information to the top quark mass measurement. For each category of events, we evaluate the rate of change of the median of the reconstructed-mass distribution as we vary the input value of the top quark mass. Larger changes in the median imply greater sensitivity to the top quark mass. Figure 6.3 shows the median reconstructed-mass as a function of the input top quark mass. Events from all four mass subsamples are included in the distributions. The four distributions correspond to events in (a) category 1, (b) category 2, (c) category 3, and (d) the three categories combined. We find that the events in which the jets are correctly assigned to the partons have the largest slope (0.90), while incorrectly assigned events have a slope of 0.62 and ill-defined events have a slope of 0.48. Correctly assigned events (category 1) do not have a slope of 1.0 because the top-specific corrections (see Section 5.1.3) are derived using a specific input top quark mass of  $170 \text{ GeV}/c^2$ . We conclude that the events with incorrect jet-to-parton assignments do in fact contain information on the top quark mass, since the slope is not zero. However, because of the smaller slope and larger width of the reconstructed-mass distribution, incorrect combinations degrade the resolution of the top quark mass measurement. The slopes for each of the four subsamples in each category are shown in Table 6.2. The slopes vary from a maximum of 0.81 for SVX Double tags to a minimum of 0.62 for SLT tagged events. Since SVX double-tagged events have the largest slope, narrowest

width and lowest background, they generally yield the best precision on the top quark mass measurement (for equal size subsamples).

Data sample	Slopes			
	1	2	3	Combined
SVX Double	$0.89 \pm 0.02$	$0.48 \pm 0.08$	$0.57 \pm 0.05$	$0.81 \pm 0.03$
SVX Single	$0.90 \pm 0.01$	$0.60 \pm 0.04$	$0.52 \pm 0.02$	$0.72 \pm 0.02$
SLT	$0.93 \pm 0.02$	$0.68 \pm 0.05$	$0.38 \pm 0.04$	$0.62 \pm 0.03$
No Tags	$0.90 \pm 0.01$	$0.62 \pm 0.03$	$0.47 \pm 0.03$	$0.68 \pm 0.02$

Table 6.2: Rate of change (“slope”) of the median reconstructed mass with the input value of the top quark mass, for the four mass subsamples. For each subsample, we show the slope for the three categories of events defined in the text, both separately and combined.

### 6.4.1 Mass reconstruction in other $t\bar{t}$ decay channels

Although the fitting procedure assumes that the candidate  $t\bar{t}$  events have decayed through the  $t\bar{t} \rightarrow (e \text{ or } \mu)\nu q\bar{q}'b\bar{b}$  channel, there is a non-negligible contribution from top events decaying through other channels. The additional acceptance from other decay channels comes mostly from events where either an electron or a  $\tau$  from the  $t$  or  $\bar{t}$  decay is misconstrued as a jet or from events with a leptonically decaying  $\tau$ . In either case, two  $b$  jets are still present. The fourth jet can be produced through gluon radiation. Table 6.3 gives the expected contributions of various decay channels to the candidate  $t\bar{t}$  sample and to the subsample with at least one SVX or SLT tag. It shows an 11% contribution from  $\tau$  events and 4% contribution from  $ee$ ,  $e\mu$  and  $\mu\mu$  events.

Figure 6.4 shows the reconstructed-mass distribution for events from these decay channels. The inset shows how the median of the reconstructed-mass distribution changes with the input value of the top quark mass used in the simulation. The relatively low, but non-zero value of the slope indicates

that these events also provide information about the top quark mass. The signal templates, to be discussed in Section 7, include contributions from these channels, hence we do not expect any bias on the fitted top mass from these events.

Channel	Top Mass Candidate Sample	Tagged Events
e+jets	$0.423 \pm 0.008$	$0.424 \pm 0.010$
$\mu$ +jets	$0.426 \pm 0.008$	$0.430 \pm 0.010$
$e - \tau(had)$	$0.017 \pm 0.002$	$0.017 \pm 0.003$
$e - \tau(lep)$	$0.007 \pm 0.001$	$0.007 \pm 0.002$
$ee$	$0.012 \pm 0.002$	$0.011 \pm 0.002$
$e - \mu$	$0.023 \pm 0.002$	$0.024 \pm 0.003$
$\mu - \tau(had)$	$0.017 \pm 0.002$	$0.017 \pm 0.003$
$\mu - \tau(lep)$	$0.005 \pm 0.001$	$0.006 \pm 0.002$
$\mu - \mu$	$0.004 \pm 0.001$	$0.004 \pm 0.001$
$\tau(had) + \tau(lep)$	$0.002 \pm 0.001$	-
$\tau(lep)$ +jets	$0.063 \pm 0.004$	$0.058 \pm 0.005$

Table 6.3: Fractional contribution (according to Monte Carlo simulation) of lepton+jets events to  $t\bar{t}$  events in the Top Mass Candidate Sample and the Tagged subsample. The Tagged subsample includes events with at least one  $b$ -tagged jet. Similar numbers are found for other subsamples (*i.e.* SVX Double, SVX Single and SLT). *lep* and *had* denote leptonic and hadronic decays, respectively, for the  $\tau$  lepton. A dash indicates that no events were found in the category.

## 6.5 Mass reconstruction in non- $t\bar{t}$ events

Non- $t\bar{t}$  events are also present in the data samples. For all the samples considered, the dominant background is expected to be from production of  $W$  bosons in association with extra jets. The background shape is modeled with the VECBOS Monte Carlo simulation. As with  $t\bar{t}$  events, we fit the background events using the  $\chi^2$  defined in Section 6. Since the sample of events does not



contain  $t\bar{t}$ , one does not expect any resonant peaks in the reconstructed-mass spectra. The reconstructed-mass spectrum for VECBOS events which have at least one  $b$ -tagged jet is shown in Fig. 6.5. This distribution is compared to the distributions for  $t\bar{t}$  events with input top quark masses of 140, 175, and 200 GeV/ $c^2$ . It is observed that for a top quark mass of 140 GeV/ $c^2$ , the signal and background peak at nearly the same value of reconstructed mass. However, the  $t\bar{t}$  events are more sharply peaked than background, and therefore there is still shape discrimination between the two. As the top quark mass increases, the reconstructed-mass distribution for  $t\bar{t}$  events is clearly separated from the background. Since we include a background constraint in the top quark mass likelihood fit (see Section 7), differences in shape between signal and background events are not required. However, the shape differences do improve the resolution on the top quark mass measurement.

### 6.5.1 Comparisons of VECBOS with data

The background modeling is checked by comparing the reconstructed  $W+4$  jet mass distributions from some data samples with the appropriate distributions from the VECBOS simulation. The data samples consist of events that fail only one of the top sample criteria. The samples compared are:

- events failing only the lepton isolation criteria;
- events having fewer than three jets with  $E_T > 15$  GeV and  $|\eta| < 2$  (see Section 3.3);
- events with a non-central ( $1.1 < |\eta| < 2.4$ ) primary electron.

Each of these samples fails one and only one of the top sample criteria. Figure 6.6 shows the reconstructed-mass spectrum for candidate  $W+4$  jet events in which the primary electron is not isolated from jet activity in the event. The

requirement that the lepton is non-isolated makes it more likely that the selected data events are from multi-jet or  $b\bar{b}$  production. The data are compared to the distribution from VECBOS events which also failed the lepton isolation criteria. The similarity of the two distributions shows that the non-W/Z component of the background is well modeled by the VECBOS simulation. The fraction of  $t\bar{t}$  events in the data sample is expected to be  $\approx 9\%$ . A Kolmogorov-Smirnov test applied to these two distributions yields a 36% confidence level for agreement. Figure 6.7 shows a similar comparison in which the events are required to have no more than two jets with  $E_T$  greater than 15 GeV. This sample has an estimated  $t\bar{t}$  contribution of about 0.7%. A Kolmogorov-Smirnov test applied to these two distributions yields a 45% confidence level for agreement. Figure 6.8 compares samples of events in which the primary electron was reconstructed in the PEM ( $1.1 < |\eta| < 2.4$ ). We expect little or no dependence of the reconstructed mass on the  $\eta$  value of the primary electron, as evidenced by the similarity between this VECBOS distribution and the one in Fig. 6.5. This sample is estimated to have a  $t\bar{t}$  fraction of 0.2%. A Kolmogorov-Smirnov test applied to these two distributions yields a 33% confidence level for agreement.

We expect the events in these three data samples to be predominantly from the same sources as described in Section 4.3, but in different proportions. In all three cases the VECBOS simulation agrees with the reconstructed-mass distribution in the data. Therefore we assume that the VECBOS simulation models satisfactorily the reconstructed-mass distribution of the background events in the mass subsamples.

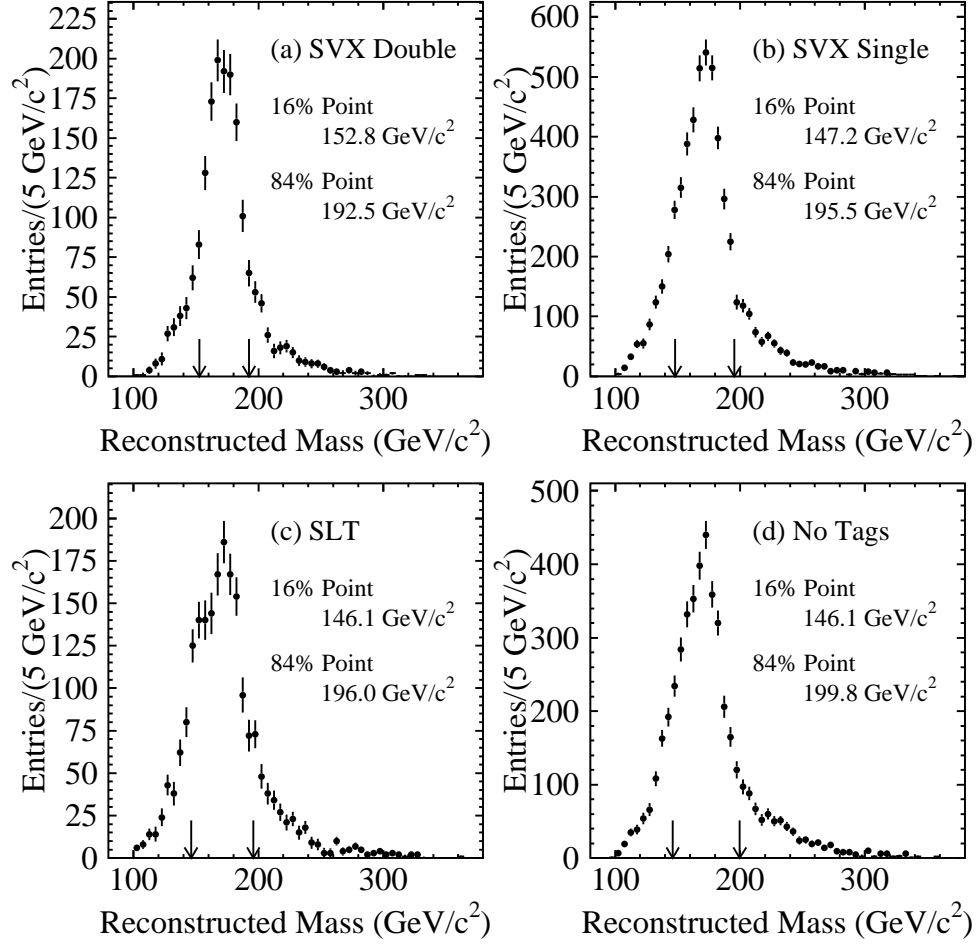


Figure 6.1: Reconstructed-mass distributions for HERWIG  $t\bar{t}$  events ( $M_{top} = 175 \text{ GeV}/c^2$ ) for the mass subsamples: (a) SVX Double, (b) SVX Single, (c) SLT (no SVX), and (d) No Tags. The 16<sup>th</sup> and 84<sup>th</sup> percentiles for each distribution are indicated by the arrows on the figures along with their values.

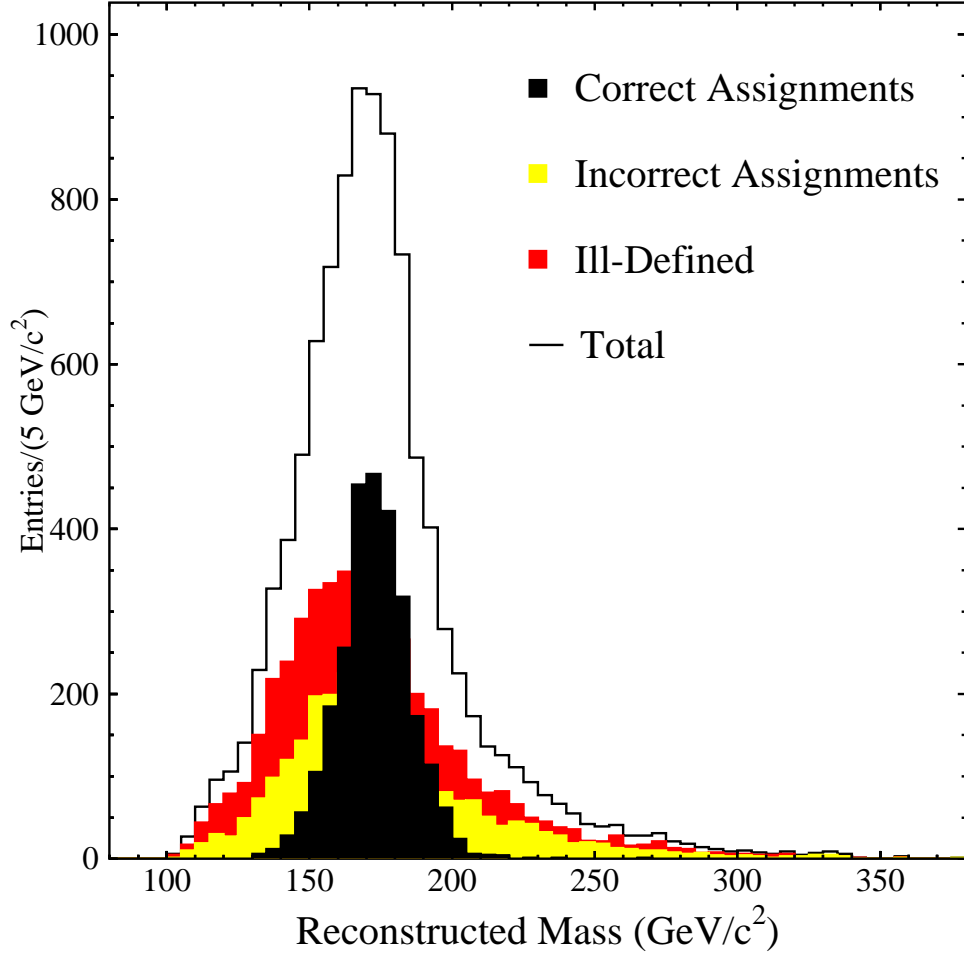


Figure 6.2: Reconstructed mass for  $M_{top} = 175 \text{ GeV}/c^2$   $t\bar{t}$  events which enter into any of the four subsamples. The black filled histogram shows the distribution for those events for which the selected jet-parton configuration was also the correct one (category 1). The lightly shaded histogram shows the distributions for which a correct assignment could be defined, but was not selected (category 2). The darker shaded histogram shows the distribution for events where a correct assignment was ill-defined (category 3). The solid line shows the three distributions combined.

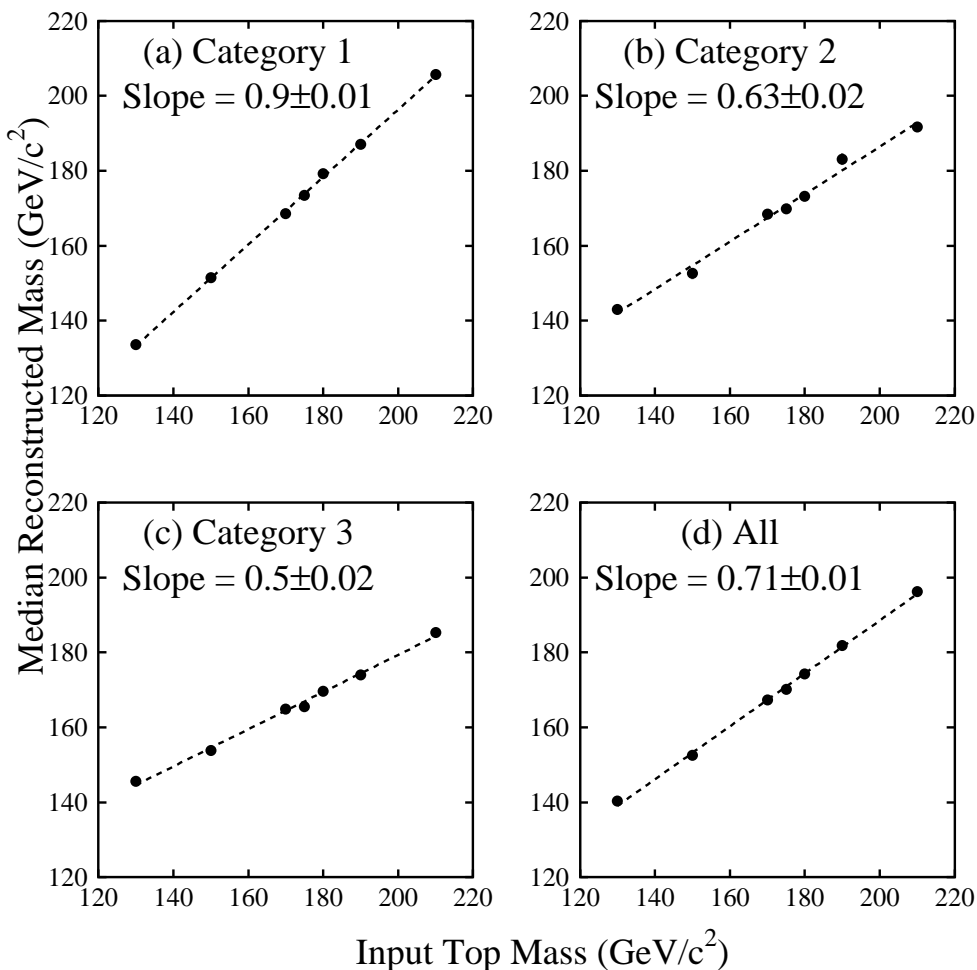


Figure 6.3: Median of the reconstructed-mass distribution as a function of the input top quark mass used in the simulation. The medians are evaluated from mass distributions which include events from all four mass subsamples. The figure demonstrates the relative sensitivity of the reconstructed-mass distribution to the input top quark mass. We show the distributions for events in (a) category 1, (b) category 2, (c) category 3, and (d) the three categories combined. The slopes indicated were evaluated using a linear fit (dashed line) to the data points.

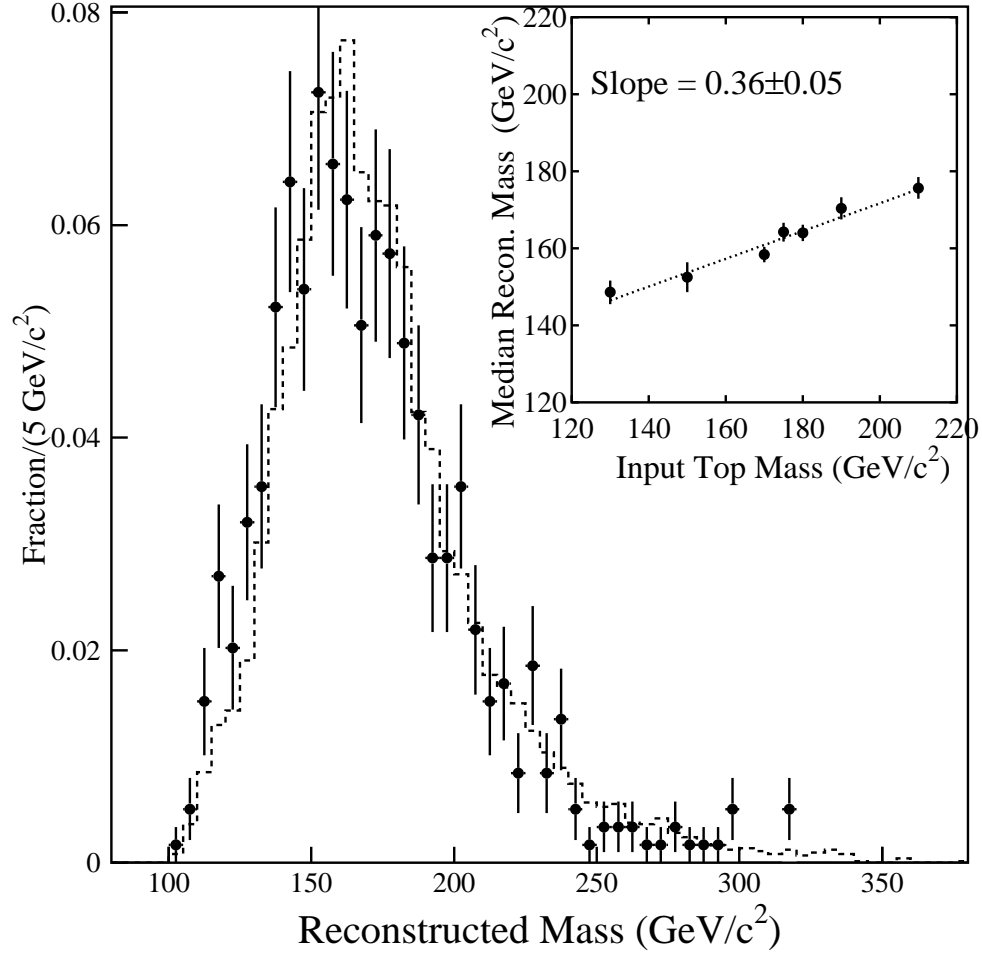


Figure 6.4: Reconstructed masses for  $t\bar{t}$  events ( $M_{top} = 175 \text{ GeV}/c^2$ ) which decay into decay channels other than  $e$ +jets or  $\mu$ +jets, but fit the hypothesized  $t\bar{t} \rightarrow (e \text{ or } \mu)\nu q\bar{q}'b\bar{b}$  decay chain (points). Most of these events are due to  $W$  decays into  $\tau$  leptons (see Table 6.3). Events from all four mass subsamples are included. For comparison, the dashed distribution corresponds to events decaying through the  $t\bar{t} \rightarrow (e \text{ or } \mu)\nu q\bar{q}'b\bar{b}$  channel, but the lowest  $\chi^2$  solution is incorrect (i.e., events in categories 2 and 3). The inset shows how the median of the reconstructed-mass distribution changes with the input value of the top quark mass used in the simulation.

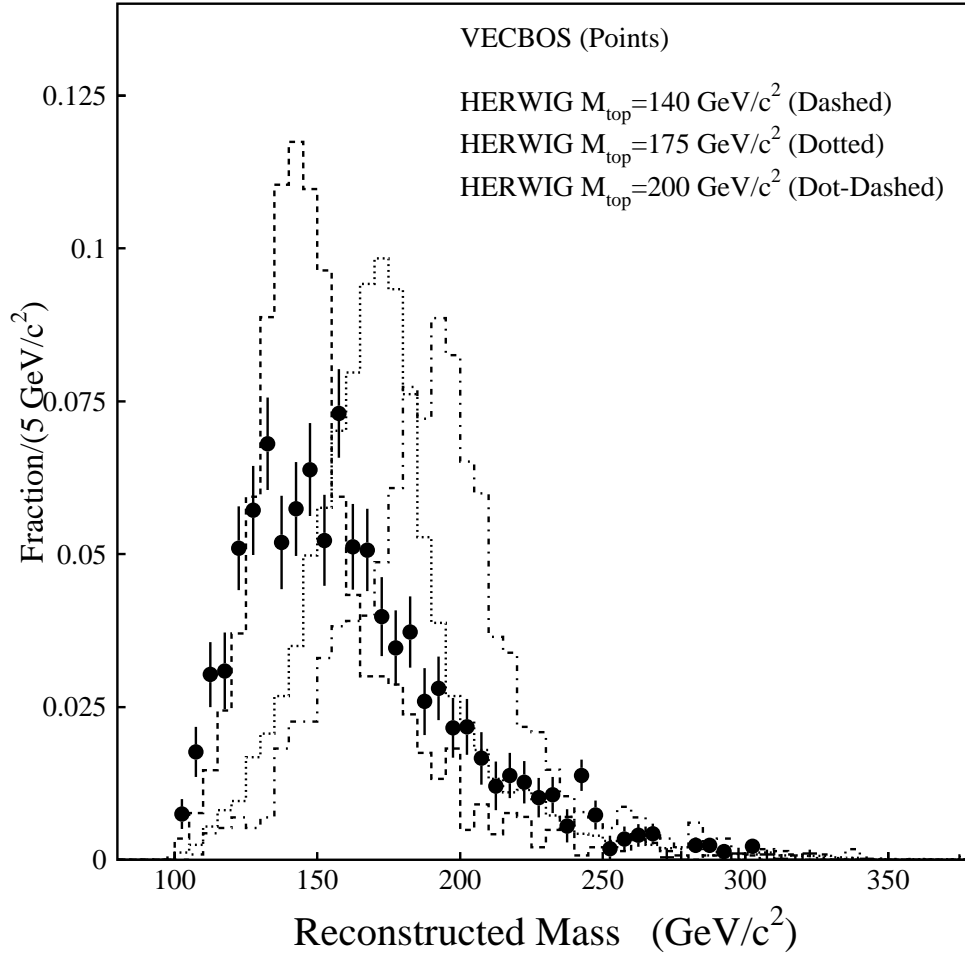


Figure 6.5: Reconstructed-mass distribution for background events from the VECBOS Monte Carlo simulation (points). Also shown are the reconstructed-mass distributions from the HERWIG Monte Carlo simulation using input top quark masses of 140, 175, and 200 GeV/c<sup>2</sup>. In all cases, events are required to have at least one SVX or SLT tagged jet. Each distribution is normalized to have unit area.

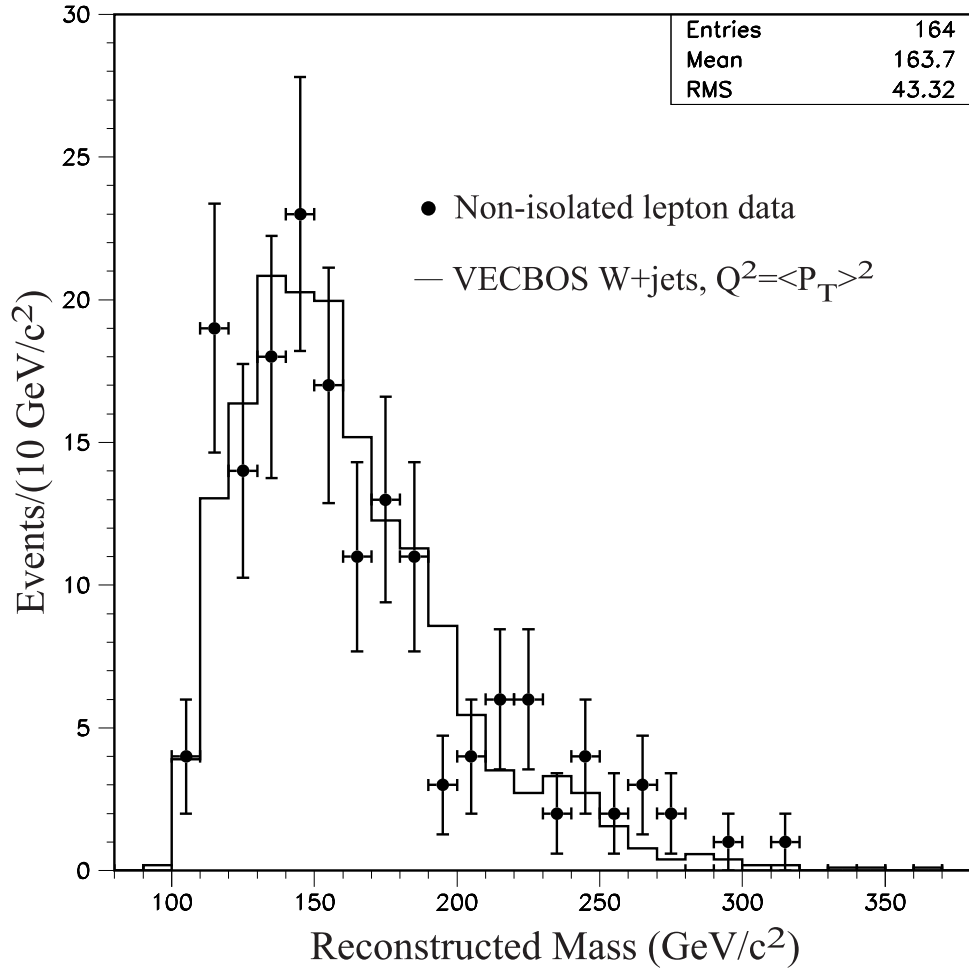


Figure 6.6: Reconstructed-mass distribution for events containing at least four jets,  $\cancel{E}_T$ , and a non-isolated lepton. The expected fraction of  $t\bar{t}$  in this sample is  $\approx 9\%$ . The points are data and the histogram is the VECBOS distribution.



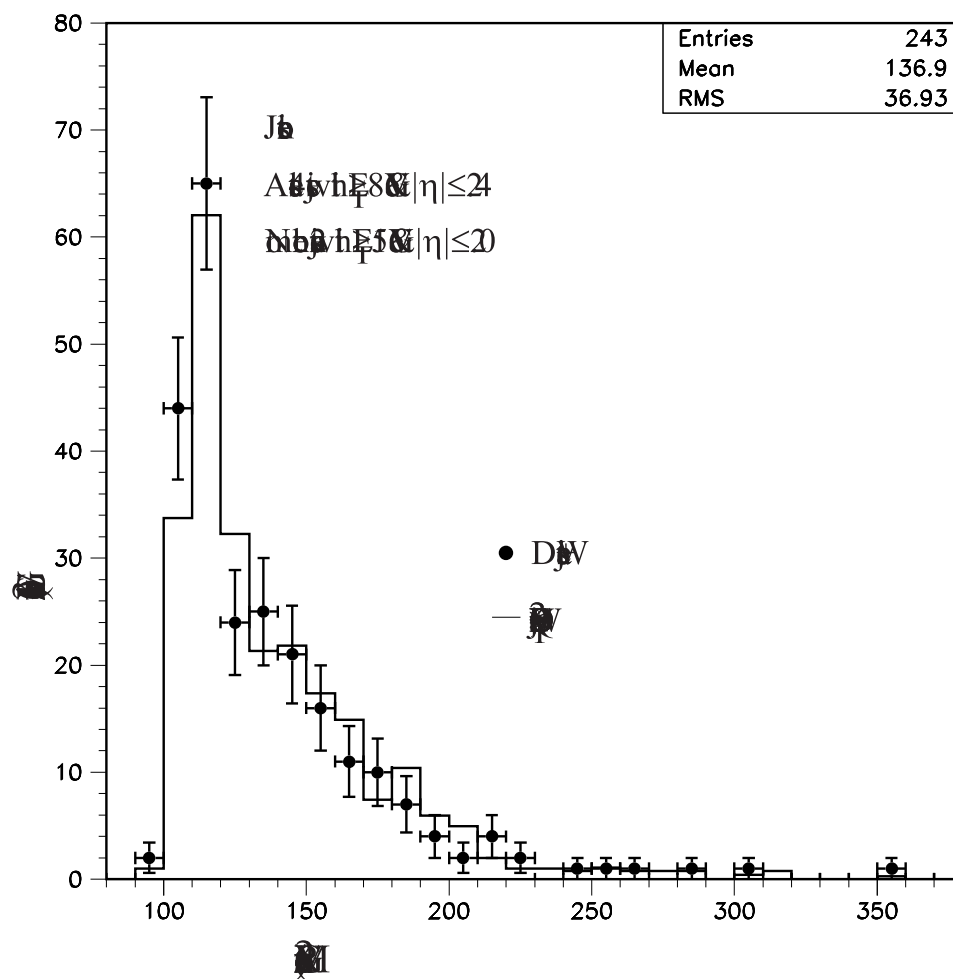


Figure 6.7: Reconstructed-mass distributions for events with an isolated lepton,  $E_T$ , and no more than two jets with  $E_T > 15$  GeV. The expected fraction of  $t\bar{t}$  in this sample is  $\approx 0.7\%$ . The points are data and the histogram is the distribution from VECBOS.

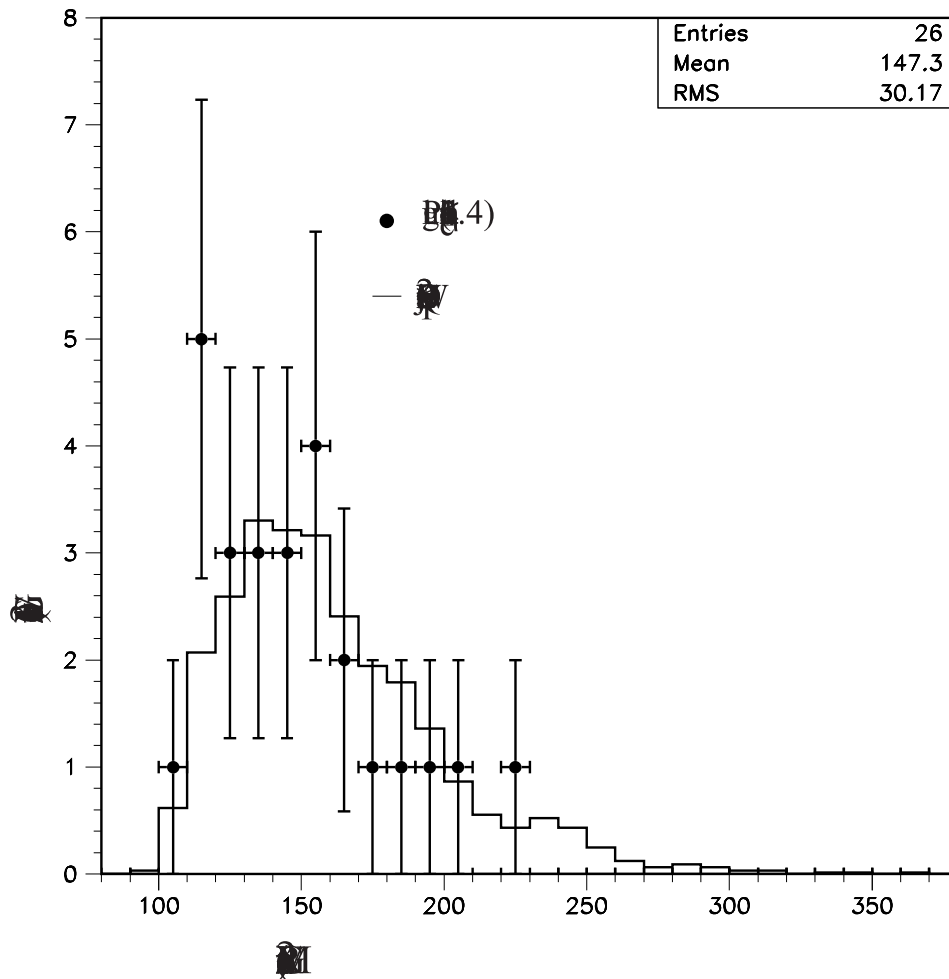


Figure 6.8: Reconstructed-mass distribution for events containing at least four jets,  $\cancel{E}_T$ , and a non-central electron (reconstructed in the region  $1.1 < |\eta| < 2.4$ ). The expected fraction of  $t\bar{t}$  in this sample is  $\approx 0.2\%$ . The points are data and the histogram is the VECBOS distribution.

# Section 7

## DESCRIPTION OF THE LIKELIHOOD PROCEDURE

A likelihood procedure is used to extract a measurement of the top quark mass from the reconstructed-mass distributions of the data samples and the  $t\bar{t}$  signal and background models, along with the constraint on the background fractions. This section describes the likelihood and discusses its validation with the help of simulated experiments.

### 7.1 Parametrization of the reconstructed-mass distributions

We use the HERWIG Monte Carlo plus detector simulation to model the shape of the reconstructed-mass distribution in  $t\bar{t}$  events. Event samples are generated at several different values of the top quark mass ranging from 120 to 220 GeV/ $c^2$ . The VECBOS Monte Carlo program is used to model the shape of the background distribution. The  $t\bar{t}$  and background samples are processed using the CDF simulation, and the same analysis is applied to them

as to the data sample. Histograms of reconstructed masses from these samples are referred to as templates.

Since we generated templates for only a finite number of input top quark masses, extraction of a measured top quark mass from the data will require an interpolation. This can be achieved in one of two ways. The first consists of fitting the data separately at each input top quark mass value to a combination of signal (at the given mass) and background. The maximum likelihood is then interpolated from the resulting likelihood values. The second method requires that the templates themselves be interpolated as a function of input top quark mass. The signal templates then become a function of both the input top quark mass and the reconstructed mass. The background templates are only functions of the reconstructed mass. The likelihood can then be defined as a smooth function of both input mass and reconstructed mass, and no further interpolation is needed. Previous publications [1, 2], with lower statistics, have used the first method of interpolation. However, the second method employs a single interpolation process and uses optimally the finite Monte Carlo statistics in the templates. We have adopted the latter method for this analysis.

### 7.1.1 Signal parametrization

A single function,  $f_s$ , is used to model the distribution of reconstructed top masses for  $t\bar{t}$  events for any given value of the input top quark mass between 120 and 220 GeV/ $c^2$ :

$$f_s(M_t, P_k) = N [P_6 f_1(M_t, P_{1,2,3}) + (1 - P_6) f_2(M_t, P_{4,5})], \quad (7.1)$$

where:

$$f_1(M_t, P_{1,2,3}) = \frac{P_3^{1+P_2}}{\Gamma(1+P_2)} (M_t - P_1)^{P_2} e^{-P_3(M_t - P_1)}, \quad (7.2)$$

$$f_2(M_t, P_{4,5}) = \frac{1}{\sqrt{2\pi}P_5} e^{-\frac{1}{2}\left(\frac{M_t - P_4}{P_5}\right)^2}, \quad (7.3)$$

$$P_i = \alpha_i + \alpha_{i+6} M_{top}. \quad (7.4)$$

For each mass subsample, six pairs of parameters  $(\alpha_i, \alpha_{i+6})$  are needed to describe how the distribution of reconstructed mass ( $M_t$ ) evolves with the input top quark mass ( $M_{top}$ ). For example,  $\alpha_4$  and  $\alpha_{10}$  ( $\alpha_5$  and  $\alpha_{11}$ ) describe how the mean (width) of the Gaussian portion of the reconstructed-mass distribution changes with  $M_{top}$ . The parameter values and their covariance matrix are obtained by a chisquare fit to the templates [57]. Six of the 18 templates for the SVX Single sample are shown in Fig 7.1 together with the predictions obtained from the fit parameter values. Figs 7.2–7.4 show the same six templates for the SVX Double, SLT, and No Tag subsamples respectively. The fit chisquares per degree of freedom (*dof*) are: 1.17 for 555 *dof*, 1.07 for 335 *dof*, 0.96 for 454 *dof*, and 1.36 for 589 *dof*, for these four subsamples, respectively.

### 7.1.2 Background parametrization

The fitting of the distribution of reconstructed masses from VECBOS is performed in a similar fashion to the signal templates, but with fewer parameters and no dependence on  $M_{top}$ . For the tagged subsamples, the background distribution shape can be described by  $f_1$ , whereas the No Tag subsample requires the additional freedom of  $f_2$  to adequately describe its shape. Figure 7.5 shows the parametrizations of the background distributions for the SVX tagged, SLT (no SVX) tagged, and No Tag events. Because of limited statistics and low probability for obtaining two SVX tagged jets in the VECBOS Monte Carlo simulation, we assume the same background shape for SVX Double and SVX Single tag events. The mass measurement is insensitive to this assumption because the expected background fraction for double tag events is only 4%. In Section 6.5.1 we compared distributions from top-depleted data samples with analogous VECBOS distributions to show that the

VECBOS Monte Carlo simulation models the shape of the  $t\bar{t}$  backgrounds quite well.

## 7.2 Definition of the mass likelihood

The value of  $M_{top}$  for each mass subsample is obtained from a maximum likelihood procedure applied to the observed mass distribution. The procedure allows the template fit parameters and the background fraction  $x_b$  to vary about their central values within their respective uncertainties. The only parameter which is entirely unconstrained in the mass likelihood fit is  $M_{top}$ . The reconstructed masses for the events in each of the four mass subsamples are tabulated in Appendix A. Since the subsamples are statistically independent, the probability of observing these four sets of masses can be expressed as a product of four individual likelihood functions, one for each subsample. These four likelihoods have the same form:

$$\mathcal{L} = \mathcal{L}_{shape} \times \mathcal{L}_{background} \times \mathcal{L}_{param}, \quad (7.5)$$

where:

$$\mathcal{L}_{shape} = \prod_{i=1}^{N_{events}} \left[ (1 - x_b) f_s(M_i, M_{top}, \vec{\alpha}) + x_b f_b(M_i, \vec{\beta}) \right], \quad (7.6)$$

$$\mathcal{L}_{background} = P(x_b), \quad (7.7)$$

$$\mathcal{L}_{param} = \exp \left\{ -\frac{1}{2} \left[ (\vec{\alpha} - \vec{\alpha}_0)^T U^{-1} (\vec{\alpha} - \vec{\alpha}_0) + (\vec{\beta} - \vec{\beta}_0)^T V^{-1} (\vec{\beta} - \vec{\beta}_0) \right] \right\}. \quad (7.8)$$

The likelihood  $\mathcal{L}_{shape}$  is the joint probability density for a sample of  $N_{events}$  reconstructed masses  $M_i$  to come from a parent distribution with background fraction  $x_b$  and signal fraction  $(1 - x_b)$ . The background likelihood  $\mathcal{L}_{background}$ , discussed in Section 4.3.3, constrains the fraction of background events to the expected value within its uncertainties (see Fig. 4.1). The expected background fraction and number of background events are related via  $N_b = x_b \times$

$N_{obs}$ , where  $N_{obs}$  is the number of observed events for that subsample. The vectors  $\vec{\alpha}$  and  $\vec{\beta}$  determine the shapes of the signal ( $f_s$ ) and background ( $f_b$ ) distributions. They are constrained by  $\mathcal{L}_{param}$  to agree with the nominal values,  $\vec{\alpha}_0$  and  $\vec{\beta}_0$ , via their covariance matrices  $U$  and  $V$  respectively. The inclusion of  $\mathcal{L}_{param}$  in the likelihood definition is due to the finite statistics of the Monte Carlo samples used to determine  $f_s$  and  $f_b$ . Furthermore, by parametrizing the signal probability  $f_s$  as a continuous function of  $M_{top}$ , the likelihood is inherently a continuous function of  $M_{top}$  as well.

To extract the top quark mass for each subsample, we minimize  $-\log \mathcal{L}$  with respect to  $M_{top}$ ,  $x_b$ ,  $\vec{\alpha}$  and  $\vec{\beta}$ . The statistical uncertainty on  $M_{top}$  is taken as the change in  $M_{top}$  which results in a 0.5 unit increase in  $-\log \mathcal{L}$  along the line on which  $-\log \mathcal{L}$  is minimized with respect to variations in all the other fit parameters. The statistical uncertainty has contributions not only from the finite statistics in the data sample, but also from the uncertainty in the expected background and the finite statistics in the mass templates. However, the latter two contributions account for less than 1% of the total statistical uncertainty. The top quark mass and its statistical uncertainty for the four subsamples combined are extracted in the same way as above from the product of the four subsample likelihoods.

### 7.3 Tests of the likelihood procedure on simulated experiments

The performance of the likelihood scheme was tested using simulated events from Monte Carlo programs. We performed a large number of simulated experiments, each consisting of four subsamples with the same numbers of events ( $N_{obs}^i, i = 1, \dots, 4$ ) as observed in the four data subsamples. Each experiment subsample contained  $N_b^i$  background events and  $N_s^i = (N_{obs}^i - N_b^i)$   $t\bar{t}$  events, where  $N_b^i$  is a binomial fluctuation of the expected background.

The  $\sum_i N_s^i$  and  $\sum_i N_b^i$  distinct mass values for each simulated experiment were chosen at random from the discrete templates for signal and background events (Figs 7.1–7.5). The four sets of masses were fit using the same likelihood procedure that was used to fit the data sample. Each simulated experiment yielded a fitted top quark mass, a statistical uncertainty and a maximum likelihood value. The self-consistency of the likelihood procedure was tested by comparing these returned values with expectations.

Figure 7.6 shows the distribution of returned masses from the likelihood fit for input top quark masses of 150, 175, and 200 GeV/ $c^2$ . The curves are fits to Gaussians, and have central values of 149.8, 174.8, and 200.2 GeV/ $c^2$ , and  $\sigma$  of 5.8, 6.8, and 7.6 GeV/ $c^2$ . In each case the mean of the distribution is consistent with the input value, which demonstrates that the procedure introduces little or no bias into the top quark mass measurement. The  $\sigma$  of the distributions reflects the expected statistical uncertainty on the top quark mass measurement for experiments which have the same expected background and  $b$ -tag composition as our Run 1 data sample. Based on the fitted  $\sigma$ 's one expects to achieve a statistical uncertainty on  $M_{top}$  of  $\approx 4\%$ .

The statistical uncertainty returned by the likelihood procedure should reflect the deviation of the returned top quark mass from the input value. The pull, defined by

$$\text{Pull} = \frac{M_{exp} - M_{input}}{\sigma_M^{stat}}, \quad (7.9)$$

is used to check the consistency between the measured deviation on the top quark mass and the estimated statistical uncertainty. In the above expression,  $M_{exp}$  is the fitted top mass value returned by the likelihood,  $M_{input}$  is the input value used to generate the (simulated) experiment, and  $\sigma_M^{stat}$  is the statistical uncertainty on  $M_{exp}$  returned by the fitter. Figure 7.7 shows the pull distribution for the simulated experiments generated for  $M_{top} = 175$  GeV/ $c^2$ . The width is close to unity, which indicates that the statistical uncertainty returned by the fitter accurately reflects the deviation of the fitted value from



the input value. Alternately, in Figure 7.8, we take slices in  $\sigma_M^{stat}$ , and evaluate the width of the corresponding  $(M_{exp} - M_{input})$  distribution. The points have a slope of  $0.92 \pm 0.09$ , which supports using the statistical uncertainty returned by the fitter as a measure of the statistical uncertainty for a given experiment.

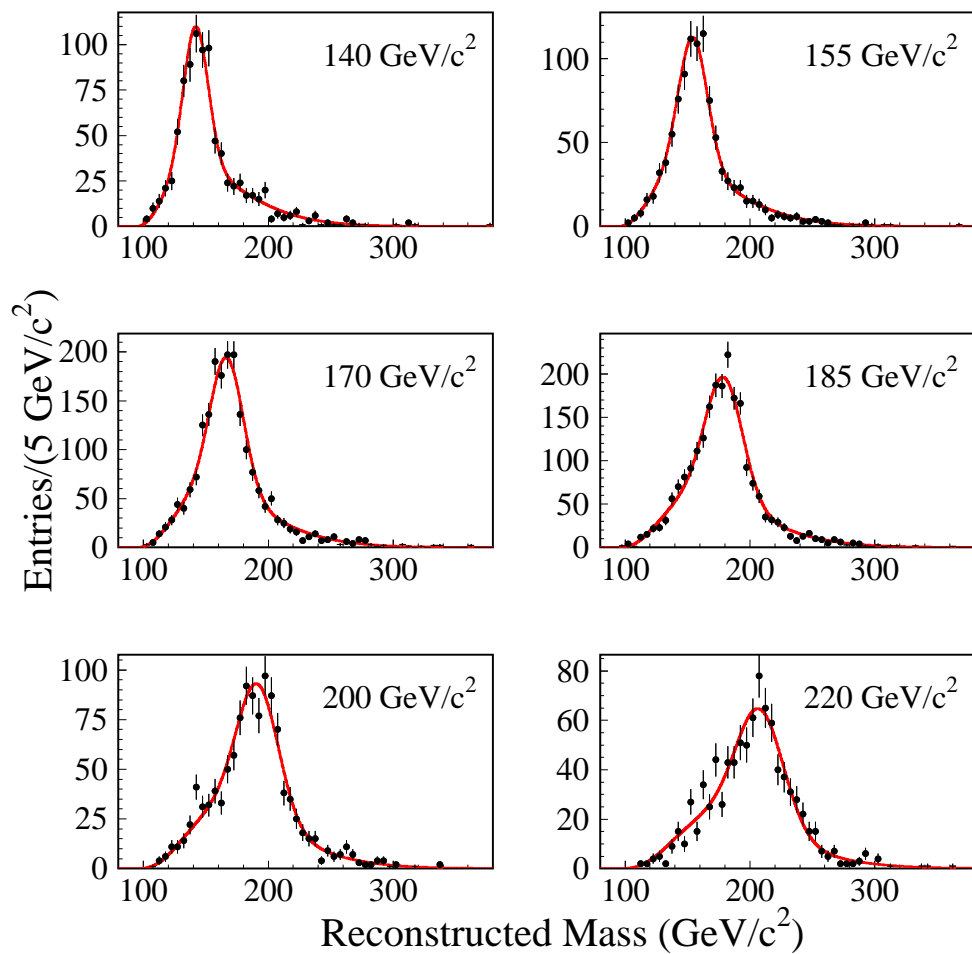


Figure 7.1: Reconstructed-mass distributions from simulated  $t\bar{t}$  events for several input values for the top quark mass used in the simulation. The overlaid curves are predictions from the parametrization of templates at 18 different top mass values. The distributions shown are for the subsample corresponding to events with exactly one SVX-tagged jet.

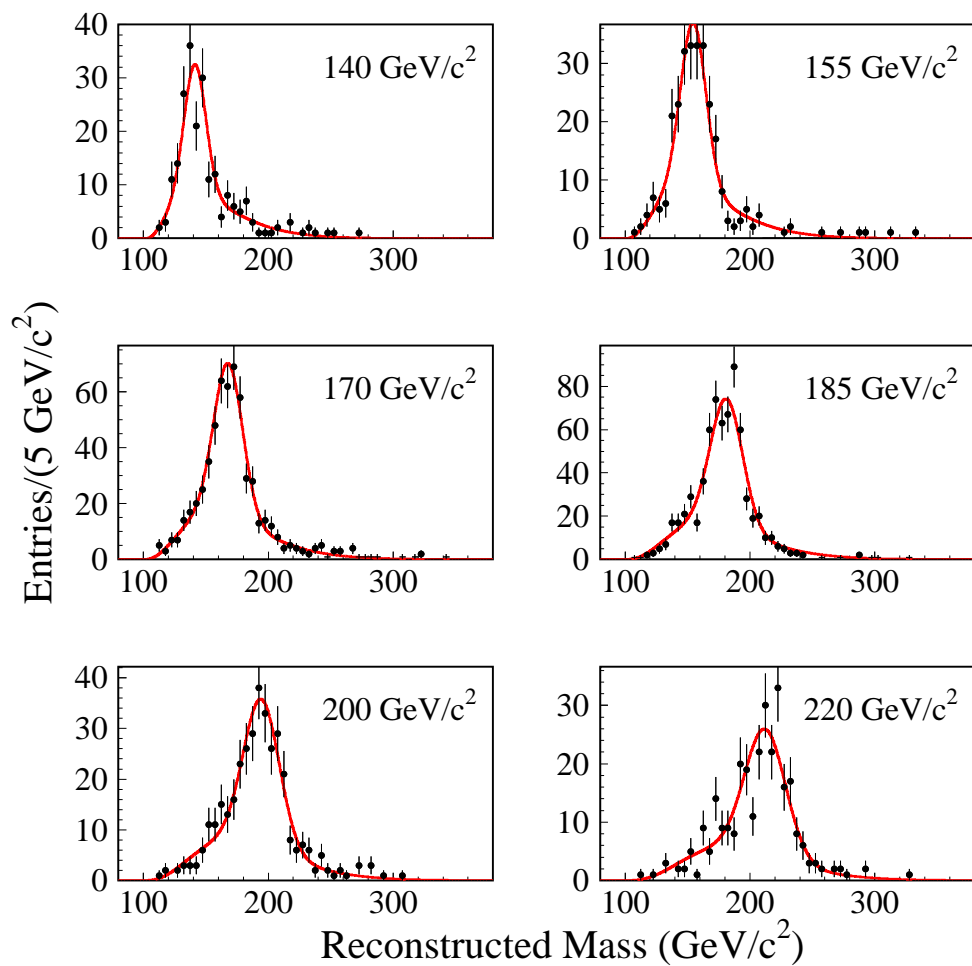


Figure 7.2: Reconstructed-mass distributions from simulated  $t\bar{t}$  events for several input values for the top quark mass used in the simulation. The overlaid curves are predictions from the parametrization of templates at 18 different top mass values. The distributions shown are for the subsample corresponding to events with exactly two SVX-tagged jets.

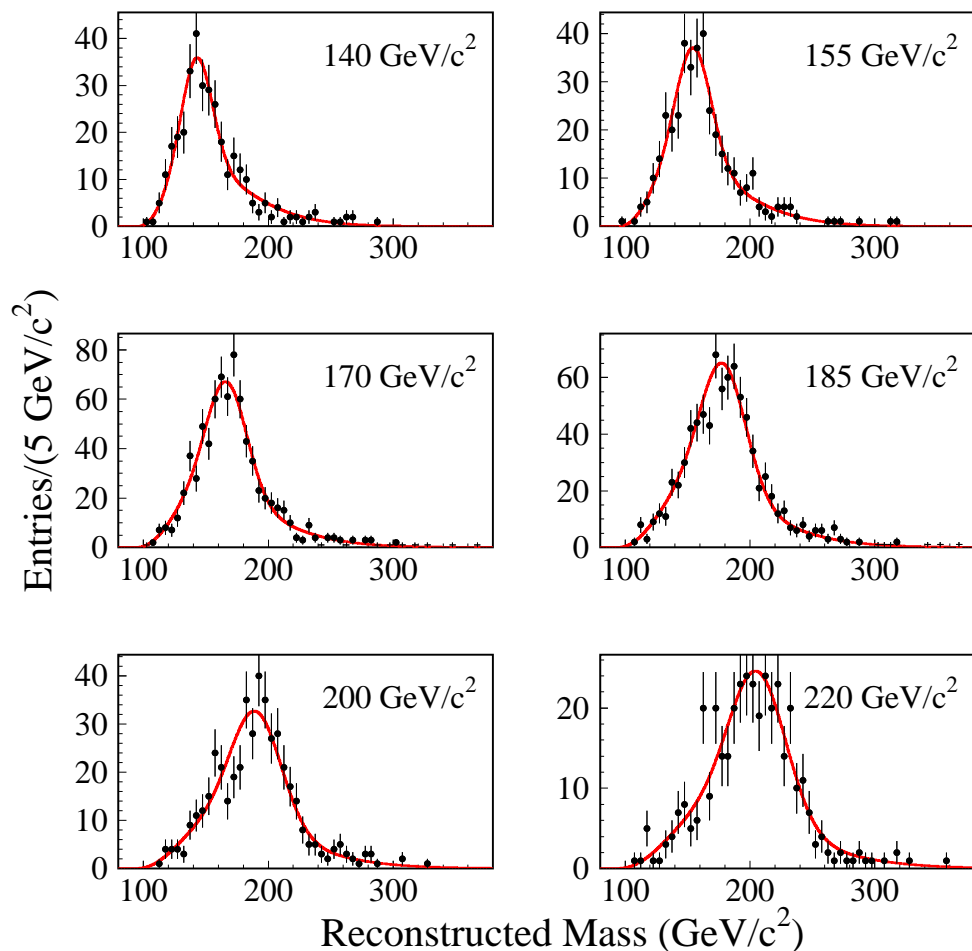


Figure 7.3: Reconstructed-mass distributions from simulated  $t\bar{t}$  events for several input values for the top quark mass used in the simulation. The overlaid curves are predictions from the parametrization of templates at 18 different top mass values. The distributions shown are for the subsample corresponding to events with one or more SLT-tagged jets and no SVX-tagged jets.

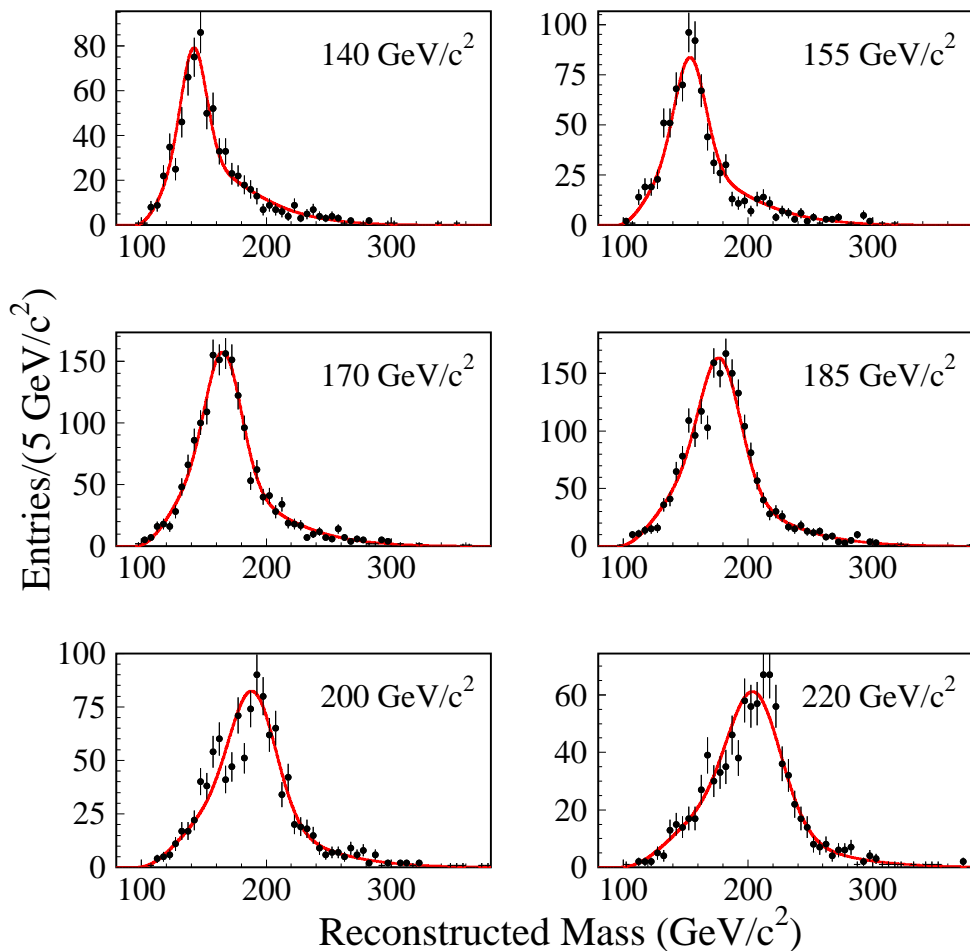


Figure 7.4: Reconstructed-mass distributions from simulated  $t\bar{t}$  events for several input values for the top quark mass used in the simulation. The overlaid curves are predictions from the parametrization of templates at 18 different top mass values. The distributions shown are for the subsample corresponding to events with no SVX-tagged or SLT-tagged jets, and the fourth jet having  $E_T > 15$  GeV and  $|\eta| < 2$ .

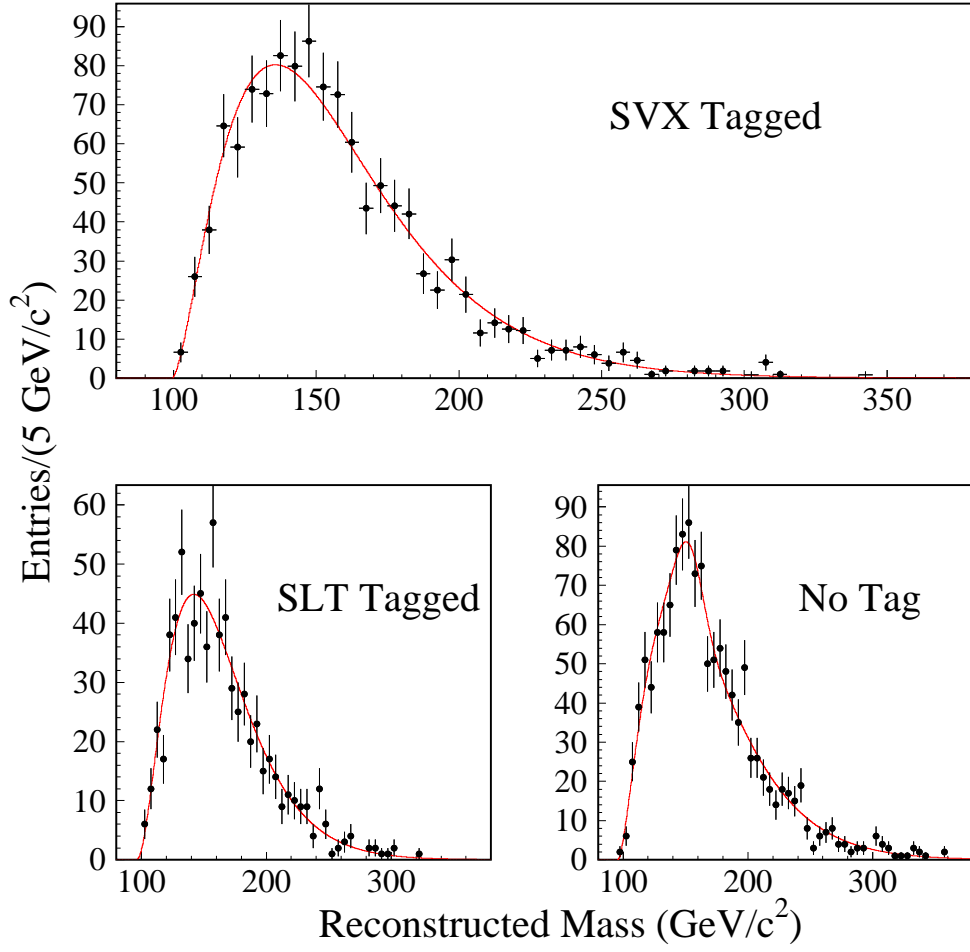


Figure 7.5: Reconstructed-mass distribution for  $W$ +jets events generated with the VECBOS Monte Carlo simulation. The smooth curves are the parametrizations of the reconstructed-mass distributions. The distributions are for SVX tagged, SLT tagged, and No Tag events used in the mass analysis.

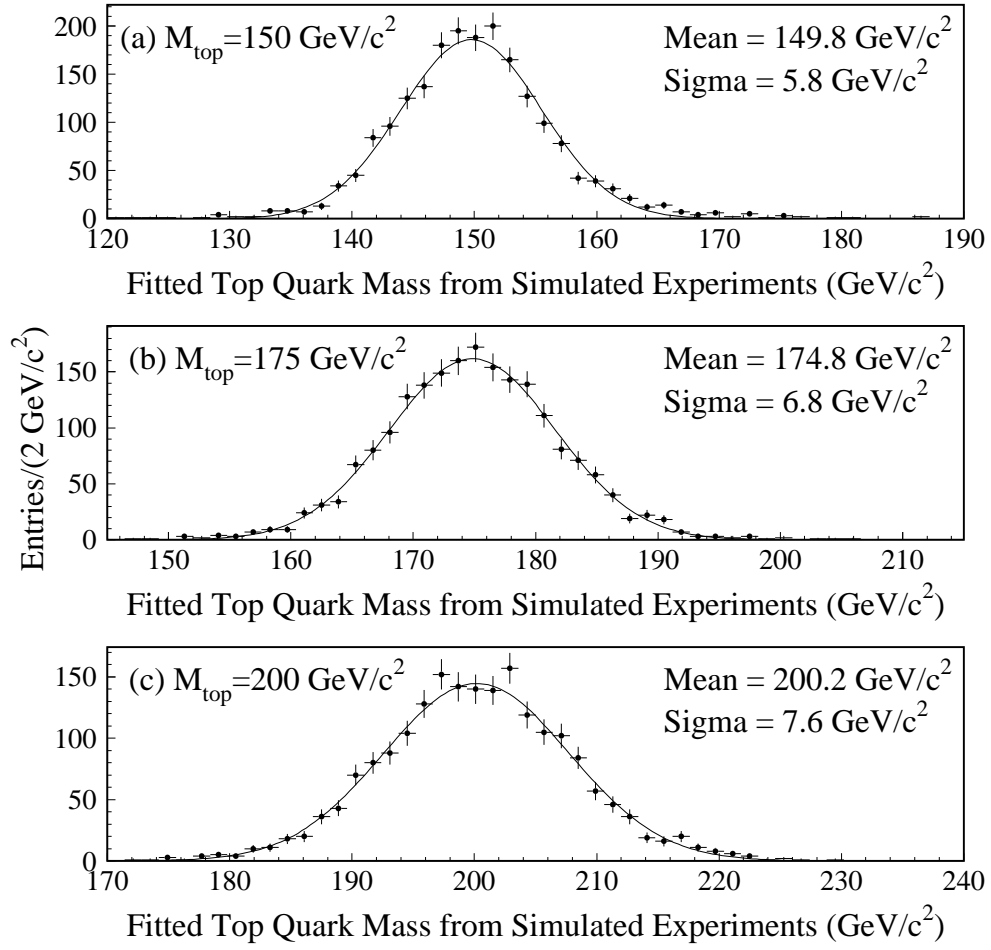


Figure 7.6: The value of the top quark mass returned by the fitter for input top quark masses of 150, 175, and 200  $\text{GeV}/c^2$ . Each simulated experiment contains an admixture of signal and background events as described in the text.

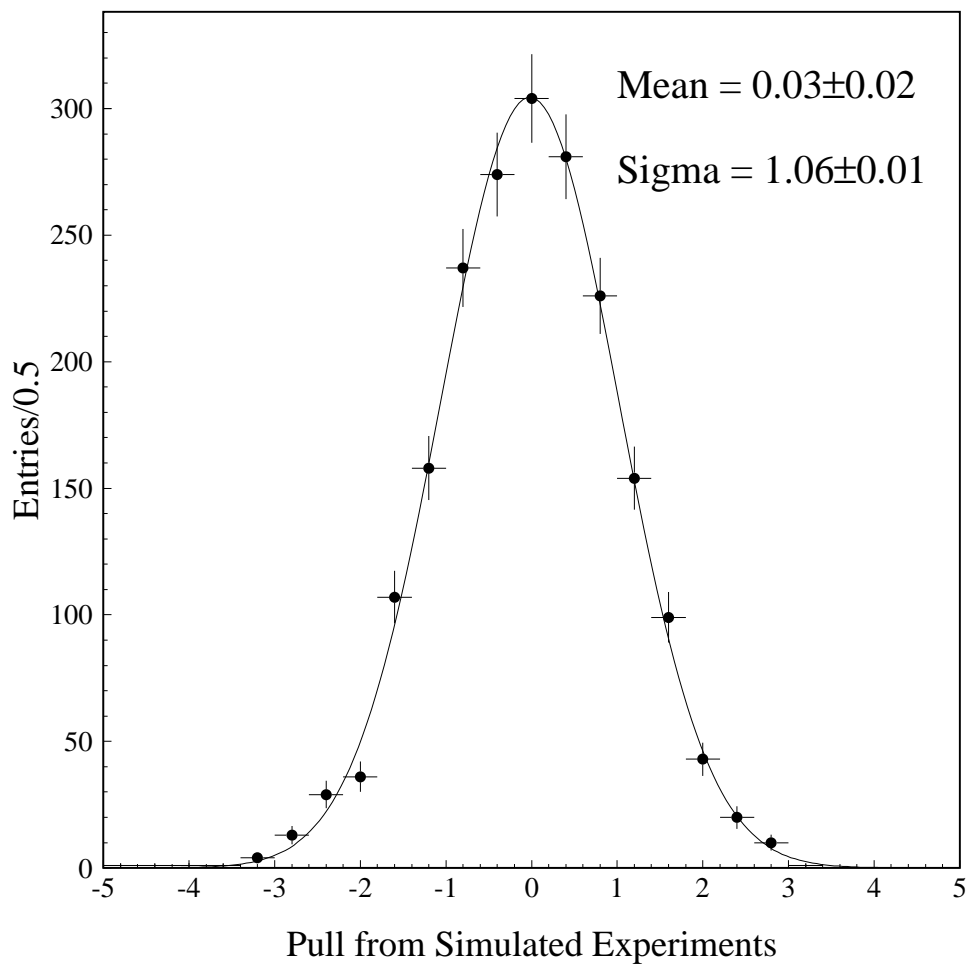


Figure 7.7: The distribution of pulls between the returned value of the top quark mass and the input value of  $175 \text{ GeV}/c^2$ . Each simulated experiment contains an admixture of signal and background events as described in the text.



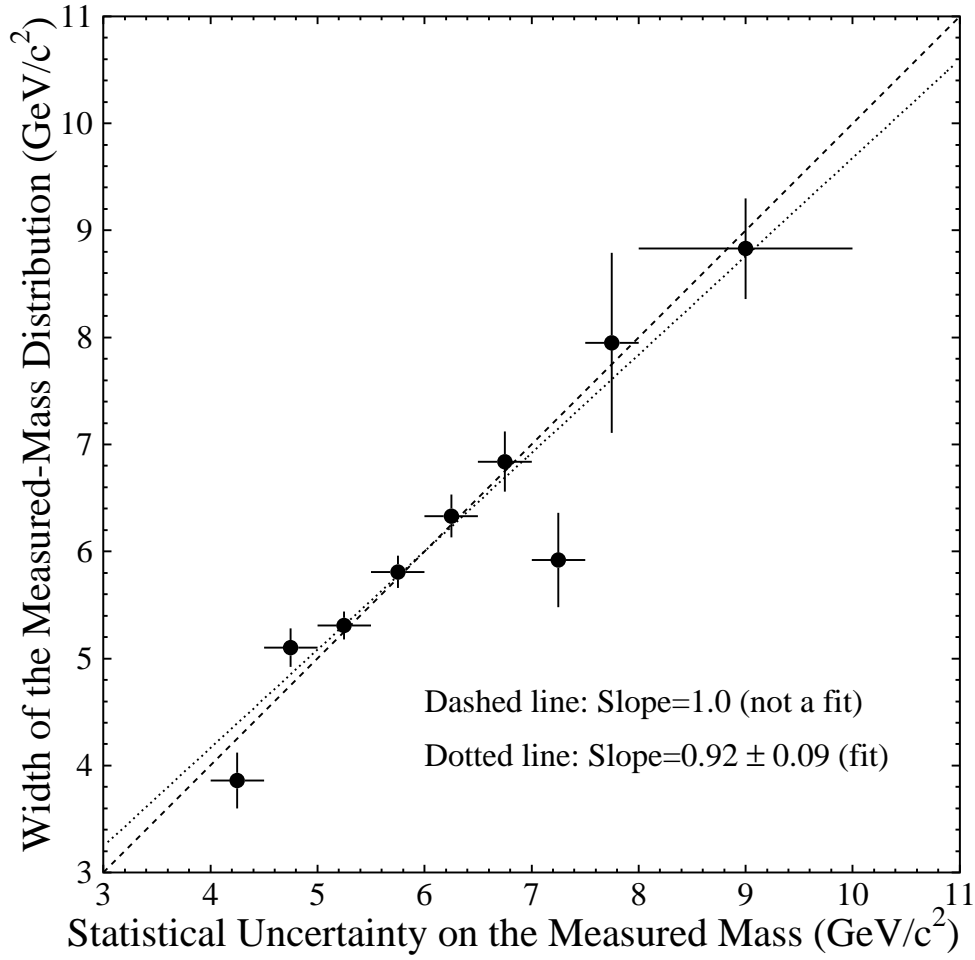


Figure 7.8: The Gaussian width of the mass distribution as a function of the statistical uncertainty returned by the likelihood. Each simulated experiment contains an admixture of signal and background events as described in the text. The dashed line, which has a slope of 1.0, is not a fit. The dotted line is a fit to the points, and has a slope of  $0.92 \pm 0.09$ .

# Section 8

## RESULTS

Having tested the mass likelihood procedure on simulated experiments, we now apply it to the data sample. Two separate fits are performed. The first is the standard mass likelihood fit defined in Section 7.2. The second is the mass likelihood fit with the background fraction constraint removed. In this case, the background fraction is determined only from the shapes of the reconstructed-mass distributions for signal and background. After presenting these results, we check the consistency of the data with Monte Carlo expectation for  $t\bar{t}$  plus background events in the expected proportion.

### 8.1 Fits to data

The mass likelihood procedure is applied to the events in the four mass subsamples. The measured values for the top quark mass for each subsample and the combined results are presented in Table 8.1. As discussed in Section 7.2, the statistical uncertainties contain contributions from both the statistics in the data, the uncertainties in the expected background, and the uncertainties in the template fit parameters. The latter two contribute less than 1% to the total statistical uncertainty. Table 8.1 also shows the fitted

background fractions, which are constrained to the expected values via the background likelihoods in Fig. 4.1. The mass fits for the four mass subsamples are statistically consistent with one another and are shown in Figure 8.1. For each subsample, the background shape has been normalized to the fitted number of background events via  $N_b^i = x_b^{fit} \times N_{obs}^i$ , and the signal plus background has been normalized to the number of data events ( $N_{obs}^i$ ). The combined fit to all four subsamples is shown in Figure 8.2.

To investigate the impact of the background constraining term on the fitted top quark mass, we also performed mass likelihood fits with the constraint on the fraction of background removed. In this case, the shape of the mass distribution determines the background fraction. The results of the mass fits are presented in Table 8.2. Several observations can be made from a comparison of these unconstrained mass fits with the constrained ones in Table 8.1. First, the tagged subsamples fit to zero background, although with large uncertainties, while the No Tag subsample yields a similar background content whether the background is free to float or not. Secondly, the masses show little sensitivity to removal of the background constraint. In general, one would expect the removal of the constraint to result in an increased statistical uncertainty since information is being removed from the likelihood fit. For all subsamples however, the uncertainty in the mass decreases when the background constraint is removed. This is because the fitted number of signal events becomes larger.

Since the background rates in the four mass subsamples are correlated, it is not correct to allow their background fractions to float relative to one another. On the other hand, it is reasonable to investigate whether the background constraint is affecting the top quark mass measurement. The results in Tables 8.1 and 8.2 indicate very little sensitivity to the background constraint.

Data sample	Number of events	$x_b^{fit}$	Top mass (GeV/ $c^2$ )
SVX Double	5	$0.03 \pm 0.02$	$170.0^{+9.4}_{-8.9}$
SVX Single	15	$0.15^{+0.05}_{-0.04}$	$178.0^{+8.5}_{-7.6}$
SLT	14	$0.53 \pm 0.09$	$140.6^{+40.5}_{-14.6}$
No Tags	42	$0.69^{+0.09}_{-0.10}$	$182.1^{+11.7}_{-9.9}$
All subsamples	76	$0.51 \pm 0.06$	$176.1^{+5.2}_{-5.0}$

Table 8.1: Results of applying the mass likelihood procedure to the four subsamples and for all subsamples combined. The background fractions are constrained to their expected values via the curves in Fig. 4.1. For the four subsamples, we show the fitted background fraction and the fitted top mass. Also shown is the final mass value obtained when combining all four subsamples. The combined background fraction is the average of the  $x_b$  fit results weighted by the number of events in the subsamples.

## 8.2 Comparison of data to expectations

Up to this point we have assumed that our data sample is a mixture of standard model  $t\bar{t}$  signal plus background. Using simulated experiments (with  $M_{top} = 175$  GeV/ $c^2$ ), we quantify the probability that our data sample is consistent with a mixture of  $t\bar{t}$  plus background with the background fractions given in Table 8.1.

We first check that the statistical uncertainty obtained from the data sample (5.1 GeV/ $c^2$ ) is reasonable. Figure 8.3 shows the distribution of statistical uncertainties from simulated experiments along with the value we obtain for our data sample. We find that 5% of simulated experiments yield a statistical uncertainty equal to or smaller than the value from our data sample. While this number is small, it is reasonable.

A further check is provided by comparing the minimum of the negative log-likelihood obtained in the data sample with the values obtained from a large sample of simulated experiments (Fig. 8.4). A value of the negative

Data sample	Number of events	$x_b^{fit}$	Top mass (GeV/ $c^2$ )
SVX Double	5	$0.0^{+0.6}_{-0.0}$	$169.9^{+9.2}_{-8.7}$
SVX Single	15	$0.0^{+1.1}_{-0.0}$	$177.6^{+7.8}_{-7.1}$
SLT	14	$0.0^{+0.8}_{-0.0}$	$146.2^{+26}_{-16}$
No Tags	42	$0.53 \pm 0.22$	$180.8^{+10.1}_{-8.3}$
All subsamples	76	$0.29 \pm 0.20$	$176.2 \pm 4.8$

Table 8.2: Results of applying the mass likelihood procedure to the four subsamples and for all subsamples combined. The background fractions are free parameters in the mass likelihood fit. For the four subsamples, we show the fitted background fraction and the fitted top mass. Also shown is the final mass value obtained when combining all four subsamples. The combined background fraction is the average of the  $x_b$  fit results weighted by the number of events in the subsamples.

log-likelihood larger than expected from simulated experiments might indicate that either the reconstructed-mass distribution is not well modeled or that the background fractions in the sample are not properly estimated. The distribution shows that the value obtained from the data is quite consistent with standard model  $t\bar{t}$  plus background, as evidenced by the 79% probability of obtaining a value of  $-\log \mathcal{L}$  larger than the one seen in the data.

### 8.3 Results from $b$ -tagged events

In previous publications [1, 2], the top quark mass was measured using only events containing SVX and/or SLT tagged jets among the leading four jets as a single sample (7 events in Ref [1], 19 events in Ref [2]). The final sample of 34  $b$ -tagged events has been analyzed as part of our four subsample fit using the likelihood method described in Sections 6 and 7. The 34 tagged events may be treated as three subsamples or they may be fit as a single 34

event sample [58]. The results of fitting the 34  $b$ -tagged events as a single sample are shown in Fig. 8.5. The likelihood fit yields a top quark mass of  $173.7 \pm 6.2(\text{stat.}) \text{ GeV}/c^2$  with a top fraction of 75%. Treating the 34  $b$ -tagged events as three subsamples, we obtain a top quark mass of  $174.0 \pm 5.7(\text{stat.}) \text{ GeV}/c^2$ . The 8% improvement is consistent with expectations from simulated experiments (see Section 3.3.1).

## 8.4 Alternate techniques

Other analyses which have different selection criteria and/or modified formulations of the  $\chi^2$  have been performed. The analyses are aimed at improving the probability for choosing the correct combination. The first of these analyses, the  $\mathcal{L}^{**}$  analysis, uses two additional terms in the  $\chi^2$  to aid in choosing the correct combination. The second analysis uses a looser definition for  $b$ -jet tagging to increase the number of double  $b$ -tagged events. Values of the top quark mass from these two analyses are consistent with the results presented in this report and are summarized in Appendix B.

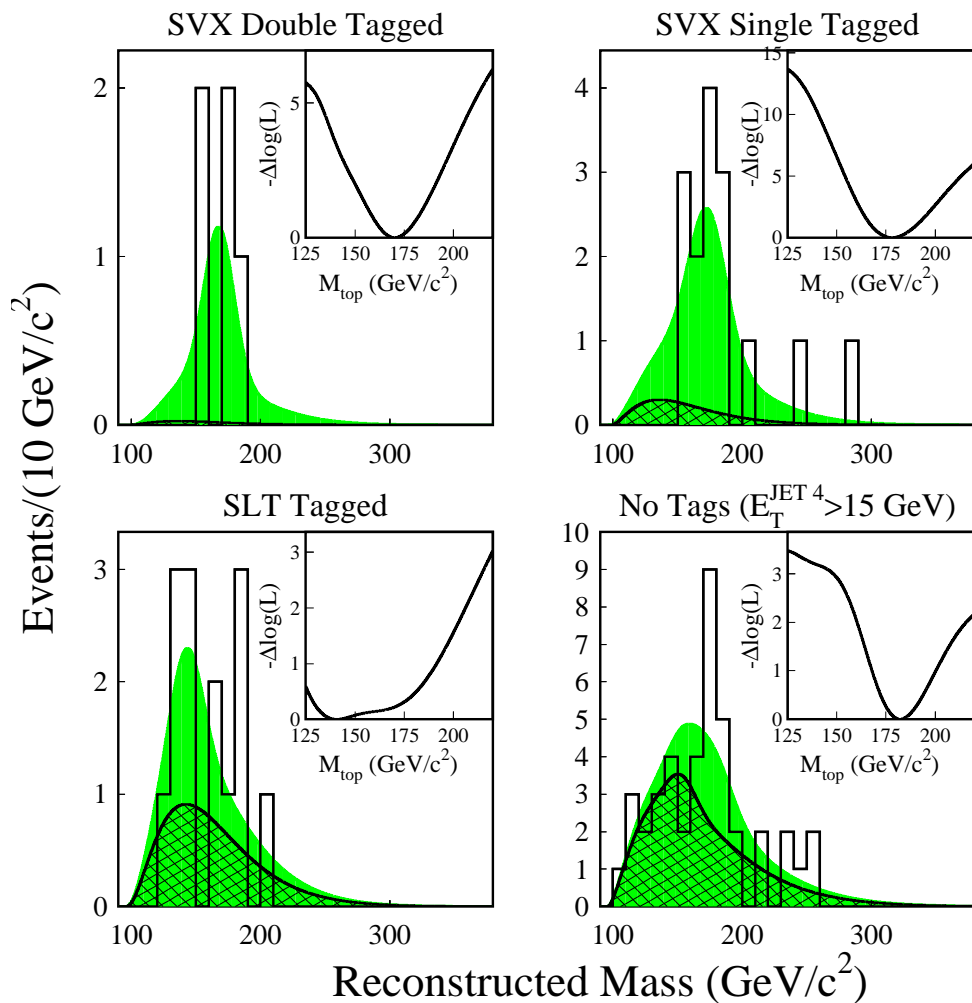


Figure 8.1: Results of applying the likelihood procedure to the four subsamples. The figure shows the data (histogram), fitted background (shaded hatched region), and fitted signal (shaded non-hatched region). The insets show the shapes of  $-\log \mathcal{L}$  versus top mass, from which we extract the fitted top quark mass and its statistical uncertainty.

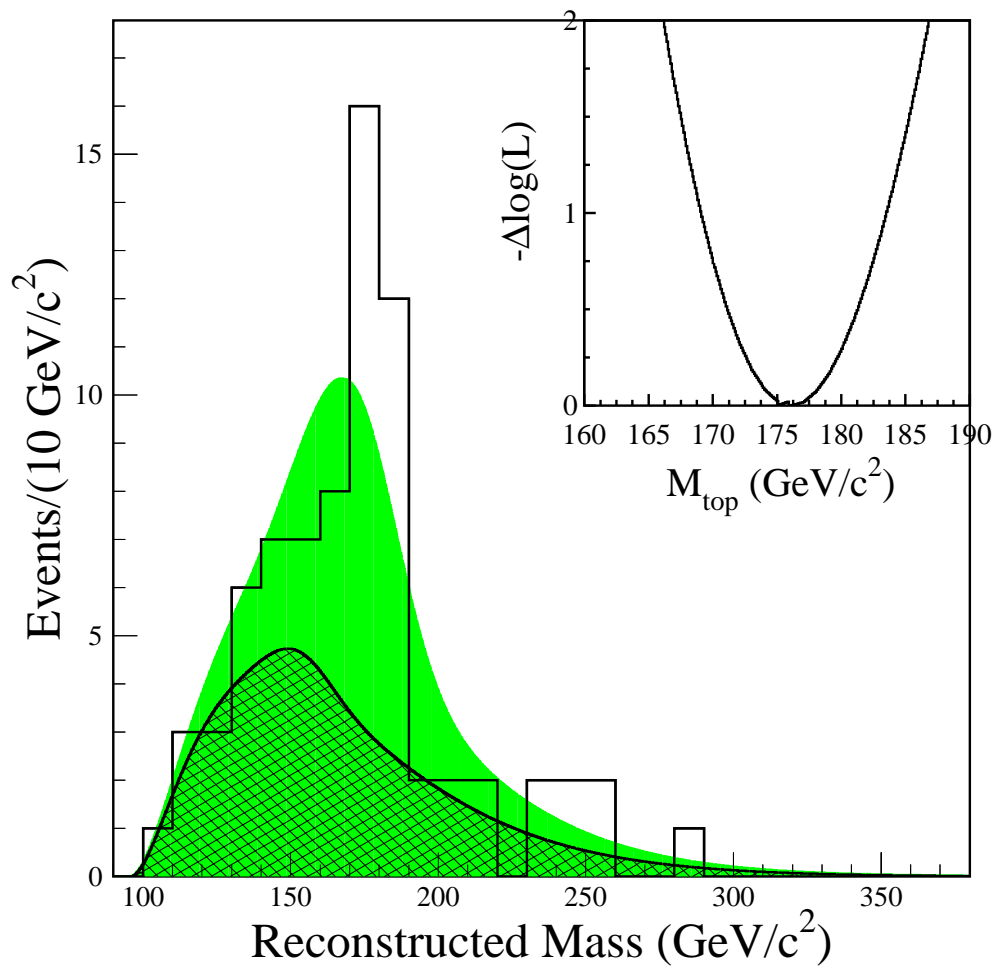


Figure 8.2: Result of applying the likelihood procedure to the combined sub-samples. The figure shows the data (histogram), fitted background (shaded hatched region), and fitted signal (shaded non-hatched region). The inset shows the shape of  $-\log \mathcal{L}$  versus top mass, from which we extract the best estimate of the top quark mass and its statistical uncertainty.



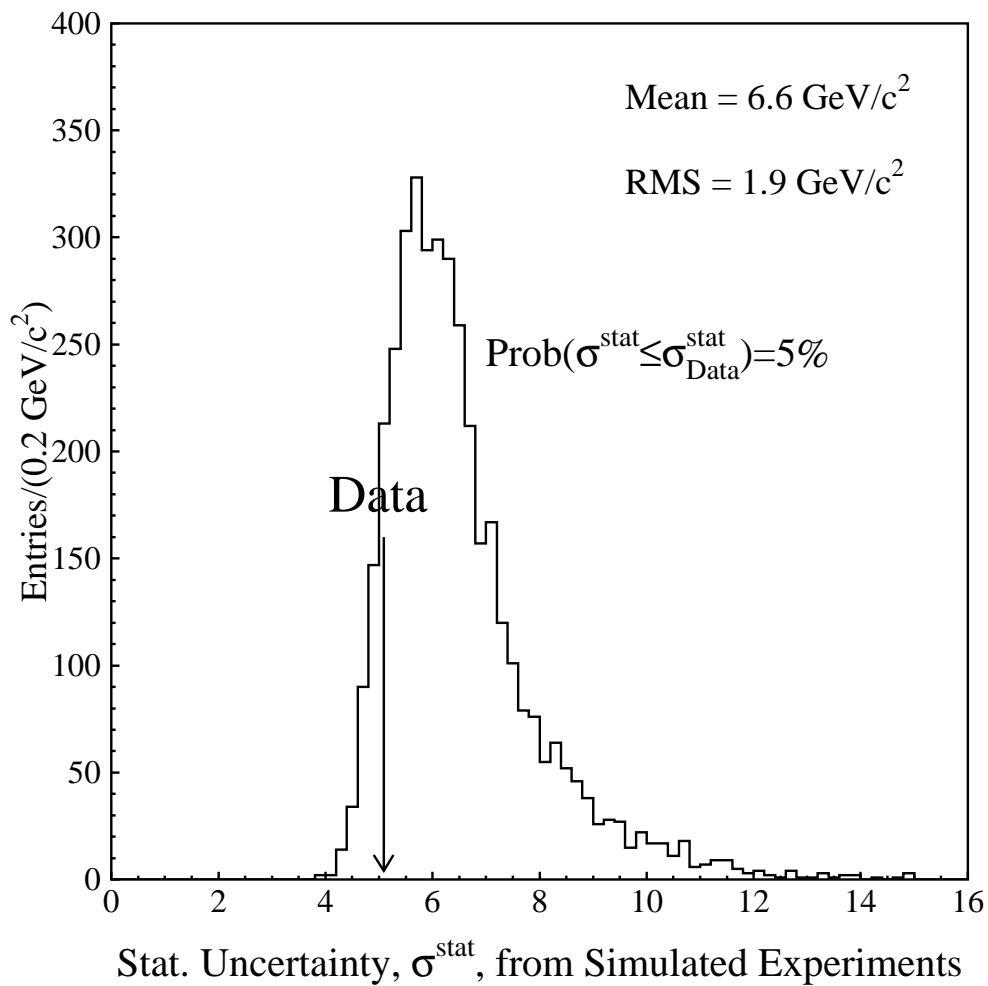


Figure 8.3: Distribution of statistical uncertainties from simulated experiments of  $t\bar{t}$  ( $M_{top} = 175 \text{ GeV}/c^2$ ) plus background. Each simulated experiment contains a mixture of signal and background events as described in the text. Also shown is the statistical uncertainty obtained from our data sample. The probability for obtaining a smaller uncertainty in the simulated experiments is 5%.

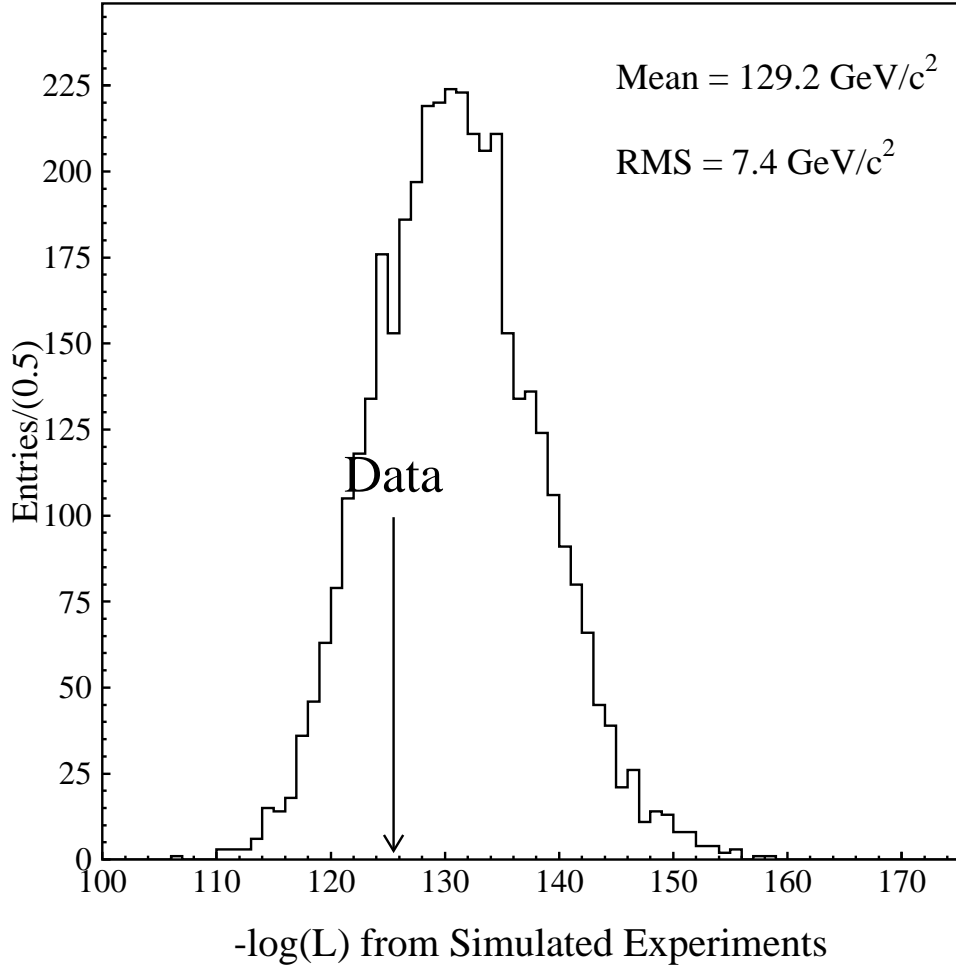


Figure 8.4: Distribution of the minimum value of  $-\log \mathcal{L}$  from simulated experiments of  $t\bar{t}$  ( $M_{top} = 175 \text{ GeV}/c^2$ ) plus background. Each simulated experiment contains a mixture of signal and background events as described in the text. Also shown is the minimum  $-\log \mathcal{L}$  value obtained from our data sample. The probability for obtaining a larger value of  $-\log \mathcal{L}$  in the simulated experiments is 79%.

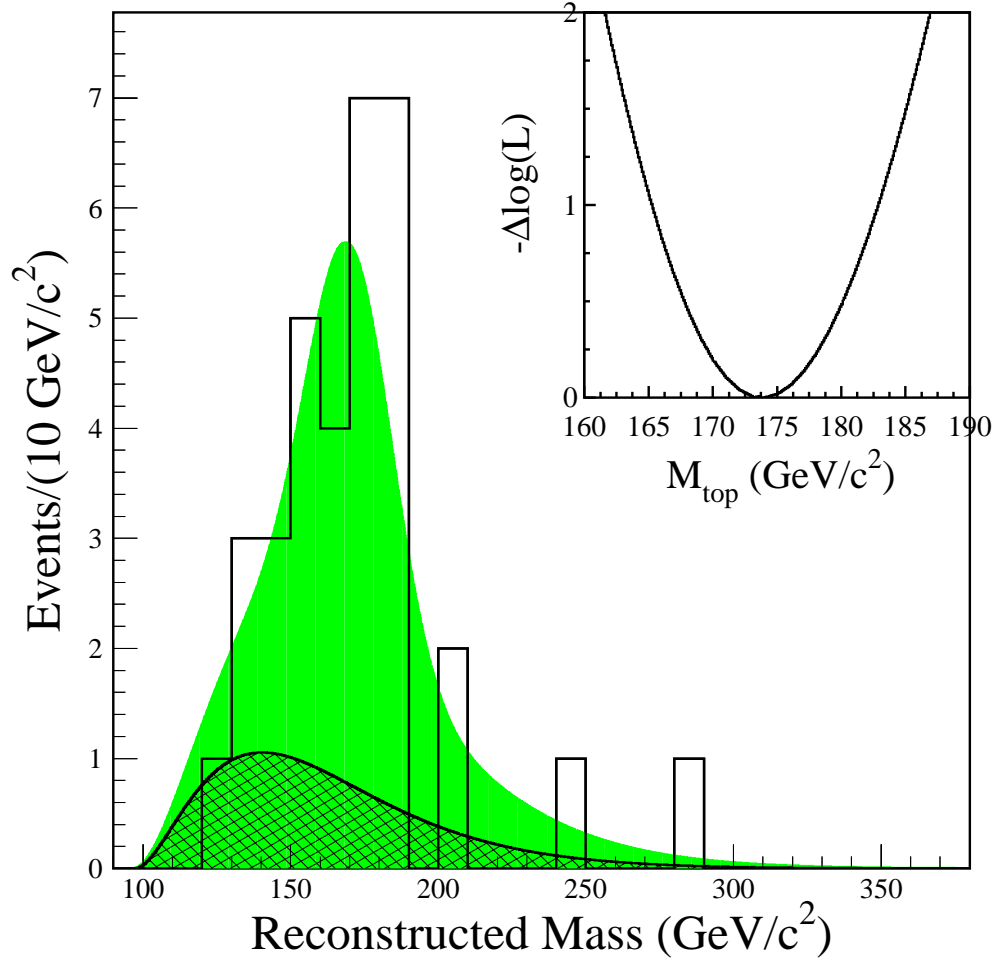


Figure 8.5: Result of applying the likelihood procedure to the 34  $b$ -tagged events, treated as a single sample. The figure shows the data (histogram), fitted background (shaded hatched region), and fitted signal (shaded non-hatched region). The inset shows the shape of  $-\log \mathcal{L}$  versus top mass, from which we extract the top quark mass and its statistical uncertainty.

# Section 9

## SYSTEMATIC UNCERTAINTIES

The general procedure for estimating the systematic uncertainty on  $M_{top}$  from a given source is handled similarly for all sources. For a given source of uncertainty, we make a change in the input value, and evaluate the impact on the measured top quark mass. The change is either a one standard deviation ( $1\sigma$ ) uncertainty on the variable in question, or a change in an input assumption. The change in the top quark mass is evaluated using simulated experiments (see Section 7.3). We perform a large number of simulated experiments with (a) the nominal input value of the variable or the standard assumption, and (b) a “ $1\sigma$ ” shift in the variable value or the changed assumption. The reconstructed-mass distribution from each simulated experiment is fit using the same likelihood procedure as used on the data sample, thus obtaining a measured top quark mass. The likelihood procedure includes the same templates as used with the data. The systematic uncertainty is defined as the difference in the median top quark mass between the two ensembles (a) and (b). The distribution of reconstructed top quark masses from simulated

experiments in which all inputs are set to their nominal values was shown in Fig. 7.6.

## 9.1 Uncertainties from the energy scale

The event reconstruction algorithm varies the measured momenta of the jets, leptons, and unclustered energy to fit the kinematics of the hypothesized  $t\bar{t}$  decay. The energy scale for electrons and the momentum scale for muons are known to a precision of 0.14% and 0.065% respectively [31]. This uncertainty has a negligible effect on the uncertainty in the top quark mass measurement. The uncertainty on the quantity  $X_T$ , the transverse energy beyond the partons associated with the  $t\bar{t}$  event, has been discussed in Section 5.2. This uncertainty is large, but large variations of  $X_T$  do not have a significant impact on the mass reconstruction. The  $\cancel{E}_T$  is evaluated through the measurements of the charged lepton, the jets, and the unclustered energy, and is therefore not an independent measurement (see Section 5.2). To avoid correlations it is not used as a measurement in the fit, but is used to estimate a starting value for the transverse momentum of the neutrino. Thus, the energy scale uncertainty in the measured top quark mass is dominated by the uncertainty in the measurement of the jet momenta.

The total uncertainty in the jet  $P_T$  scale is taken as the quadrature sum of all uncertainties discussed in Section 5.1. We apply  $+1\sigma$  and  $-1\sigma$  shifts to the jet momenta in  $t\bar{t}$  signal and background events, and measure the effect on the measurement of the top quark mass. For the SVX Single subsample, the distributions of reconstructed masses for  $-1\sigma$  and  $+1\sigma$  shifts in the  $P_T$  scale are shown in Figs. 9.1(a) and (c) respectively. These distributions may be compared to Fig. 9.1(b) which shows the distribution obtained from the default momentum scale. As expected, a clear shift in the reconstructed-mass spectrum is observed. We generate analogous distributions for the other three

mass subsamples and for the background mass distribution. To obtain the systematic uncertainty, we generate two large samples of simulated experiments. In the first sample, we choose the reconstructed masses for  $t\bar{t}$  events at random from distributions like the one in Fig. 9.1(a). In the second sample, we use distributions like the one in Fig. 9.1(c). The simulated experiments in each of these samples are fit using the standard templates and the likelihood technique described in Section 7. The median top mass from the simulated experiments in the two samples differ because of the applied jet  $P_T$  scale shifts. The distribution of reconstructed top masses from the two (jet  $P_T$  shifted) samples are displayed in Fig. 9.2. We take half the difference between the medians of the  $-1\sigma$  and  $+1\sigma$  distributions (from Fig. 9.2) as the uncertainty on the top quark mass measurement due to the  $P_T$  scale uncertainty. Using this prescription, we obtain a top mass uncertainty of  $\pm 4.4 \text{ GeV}/c^2$  from the jet  $P_T$  scale.

## 9.2 Initial and final state hard radiation

QCD radiation that produces jets can originate from the outgoing (final state) partons, the incoming (initial state) partons, or from interference among the two. The interference effect is expected to be small [56] and is not considered here.

The effects of initial state radiation (ISR) and final state radiation (FSR) on the measurement of  $M_{top}$  are studied using the PYTHIA program since it allows the two effects to be studied in isolation from one another. The approach used to evaluate the systematic uncertainty due to ISR is to compare the median mass from simulated experiments using the standard PYTHIA settings to the median mass from simulated experiments with ISR turned off. The median mass from simulated experiments for the no-ISR PYTHIA sample is found to be lower than that of the standard PYTHIA sample by  $2.6 \text{ GeV}/c^2$ . The uncertainty is taken to be one half of the shift in median mass between

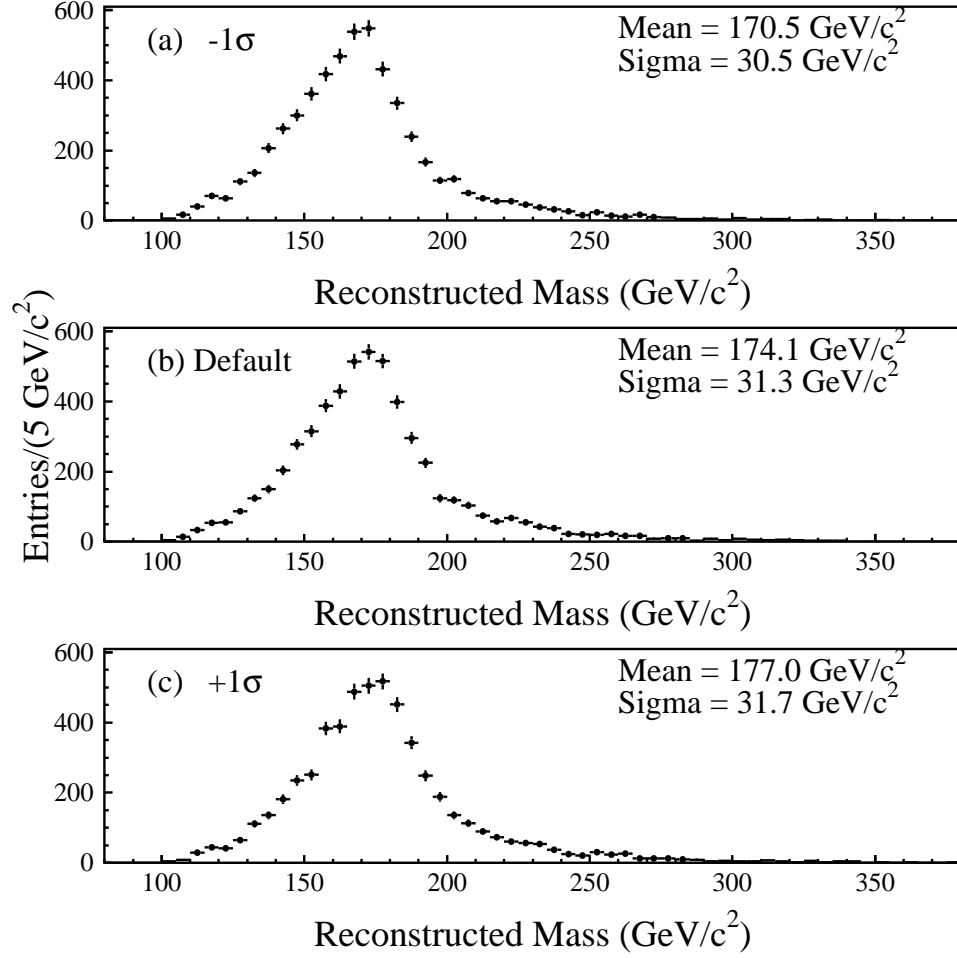


Figure 9.1: Distribution of reconstructed masses for SVX Single tagged events from the HERWIG  $t\bar{t}$  Monte Carlo simulation using an input top mass  $175 \text{ GeV}/c^2$  for (a) a  $-1\sigma$  shift in the jet  $P_T$  scale, (b) no shift in the jet  $P_T$  scale, and (c) a  $+1\sigma$  shift in the jet  $P_T$  scale. These distributions are used as inputs to generate the samples of simulated experiments described in the text.

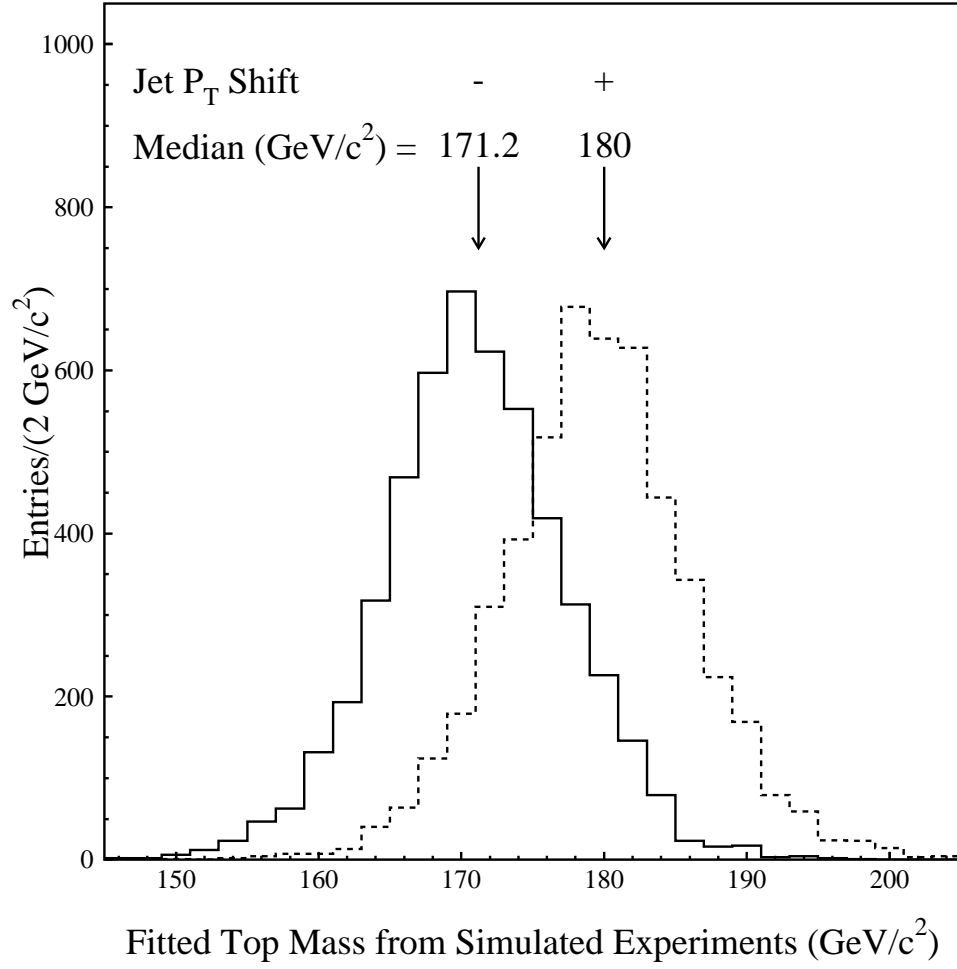


Figure 9.2: Distribution of fitted top masses returned from the likelihood procedure for simulated experiments. The solid histogram shows the distribution when the jet  $P_T$  scale is shifted down by  $-1\sigma$ , and the dashed histogram shows the results when the jet  $P_T$  scale is shifted up by  $+1\sigma$ . The median top masses for each are indicated on the figure, from which we obtain a systematic uncertainty of  $4.4 \text{ GeV}/c^2$ .



the standard PYTHIA simulation and the no-ISR PYTHIA simulation, which is  $1.3 \text{ GeV}/c^2$ . We assume that the shift is symmetric with the amount of ISR and therefore the uncertainty is  $\pm 1.3 \text{ GeV}/c^2$ .

Extracting the effects due to final state radiation is a more subtle exercise because PYTHIA, like HERWIG, describes jet formation through a parton shower. The effects of modeling the softer components on the measurement of  $M_{top}$  are described by the studies of soft gluon radiation (see Section 5.1.1). In this discussion, we are therefore referring to the “harder” component of FSR, which leads to extra jets in the final state. To isolate the effect of FSR, we use a sample of PYTHIA events which have ISR turned off. We select a subsample of these events that have exactly four jets (either four high- $E_T$  jets,  $E_T > 15 \text{ GeV}$  and  $|\eta| < 2.0$ , or three high- $E_T$  jets plus one with  $E_T > 8 \text{ GeV}$  and  $|\eta| < 2.4$ ), all of which can be uniquely matched to the partons from  $t\bar{t}$  decay (within a cone of 0.4). Using the procedure of simulated experiments, we take the systematic uncertainty to be half the difference between the no-ISR PYTHIA events with no restriction on the number of jets and the subsample of events with exactly four jets uniquely matched to the partons from  $t\bar{t}$  decay. We assume that this difference is approximately independent of the amount of ISR present. The median top mass from the no-ISR sample with exactly four jets is found to be larger than the default no-ISR sample by  $4.4 \text{ GeV}/c^2$ . The systematic uncertainty is taken to be one half of the difference in the median top masses between the two samples, or  $2.2 \text{ GeV}/c^2$ . As with ISR, we assume that the shift in top mass is symmetric with respect to the amount of FSR, so the systematic uncertainty is  $\pm 2.2 \text{ GeV}/c^2$ .

### 9.3 Background mass distribution

In generating the default background distributions with the VECBOS program, we used the  $W+3$  partons matrix elements and chose a scale of

$Q^2 = \langle P_T \rangle^2$ . This  $Q^2$  scale is not only used in VECBOS for the computations of the matrix elements and the evaluation of the parton distribution functions, but it is also used in the evolution of the parton showers to limit the  $P_T$  of additional jets [59]. As a result, the shape of the reconstructed-mass distribution is sensitive to the choice of scale. The systematic uncertainty from using the assumed background shape was evaluated by changing the  $Q^2$  scale from  $\langle P_T \rangle^2$  to  $M_W^2$ . Simulated experiments using  $t\bar{t}$  and the modified background shape ( $Q^2 = M_W^2$ ) were fit to the default signal and background probability distributions as described in Section 7. The median mass from these simulated experiments was found to differ by  $1.3 \text{ GeV}/c^2$  from simulated experiments using the default background shape. The systematic uncertainty from the background shape modeling is taken to be this difference symmetrized, or  $\pm 1.3 \text{ GeV}/c^2$ .

## 9.4 $b$ -Tagging

A systematic uncertainty in the top mass measurement may arise from an uncertainty in the SVX and SLT tagging efficiencies. For SVX tagging, the primary uncertainty comes from the possible  $E_T$  dependence of the SVX tagging efficiency which may differ from the simulation. The SVX tagging efficiency in data relative to the simulation is parametrized as a function of the jet  $E_T$ , and is nearly flat. The systematic uncertainty is evaluated by assuming the largest possible  $E_T$  dependence of this ratio given the available statistics. Comparison of results obtained using a flat ratio to those obtained with a sloped one gives a mass shift of only  $0.1 \text{ GeV}/c^2$ .

The jet  $E_T$  dependence of the SLT tagging efficiency is better known than in the SVX case. However, a systematic uncertainty does arise from the uncertainty in the expected ratio of true to fake SLT tags in  $t\bar{t}$  events. To estimate the sensitivity of our top quark mass measurement to this ratio, we

generate Monte Carlo  $t\bar{t}$  events in which all SLT tags are either (a) true tags, or (b) fake tags. We then produce two large samples of simulated experiments, each having the same number of observed events as in our four mass subsamples and including the appropriate background contributions. The two samples of simulated experiments consist of either events all from set (a) or all from set (b). The median top quark mass values from the two samples of simulated experiments differ by  $0.8 \text{ GeV}/c^2$ . We take half of this difference, or  $0.4 \text{ GeV}/c^2$ , as the corresponding systematic uncertainty in the top quark mass. Combining the systematic uncertainties from SVX and SLT tagging, we find an overall systematic uncertainty of  $\pm 0.4 \text{ GeV}/c^2$ .

## 9.5 Parton distribution functions

All of the Monte Carlo samples used to measure the top mass were generated with the MRSD0' [37] set of parton distribution functions (PDF). This was the preferred PDF at the time the samples were generated. Newer distribution functions now exist, in particular ones which fit CDF's inclusive jet cross section. One such PDF, CTEQ4L [60], provides a higher gluon content at lower momentum fraction than MRSD0'. We take the shift in the median top mass between samples generated with the two PDF's as the relevant uncertainty. We therefore assign a systematic uncertainty of  $\pm 0.3 \text{ GeV}/c^2$  in the top quark mass from this source.

## 9.6 Monte Carlo generators

The effect of using different Monte Carlo generators has also been studied. Previously, this was evaluated from the difference between the HERWIG and ISAJET simulations. Because of the evidence that independent fragmentation does not reproduce some aspects of the data (energy flow around

and between jets [61, 9]) we will not use ISAJET here. We evaluate the systematic uncertainty from the choice of Monte Carlo generators via the mass shift between the HERWIG and PYTHIA simulations. This gives a systematic uncertainty of  $\pm 0.1 \text{ GeV}/c^2$ .

## 9.7 Summary of systematic uncertainties

The relevant systematic uncertainties studied for the top mass measurement are listed in Table 9.1. Combining all of these effects in quadrature gives a total systematic uncertainty of  $\pm 5.3 \text{ GeV}/c^2$ , or  $\pm 3\%$  of  $176.1 \text{ GeV}/c^2$ .

Source	Uncertainty ( $\text{GeV}/c^2$ )
Jet energy measurement	4.4
Initial and final state radiation	2.6
Shape of background spectrum	1.3
$b$ -Tagging	0.4
Parton distribution functions	0.3
Monte Carlo generators	0.1
Total	5.3

Table 9.1: Systematic uncertainties on the measurement of the top quark mass for this analysis.

# Section 10

## COMBINED TOP QUARK MASS

The most precise measurement of the top quark mass in any single decay channel is obtained with events in the lepton+jets topology. The analysis of such events leads to a mass of  $176.1 \pm 5.1(\text{stat.}) \pm 5.3(\text{syst.}) \text{ GeV}/c^2$ . Measurements in the all-hadronic [10] and dilepton [62] decay topologies have also been made and can be combined with the lepton+jets result to reduce the overall uncertainty. Here we make some brief remarks on these analyses, and describe how the three measurements were combined.

### 10.1 All-hadronic topology

The top quark mass measurement in the all-hadronic topology used a sample of 136 events that satisfied several selection criteria, including the requirement of six or more jets, at least one of which was tagged as a  $b$  by the SVX. The estimated background in the sample was  $108 \pm 9$  events. The method for extracting a top mass was similar to the one used for the lepton+jets topology, and included a kinematic fit to each event and a likelihood fit to

the resulting reconstructed-mass distribution. The results of the likelihood fit yielded a measured top quark mass of  $186 \pm 10(\text{stat.}) \pm 12(\text{syst.}) \text{ GeV}/c^2$  [10]. A reevaluation of the systematic uncertainty on this measurement has led to a more accurate estimate of  $5.7 \text{ GeV}/c^2$  [62]. Appendix C describes the details of this reevaluation.

## 10.2 Dilepton topology

The dilepton topology includes  $t\bar{t}$  events in which the  $W^+$  and  $W^-$  bosons each decay into an  $e\nu$  or  $\mu\nu$  final state. The presence of two neutrinos, which are not observed in our detector, prevents a straightforward event-by-event kinematic fit to the  $t\bar{t}$  decay hypothesis. Therefore, we have measured the top quark mass from dilepton events using a weighting method [13, 63, 64]. In this method the vector sum of the neutrino transverse momenta, as predicted after making certain assumptions, is compared to the observed missing transverse momentum [62]. From a sample of eight events with an estimated background of  $1.3 \pm 0.3$  events we obtain a mass of  $167.4 \pm 10.3(\text{stat.}) \pm 4.8(\text{syst.}) \text{ GeV}/c^2$ . A brief description of the method, and some additional information not reported in Ref. [62] is given in Appendix C.

## 10.3 Combining the measurements

Each of the three top quark mass measurements is associated with a statistical and systematic uncertainty. The statistical uncertainties are uncorrelated, since the samples are statistically independent. However, the systematic uncertainties are correlated, and these correlations must be included when combining the results.

The systematic uncertainties in the measurements from each decay topology [62] are assigned to one of five independent categories:

1. jet energy scale,
2. signal model (ISR, FSR, PDF,  $b$ -tagging),
3. Monte Carlo generator,
4. background model,
5. Monte Carlo statistics.

The assignment of the systematic uncertainties for each of the three mass analyses to these categories is shown in Table 10.1. In the lepton+jets measurement, the statistical uncertainty in the Monte Carlo simulation is included in the global statistical uncertainty.

Systematic category	Systematic uncertainty ( $\text{GeV}/c^2$ )		
	Lepton+jets	All-hadronic	Dilepton
Jet energy scale	4.4	5.0	3.8
Signal model	2.6	1.8	2.8
M.C. generators	0.1	0.8	0.6
Background model	1.3	1.7	0.3
M.C. statistics	-	0.6	0.7
Total	5.3	5.7	4.8

Table 10.1: Systematic uncertainties for each of the three mass analyses grouped into the five categories. Also shown is the total systematic uncertainty for each analysis.

For each of the five categories, the systematic uncertainties in each of the three measurements are assumed to be either uncorrelated or 100% correlated. The jet energy scale uncertainty is taken to be 100% correlated since all three analyses use the same detector and the same jet clustering algorithm. The systematic uncertainties coming from the signal model and the Monte Carlo generator are also assumed to be 100% correlated since all three analyses use the HERWIG Monte Carlo generator to simulate  $t\bar{t}$  events. The

uncertainties in the background shape are assumed to be uncorrelated because the background processes for each analysis are different. The correlation coefficients between the three pairs of analyses are given in Table 10.2.

Systematic category	Correlation coefficients		
	LJ/AH	LJ/LL	AH/LL
Jet energy scale	1.0	1.0	1.0
Signal model	1.0	1.0	1.0
M.C. generators	1.0	1.0	1.0
Background model	0.0	0.0	0.0
M.C. statistics	0.0	0.0	0.0

Table 10.2: Correlation coefficients between the three mass analyses for the five categories of systematic uncertainty. Here, LJ signifies the lepton+jets analysis, AH the all-hadronic analysis, and LL the dilepton analysis.

The inputs into the calculation for combining the mass measurements are the three top quark mass measurements cited in this section, their statistical uncertainties, and the systematic uncertainties and their correlations as listed in Tables 10.1 and 10.2. The calculation uses a generalized chisquare method with full covariance matrix (see for example [65]), and yields:

$$m_t = 176.1 \pm 6.6 \text{ GeV}/c^2. \quad (10.1)$$

In the calculation, the central value can be written as the weighted sum of the three input central values. The weights, which depend on the statistical and systematic uncertainties and the correlations, are found to be 0.65 (lepton+jets), 0.19 (dilepton), and 0.16 (all-hadronic). If we define a statistical uncertainty on the combined result as the quadrature sum of the weighted individual statistical uncertainties, that combined statistical uncertainty is  $\pm 4.2 \text{ GeV}/c^2$ . The combined systematic uncertainty, defined as the quadrature difference between the total and statistical uncertainties, is then  $\pm 5.1 \text{ GeV}/c^2$ .



# Section 11

## SUMMARY

The first evidence of the production of top quark pairs in  $p\bar{p}$  collisions was reported by CDF in 1994 [1]. From a sample of seven candidate lepton+jets events with an expected background of 1.4 events, the top quark mass was measured to be  $174 \pm 10(\text{stat})_{-12}^{+13}(\text{syst}) \text{ GeV}/c^2$ . Since that time, both CDF and D0 have analyzed their full Run 1 data samples and have published their measurements of the  $t\bar{t}$  production cross section [7, 8] and top quark mass [5, 6]. Indirect measurements of the top quark mass using data from LEP and SLC have been made [17], and are consistent with the direct measurements, although with a substantially larger uncertainty.

This report has described in detail the best single channel measurement of the top quark mass. A letter on the measurement is already published [6]. The likelihood method uses parametrized templates, which results in a continuous likelihood shape as a function of the top quark mass from which the top quark mass and statistical uncertainty are evaluated. The statistical precision of the top quark mass measurement has benefitted from a larger data sample than earlier measurements [1, 2], and through subdivision of the data sample into non-overlapping subsamples according to the  $b$ -tagging information. Systematic uncertainties have been considerably reduced, primarily

through a better understanding of the jet energy measurements which resulted in smaller uncertainties on jet  $P_T$ .

From the  $106 \text{ pb}^{-1}$  Run 1 data sample, we measure the top quark mass in the lepton+jets topology to be  $176.1 \pm 5.1(\text{stat.}) \pm 5.3(\text{syst.}) \text{ GeV}/c^2$ . Measurements of the top quark mass in the all-hadronic [10] and dilepton [62] decay topologies are consistent with this measurement. Combination of the three measurements from CDF gives a top quark mass of  $176.1 \pm 6.6 \text{ GeV}/c^2$ . The D0 collaboration has also published results on the top quark mass measurement in the lepton+jets and dilepton channels, from which they obtain a combined top quark mass of  $172.1 \pm 7.1 \text{ GeV}/c^2$  [66]. The measurements of the top quark mass from the CDF and D0 experiments are consistent with each other, therefore, their Run 1 measurements have been combined to obtain a top quark mass at the Tevatron of  $174.3 \pm 5.1 \text{ GeV}/c^2$  [67]. This measurement represents the most precise measurement of any of the quark masses.

We thank the Fermilab staff and the technical staffs of the participating institutions for their vital contributions. This work was supported by the U.S. Department of Energy and National Science Foundation; the Italian Istituto Nazionale di Fisica Nucleare; the Ministry of Education, Science, Sports and Culture of Japan; the Natural Sciences and Engineering Research Council of Canada; the National Science Council of the Republic of China; the Swiss National Science Foundation; the A. P. Sloan Foundation; the Bundesministerium fuer Bildung und Forschung, Germany; and the Korea Science and Engineering Foundation.

# **Appendix A**

## **EVENTS IN THE MASS ANALYSIS**

The individual reconstructed masses of all events in the four subsamples are listed in Tables A.1 through A.4.

Run	Event	Mass (GeV/ $c^2$ )
40758	44414	175.3
67824	281883	170.1
65581	322592	152.7
67971	55023	183.5
68464	547303	151.1

Table A.1: List of events which are in the SVX Double subsample. Shown are the run and event numbers and the reconstructed top mass for the solution having the lowest  $\chi^2$ .

Run	Event	Mass (GeV/ $c^2$ )
43096	47223	288.6
45610	139604	180.0
45879*	123158	180.1
59698*	31639	187.4
63247	65096	161.0
63641	3054	173.3
68006	44672	243.4
64901	569801	156.3
69683*	135095	163.2
56911*	114159	156.7
67515	298909	174.6
68312*	821014	202.4
68739	425355	170.9
69781*	266905	182.8
56669	21631	152.1

Table A.2: List of events which are in the SVX Single subsample. Shown are the run and event numbers and the reconstructed top mass for the solution having the lowest  $\chi^2$ . Events labelled with a \* have both SVX and SLT tagged jets.

Run	Event	Mass (GeV/ $c^2$ )
45705	54765	186.3
45880	31838	130.4
43351	266423	162.4
66368	91765	137.9
66500	421896	173.0
67879	30394	141.1
69005	181134	129.6
58908	41102	138.6
60998	423792	162.0
61334	57897	183.1
64721*	229200	181.0
65298*	747402	149.4
65648	203840	203.2
67515	616477	149.9

Table A.3: List of events which are in the SLT subsample. Shown are the run and event numbers and the reconstructed top mass for the solution having the lowest  $\chi^2$ . Events labelled with a \* have two SLT-tagged jets.

Run	Event	Mass (GeV/ $c^2$ )	Run	Event	Mass (GeV/ $c^2$ )
46492	57501	179.2	58696	83095	137.6
41301	45902	175.7	59948	105232	115.4
43421	65648	147.8	60634	350037	151.2
47757	262594	219.6	61167	332223	167.3
45757	30003	173.0	63265	5385	255.2
45144	107403	189.2	64041	473567	247.5
60656	96710	180.3	64997	78806	192.0
60746	121257	180.1	65179	215794	195.7
61511	75858	113.0	67391	50780	184.9
62981	85084	125.0	67757	631972	172.0
64861	121618	178.8	68144	100373	178.3
64934	400688	215.4	68231	78554	177.7
66046	507038	164.2	68374	312573	139.1
66207	12039	154.4	68553	707057	130.4
66315	365275	230.3	68570	897728	142.6
67862	631243	114.2	68593	88427	144.0
68006	176291	120.9	69519	430034	160.0
68939	352425	173.1	70000	26023	161.1
69520	307639	235.2	57438	71994	253.1
70578	351956	143.0	64901	505659	108.1
70986	227609	176.2	67397	105755	190.0

Table A.4: List of events which are in the No Tag subsample. Shown are the run and event numbers, and the reconstructed top mass for the solution having the lowest  $\chi^2$ .

# Appendix B

## ALTERNATE MASS ANALYSES

A number of alternate mass analyses have been performed using the Run 1 data sample. We discuss two alternate analyses which are aimed at improving the statistical and/or systematic uncertainty on the top quark mass measurement using some subsample of events. Another goal is to check our default technique by employing complementary strategies by: (i) using more event information associated with  $b$  tagging and jet charge, and (ii) reducing the sample to the most complete events, ie. those where we have two  $b$ -tagged jets. The first of these techniques includes additional terms in the likelihood function, which improves the probability for choosing the correct jet-to-parton configuration at the expense of reduced statistics. The second technique uses three  $b$ -tagging algorithms to explore a subsample of the data set that consists of events with two  $b$ -tagged jets among the leading four jets. Neither of these two techniques is found to yield a more precise measurement than the mass analysis described in the body of this report. In this appendix, we briefly describe these two mass analyses.

## B.1 The $\mathcal{L}^{**}$ fitting technique

The  $\mathcal{L}^{**}$  technique [68] aims at improving the fraction of correct jet-to-parton assignments by combining three independent sources of event information into a single parameter. These sources are:

- $\chi^2$  for  $t\bar{t}$ -like kinematics as described in Section 6;
- probability for the jets assigned as  $b$  jets to originate from  $b$  quarks, and the two jets assigned to the hadronic W-decay to originate from light quarks. The probability is evaluated using the jet probability (JPB) algorithm [1, 69, 70];
- probability to observe a given jet charge [71] for  $b$  and  $\bar{b}$  quarks in  $t\bar{t}$  events.

### B.1.1 Definition of $\mathcal{L}^{**}$

The JPB algorithm evaluates for each charged track in a jet the probability that it comes from the primary vertex. For each jet the track probabilities are combined into an overall probability (JPB) that the jet is consistent with the zero lifetime hypothesis. Due to the long lifetime of  $b$  hadrons, the JPB distribution for  $b$  quark jets exhibits a strong peak near zero. Non- $b$  jets in  $t\bar{t}$  events are produced either through the decays of W-bosons to  $(u, d)$  and  $(c, s)$  quark pairs, or production of gluon jets from initial or final state radiation. With the exception of the charmed quarks, the non- $b$  jets exhibit a flat JPB distribution. The charm quark jets produce a small peak near zero which can be ignored given its relative size. Unless otherwise noted, charm quark jets are understood to be included in the “non- $b$ ” quark distribution of JPB.

We incorporate the JPB variable into the  $\chi^2$  definition by introducing



the following selection function:

$$\mathcal{L}^* = \chi^2 - 2 \cdot \ln [\mathcal{P}(\text{JPB}_1) \cdot \mathcal{P}(\text{JPB}_2) \cdot \mathcal{P}(\text{JPB}_3) \cdot \mathcal{P}(\text{JPB}_4)]. \quad (\text{B.1})$$

The  $\chi^2$  is the same as the one defined in Section 6, and  $\mathcal{P}(\text{JPB}_i)$  is the probability density for the  $i^{\text{th}}$ -jet assignment ( $i=1,\dots,4$ ). The  $\mathcal{P}$  functions in  $\mathcal{L}^*$  depend only on jet type, since one function is appropriate for both  $b$  and  $\bar{b}$  jets, and another for non- $b$  quarks. While the  $\chi^2$  value is in general different for each of the 24 combinations, only six distinct values occur for the second term in  $\mathcal{L}^*$ . Groups of four, corresponding to the interchange of the  $b$  and  $\bar{b}$  quarks (and the two neutrino  $P_Z$  solutions), have the same contribution from this second term.

We used the HERWIG Monte Carlo and the full CDF detector simulation to generate the ( $b$  and  $\bar{b}$ ) and non-( $b$  and  $\bar{b}$ ) [72] probability density distributions. We only considered events in which the leading four jets corresponded to the four primary partons from  $t\bar{t}$  decay, which limits us to 56% of the sample. Of this subset, we found that the largest fraction of correct assignments based on selecting combinations with minimum  $\mathcal{L}^*$  was 48%, which was obtained with a jet clustering cone size of 0.4 and a minimal track  $P_T$  of 1.0 GeV/ $c$ .

To incorporate additional information pertaining to the charge of the  $b$  and  $\bar{b}$  jets, we define a new selection function,

$$\mathcal{L}^{**} = \mathcal{L}^* - 2 \cdot \ln [\mathcal{C}(\mathcal{Q}_b) \cdot \mathcal{C}(\mathcal{Q}_{\bar{b}})], \quad (\text{B.2})$$

where  $\mathcal{C}(\mathcal{Q}_{jet})$  is the jet charge probability density. The jet charge is defined as in Ref. [71]:

$$\mathcal{Q}_{jet} = \frac{\sum_{i=1}^{n_{trk}} q_i \cdot |\vec{p}_i \cdot \vec{e}|^k}{\sum_{i=1}^{n_{trk}} |\vec{p}_i \cdot \vec{e}|^k}, \quad (\text{B.3})$$

where  $\vec{e}$  is the unit vector along the jet axis,  $q_i$  and  $\vec{p}_i$  are the charge and momentum of the  $i^{\text{th}}$  track, and the sum extends over all  $n_{trk}$  charged particles in a fixed cone around the jet. To determine optimal choices for the cone size

and the weighting factor  $k$ , we varied the jet cone size from 0.35 to 1.0 and  $k$  from 0.4 to 1.2, and compared the significance of separation between the  $b$  and  $\bar{b}$   $\mathcal{C}(Q_{jet})$  distributions. The results were relatively insensitive to the exact values of these parameters. Since we found no strong dependence on these parameters, we chose the same cone size as used to calculate the JPB probability and for simplicity selected  $k = 1$ .

### B.1.2 Event selection and number of expected background events

In this analysis we select events with at least one SVX or SLT tag. All of the standard lepton and jet corrections discussed previously in this paper are applied. A total of 34 events are accepted which are identical to the tagged events shown in Table 3.1. Since the JPB algorithm uses tracks reconstructed in the silicon vertex detector, we require that each event has at least one jet with associated SVX tracks. We also require that the combination with the lowest value of  $\mathcal{L}^{**}$  has a  $\chi^2$  (as defined in Section 6) less than 10. Only solutions in which a  $b$ -tagged jet is assigned to a  $b$  parton are considered. We find that 27 of the 34 events pass these requirements.

We take the combination with the lowest  $\mathcal{L}^{**}$  value as the most likely decay chain of the  $t\bar{t}$  into the four highest  $E_T$  jets. Monte Carlo studies show that switching from  $\chi^2$  to the  $\mathcal{L}^{**}$  selection increases the probability of making the correct jet-to-parton assignments. The probability of correctly assigning the four highest  $E_T$  jets to the  $t\bar{t}$  daughter partons increases from  $30.5 \pm 0.7\%$  to  $37.3 \pm 0.6\%$ . This fraction is “a priori” limited to a maximum of 56%, due to jets from ISR and FSR.

The number of expected background events for the 34 tagged events is estimated to be  $10.2 \pm 1.5$ , which includes a background of  $7.6 \pm 1.3$  for the 14 events with only SLT tags. This analysis reduces the number of SLT

tagged events from 14 to 7 (no SVX tagged events are cut out). Using the method described in Section 4.3, the expected background for the 7-event SLT sample was evaluated to be  $3.2^{+0.7}_{-0.6}$  events. We therefore calculate an expected background for the 27-event sample of  $5.8^{+1.1}_{-0.9}$  events, which corresponds to a background fraction  $x_b = 0.21^{+0.04}_{-0.03}$ .

### B.1.3 Result of the likelihood fit

The evaluation of the top mass uses the same techniques described in Section 7. The result of the fit is shown in Fig. B.1. The histogram represents the reconstructed mass distribution for the 27 data events. The shaded area corresponds to the background fraction returned by the fitting procedure, and the smooth curve shows the sum of the fitted background and signal contributions. The insert displays the likelihood shape with the background fraction constrained to  $0.21^{+0.04}_{-0.03}$ . The resulting fit yields:

$$M_{top} = 170.3^{+5.9}_{-5.4}(\text{stat.}) \text{ GeV}/c^2. \quad (\text{B.4})$$

The soundness of the procedure was tested using simulated experiments. Figure B.2(a) shows the pull distributions for simulated experiments, and Fig. B.2(b) shows the average (of the positive and negative) statistical uncertainty returned from the likelihood fit. The arrow indicates the fit result from the data sample. We find that 44% of simulated experiments have a statistical uncertainty smaller than measured in the data sample.

Using simulated experiments, we compared the expected statistical uncertainty from 34 tagged events using the standard kinematic fit with 27-event experiments using the  $\mathcal{L}^{**}$  technique. The studies indicated that for samples of this size, we could reduce the top quark mass measurement uncertainty by  $\approx 0.5 \text{ GeV}/c^2$  over the standard kinematic  $\chi^2$ , if we consider the 34 events as a single sample.

### B.1.4 Systematic uncertainties

The same categories of systematic uncertainties which were shown in Section 9 are present in this analysis. Moreover, we introduce a new systematic uncertainty which accounts for a possible difference in the tracking efficiency between data and simulation. This uncertainty is introduced because both the JPB algorithm and the jet charge calculation have some sensitivity to the tracking efficiency in jets. Using simulated experiments, we find an expected uncertainty in the top quark mass of  $0.9 \text{ GeV}/c^2$  from this source. The systematic uncertainties for the  $\mathcal{L}^{**}$  method are summarized in Table B.1.

Systematic uncertainty	Value ( $\text{GeV}/c^2$ )
Jet energy measurement	4.0
Initial and final state radiation	2.7
Shape of background spectrum	0.5
$b$ -Tagging	0.3
Parton distribution functions	0.6
Monte Carlo generators	0.8
Tracking efficiency	0.9
Total	5.1

Table B.1: Systematic uncertainties for the  $\mathcal{L}^{**}$  analysis.

In conclusion, the  $\mathcal{L}^{**}$  analysis technique has been applied to a 27-event subset of the 34 tagged events, and leads to a top quark mass measurement of  $170.3_{-5.4}^{+5.9} \text{ (stat.)} \pm 5.1 \text{ (syst.) GeV}/c^2$ . This value is in good agreement with the results presented in Section 8.

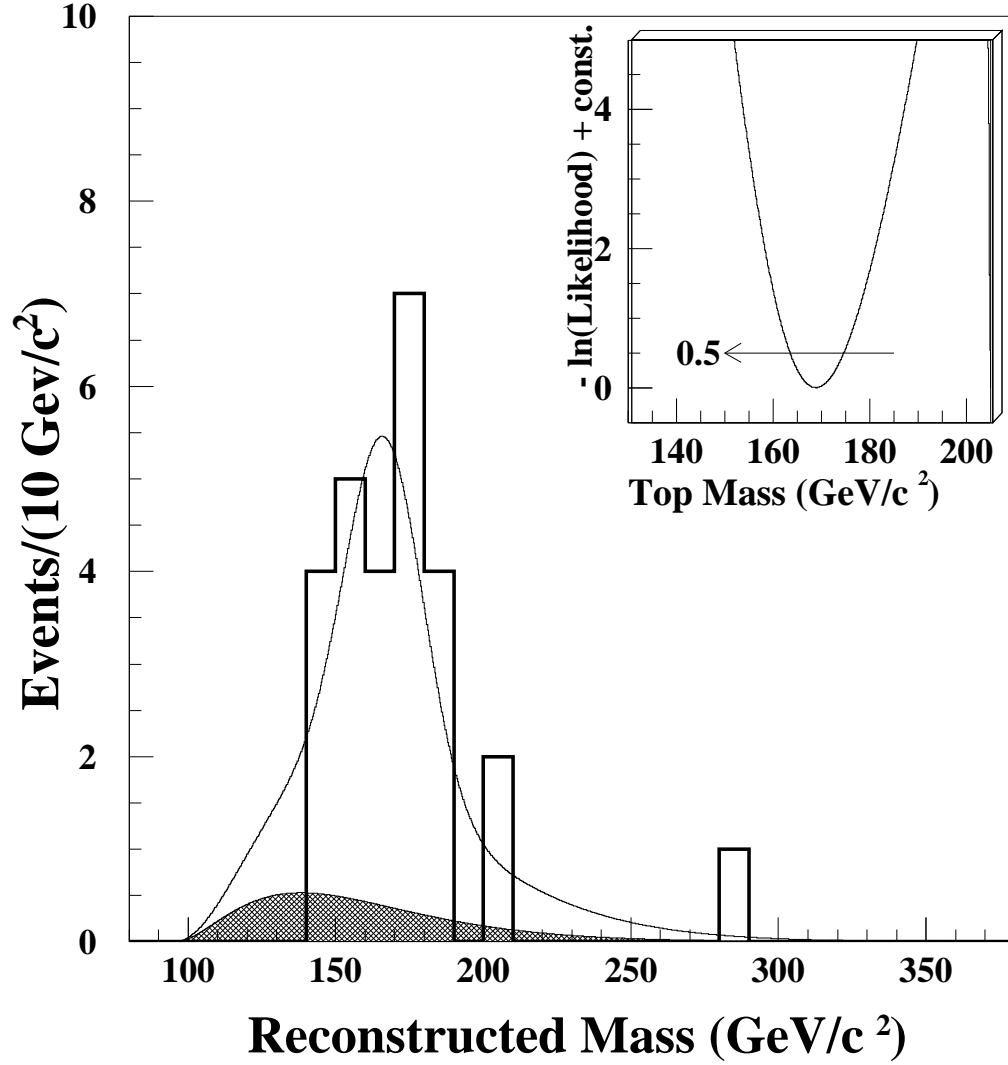


Figure B.1: Results of the  $\mathcal{L}^{**}$  likelihood fit to 27  $b$ -tagged events (histogram). The shaded area corresponds to the background returned by the fit ( $5.2 \pm 1.4$ ) and the smooth line is the sum of fitted signal and background contributions. The inset shows the shape of the  $-\log \mathcal{L}^{**}$  versus top mass from which we extract the fitted top quark mass and background contribution.

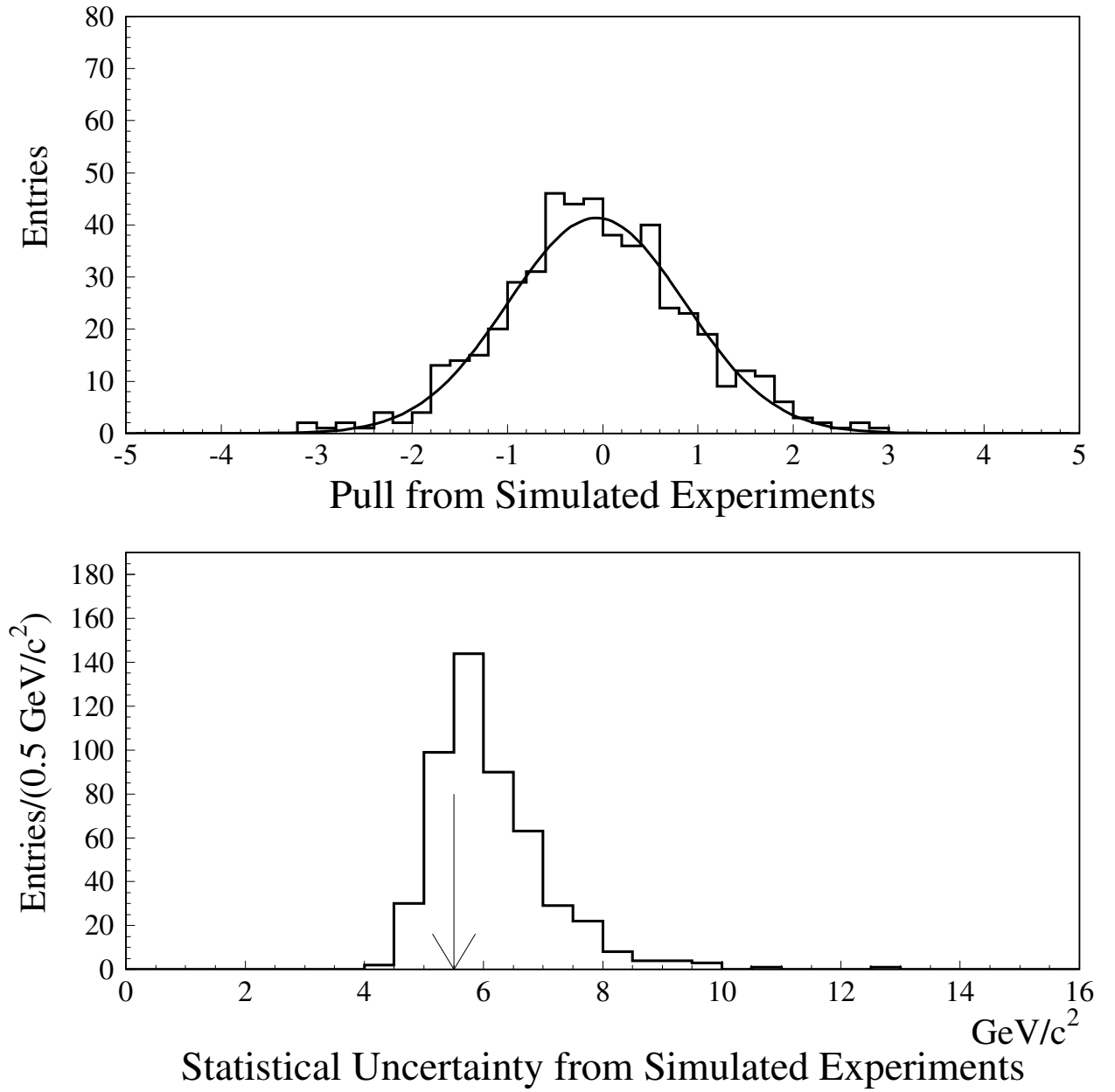


Figure B.2: Results from 500 simulated experiments using the  $\mathcal{L}^{**}$  likelihood technique. Each simulated experiment consists of 27 events, as in the data sample. The upper figure shows the pull distribution between the fitted top mass and the input value ( $175 \text{ GeV}/c^2$ ), and the bottom figure shows the average statistical uncertainty on the fitted top mass as returned by the likelihood procedure. The arrow represents the measured value in the data sample.

## B.2 Fitting double $b$ -tagged events

This analysis considers only events which contain two  $b$ -tagged jets [73]. To increase the acceptance for double  $b$ -tagged events beyond what the SVX and SLT algorithms provide, we allow one of the  $b$  jets to be tagged by the JPB algorithm. Because the JPB variable depends upon the impact parameters of the tracks in the jet with respect to the primary interaction vertex, this algorithm is correlated with the SVX tagging algorithm. We expect little or no correlation between the JPB and SLT tagging algorithms. We consider a jet  $b$ -tagged if it has a JPB value less than 5%.

Events are selected using the same selection criteria described in Section 3. After we apply analysis cuts 1–7 from Section 3.3 and require that two jets are tagged by at least one of the three  $b$ -tagging algorithms, the data sample consists of 11 events. Monte Carlo simulations showed that the resolution on the measured top quark mass can be improved by requiring the invariant mass of the two untagged jets to be near the  $W$ -boson mass. A cut of  $60 < M_{jj} < 100 \text{ GeV}/c^2$  was found to yield the lowest uncertainty on the measured top quark mass. Nine of the eleven events are found to survive the  $W$  mass cut. The nine events are a subset of the sample of 34 tagged events. The reconstructed top masses of these nine events are listed in Table B.2 and are shown in Figure B.3.

The expected backgrounds are estimated to be  $0.22 \pm 0.08$  events from  $Wb\bar{b} + Wc\bar{c}$  processes,  $0.05 \pm 0.02$  events from non- $W$  background (e.g.  $b\bar{b}$  production), and  $0.13 \pm 0.05$  events for non-heavy flavor background such as  $WW$  and  $WZ$  processes. The total number of background events is then estimated to be  $0.4 \pm 0.1$ .

The method for evaluating the top quark mass from this data sample is the same as the procedure discussed in Section 7. The results of the fit are shown in Fig. B.3. The figure shows the mass distribution obtained from data

overlayed with the fitted results from the Monte Carlo simulation. The inset shows the distribution of  $-\Delta \log \mathcal{L}$  as a function of the top mass for the nine data events.

The evaluation of systematic uncertainties are carried out in a similar manner to that which was discussed in Section 9. The results are shown in Table B.3. The uncertainty due to background shape is appreciably reduced compared to the four subsample analysis because of the smaller background fraction.

Using the techniques described in this section on the nine double tagged events, we measure the top quark mass to be  $171.8 \pm 7.2(\text{stat.}) \pm 4.3(\text{syst.})$  GeV/ $c^2$ . This measurement is consistent with the results presented in Section 8.

Run	Event	Tags	Di-jet mass (GeV/ $c^2$ )	Top mass (GeV/ $c^2$ )
40758	44414	SVX + SVX	83.9	175.4
59698	31639	SVX + (SLT & JPB)	79.5	187.4
63247	65096	SVX + JPB	81.3	161.0
64721	229200	SLT + SLT	81.6	181.0
65298	747402	SLT + JPB	60.0	149.4
65581	322592	(SVX & SLT) + SVX	66.2	152.7
67824	281883	(SVX & SLT) + SVX	73.3	170.1
67971	55023	SVX + SVX	98.1	183.5
68464	547303	SVX + SVX	87.3	151.1

Table B.2: List of events used in the double  $b$ -tagged analysis. Shown are the run-event numbers, the algorithms which tagged the two jets, the di-jet mass of the two untagged jets, and the reconstructed top mass for the solution having the lowest  $\chi^2$ . If a jet is tagged by two different algorithms, both tags appear in parentheses.



Systematic uncertainties	Values ( $\text{GeV}/c^2$ )
Jet energy measurement	4.1
Initial and final state radiation	1.1
Shape of background spectrum	$<0.1$
$b$ -Tagging	0.4
Parton distribution functions	0.3
Total	4.3

Table B.3: Summary of systematic uncertainties in the top mass measurement from double  $b$ -tagged events.

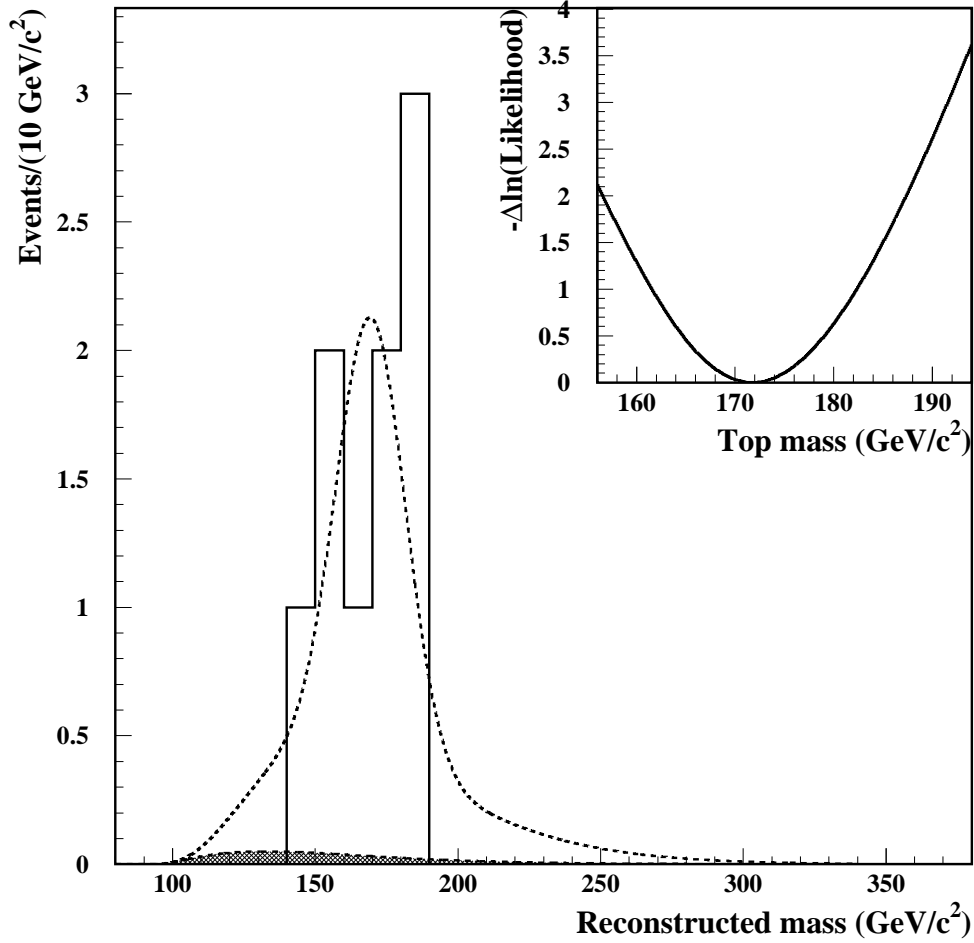


Figure B.3: Distribution of reconstructed mass for the nine data events and Monte Carlo simulation for the Double b-tag analysis. The background distribution (hatched) has been normalized to the expected background of 0.4 events. The sum of signal+background (dashed line) has been normalized to the fitted number of  $t\bar{t}$  and background. The inset shows the shape of the likelihood function versus the top quark mass, from which we extract the top quark mass to be  $171.8 \pm 7.2$  GeV/c<sup>2</sup>.

# Appendix C

## DETAILS OF THE ALL-HADRONIC AND DILEPTON MASS ANALYSES

### C.1 All-hadronic channel

A reevaluation of the systematic uncertainties on the measurement of the top quark mass in the all-hadronic channel as reported in Ref. [10] has shown that some of those estimates were overly conservative. Since that publication further studies of the systematic uncertainties have led to better procedures, which we now apply to all channels. The systematic uncertainties which have been revised include: initial and final state radiation, fitting procedure, and jet energy scale. These revisions are discussed below.

The contribution due to uncertainty in modeling initial and final state hard radiation was  $8.0 \text{ GeV}/c^2$ . To evaluate this uncertainty, standard HERWIG  $t\bar{t}$  events were compared to samples which were constructed to have smaller and larger fractions of events in which one or more of the final state jets did not match any of the daughter quarks from the  $t\bar{t}$  decay. The most

evident difference between the samples was that the width of the reconstructed mass distribution broadened as this fraction increased. On the other hand, simulated experiments showed only a very small shift in the fitted top quark mass. The systematic uncertainty was evaluated as follows. We generated two samples of simulated experiments, (a) one using the default HERWIG templates, and (b) one using templates which were constructed to have 90% of events containing one or more jets that were not matched to the daughter quarks from the  $t\bar{t}$  decay. For the default HERWIG sample, approximately 60% of events have one or more jets not matched to a quark from the  $t\bar{t}$  decay. In both cases, we evaluated the median and the rms width of fitted top quark masses from the simulated experiments. The systematic uncertainty was taken to be the quadrature difference of the widths between samples (a) and (b). This number was then added in quadrature with the small shift in the median mass which was observed between sample (a) and (b). Essentially all of the  $8.0 \text{ GeV}/c^2$  uncertainty was from the increase in the width of the distribution of sample (b). Further studies show that the change in width of the reconstructed mass distribution with increased radiation is reflected in the statistical uncertainties returned by the fits for simulated experiments; thus the statistical uncertainty obtained from our fitting procedure for the data sample already takes into account this effect. A reevaluation, using the same procedure as described in Section 9.2, results in a contribution from this source of  $1.8 \text{ GeV}/c^2$  [62].

Another large source of systematic uncertainty ( $5.2 \text{ GeV}/c^2$ ) came from the effect of selecting the second-best rather than the best kinematic fit to each event. A smaller contribution came from considering different ways of interpolating between likelihood values at discrete top mass values in order to find the maximum likelihood point. A third contribution came from the finite Monte Carlo statistics that provided the expected reconstructed mass distributions at different top mass values. The first two contributions are no

longer identified as sources of significant systematic uncertainty since they concern the robustness of the chosen method. The contribution from Monte Carlo statistics, of  $0.3 \text{ GeV}/c^2$ , remains.

The jet energy scale uncertainty was determined to be  $5.4 \text{ GeV}/c^2$ . Part of that ( $3.7 \text{ GeV}/c^2$ ), was due to differences in the calorimeter energy scale between two versions of the detector simulation. The source of this uncertainty was later corrected. As a result, the  $3.7 \text{ GeV}/c^2$  contribution to the uncertainty was eliminated.

A small reorganization of the contributions has occurred, which we mention in order to avoid any confusion in a comparison with Ref. [10]. The soft gluon uncertainty ( $3.0 \text{ GeV}/c^2$ ) has been moved from the “gluon radiation and fragmentation effects” to the “jet energy scale” category. The Monte Carlo generator uncertainty ( $0.8 \text{ GeV}/c^2$ ) has been assigned its own category. The result is a new systematic uncertainty of  $5.7 \text{ GeV}/c^2$ , with a breakdown into different contributions as listed in Table 10.1.

## C.2 Dilepton channel

The top quark mass measurement in the dilepton channel uses eight observed events that pass the standard selection criteria used for the dilepton channel [12, 62]. The criteria require that the leptons have opposite charges, that there be at least two jets per event, and include cuts on the missing transverse energy and the lepton transverse energies.

This measurement involves two steps: a top mass estimate is obtained for each event, and then a likelihood fit, which allows for the presence of background, gives an overall best estimate of the top quark mass. The second step is similar to that in the lepton+jets topology, but the first step is appreciably different.

In order to get a mass estimate for an individual event, we determine

a weight distribution as a function of an assumed top mass,  $m_t$ . First, we assume that the event originates from  $t\bar{t}$  production and decay, that the leading two jets are  $b$  jets from top decay, and that the leptons ( $e$  or  $\mu$ ) are from associated  $W$ -boson decays. Next, we assume a value for the top mass,  $m_t$ , assume pseudorapidity values,  $\eta_1$  and  $\eta_2$ , for the two neutrinos, and solve for the two neutrino momenta. In general there are eight solutions because of a quadratic ambiguity in each neutrino's longitudinal momentum and a choice of pairing leptons with jets. For each solution, we denote as  $\not{E}_T^p$  the vector sum of the solution's neutrino transverse momenta. Then we assign a weight to each solution according to how well  $\not{E}_T^p$  agrees with the event's measured missing transverse energy,  $\not{E}_T^m$ , as follows:

$$g(m_t, \eta_1, \eta_2) = \exp\left(-\frac{(\not{E}_{Tx}^p - \not{E}_{Tx}^m)^2}{2\sigma^2}\right) \times \exp\left(-\frac{(\not{E}_{Ty}^p - \not{E}_{Ty}^m)^2}{2\sigma^2}\right) \quad (\text{C.1})$$

where  $\sigma$  is the resolution in each component (x and y) of the measured unclustered transverse energy (see below). The experimental resolution in jets and leptons is taken into account by sampling the measured quantities many times according to their resolutions. That is, for each set of assumed  $m_t$ ,  $\eta_1$  and  $\eta_2$  values a weight is calculated many times, and the sum is accumulated. For each assumed  $m_t$  value, 100 pairs of  $\eta_1$  and  $\eta_2$  values are assumed in turn, and the summed weights are again summed, to give a final summed weight,  $f(m_t)$ , at any  $m_t$  value. The  $\eta_1$  and  $\eta_2$  values are drawn independently from a Gaussian distribution with unit width and centered at 0.0, as predicted by HERWIG Monte Carlo simulations. Thus all the uncertainties on the  $\not{E}_T$  measurement are taken into account, except for the resolution of the unclustered energy. We use  $\sigma = 4\sqrt{n}$  GeV, where  $n$  is the number of interactions in the event and comes from studies of low-luminosity minimum-bias events.

For each event,  $m_t$  values in the range 90 to 290 GeV/ $c^2$ , in 2.5 GeV/ $c^2$  steps, were assumed in order to give a  $f(m_t)$  distribution. This distribution is used to determine a top mass estimate, as follows. The position of

the maximum value,  $f(m_t)_{max}$ , is denoted by  $M_{max}$ . The first points on either side of  $M_{max}$  that have  $f(m_t) \leq f(m_t)_{max}/2$  are denoted by  $M_1$  and  $M_2$ . The average of  $M_1$  and  $M_2$  is taken as the top mass estimate.

The  $f(m_t)$  distributions, normalized to unity, for the eight events are shown in Fig. C.1. The eight events, with their lepton identifications, numbers of jets (with uncorrected transverse energy greater than 10 GeV and pseudo-rapidity in the range  $-2.0$  to  $+2.0$  units), and estimated top masses are given in Table C.1.

Run	Event	leptons	$N_{jet}$	Top mass	$\log(P_{ev})$
41540	127085	$e^- \mu^+$	2	158.8	0.47
45047	104393	$e^+ \mu^-$	2	180.0	1.82
47122	38382	$e^+ \mu^-$	2	176.3	1.40
57621	45230	$e^+ \mu^-$	2	156.3	2.20
66046	380045	$e^+ \mu^-$	4	172.5	-5.20
67581	129896	$e^+ \mu^-$	2	143.8	0.44
68185	174611	$e^+ e^-$	2	161.3	4.10
69808	639398	$e^- \mu^+$	3	170.0	3.50

Table C.1: Information on the eight candidate dilepton events used in the dilepton mass analysis. Shown are: the run and event numbers, the types of leptons in each event, the number of reconstructed jets (with uncorrected  $P_T > 10$  GeV/ $c$  and  $|\eta| < 2$ ), and the top mass estimates for each event. Also listed is  $\log(P_{ev})$ , where  $P_{ev}$  is the sum of all the weights for the event divided by the number of resolution samplings used.

It is useful to define a variable,  $P_{ev}$ , as the sum of  $f(m_t)$  over all assumed  $m_t$  values, divided by the number of resolution samplings used. The latter number is 1500 for data and 30 for Monte Carlo events. This variable gives an indication of how easily an event can be fit to the  $t\bar{t}$  decay hypothesis. The  $\log(P_{ev})$  distribution of simulated  $t\bar{t}$  plus background events is shown in Figure C.2. The  $t\bar{t}$  events are from the HERWIG simulation with a top quark mass of 175 GeV/ $c^2$ . The  $\log(P_{ev})$  values for the eight observed events are

listed in Table C.1 and are indicated by arrows in Figure C.2. The data points all lie within the range spanned by the simulated distribution. In the simulated events, 0.7% have  $\log(P_{ev}) < -5.2$ , the value for the lowest data point, so the probability for an eight-event sample to have at least one event at  $-5.2$  or lower is 5%.

In Ref. [62] it was noted that the same method could be applied to events in the lepton+jets topology that had two SVX-tagged jets. In such events the two untagged jets (of the four highest  $E_T$  jets) are assumed to result from  $W$ -boson decay, and in order to mimic a  $W$ -boson leptonic decay one of those jets is treated as a lepton (electron or muon) and the other as a neutrino. In the following we took the jet with lower  $E_T$  as an unobserved neutrino and recalculated  $\cancel{E}_T^m$  for the event. Then the above dilepton method was applied.

The five events in the SVX Double sample were fit with this method. A top quark mass value of  $181.5 \pm 12.6 \text{ GeV}/c^2$  was obtained. This value has to be compared with the value shown in Table 8.1 of  $170.0_{-8.9}^{+9.4} \text{ GeV}/c^2$ , a difference of  $11.5 \text{ GeV}/c^2$ . In order to understand the difference between the two methods a comparison was made in a Monte Carlo study that used a sample of approximately 1300 simulated lepton+jets  $t\bar{t}$  events with  $M_{top} = 175 \text{ GeV}/c^2$  and with two jets having SVX tags. The distribution of the reconstructed mass from the standard lepton+jets kinematic fit is shown in Figure C.3(a). Also shown is the top mass estimate per event with the pseudo-dilepton method described above. The two distributions are similar. The medians are  $170.5 \text{ GeV}/c^2$  and  $170.9 \text{ GeV}/c^2$ , and the widths are  $21.4 \text{ GeV}/c^2$  and  $23.4 \text{ GeV}/c^2$ , respectively for the kinematic fit and the dilepton methods. Here the widths are one-half the separation of the 16<sup>th</sup> and 84<sup>th</sup> percentiles in the distributions. As expected, the dilepton method gives a slightly wider distribution. In Figure C.3(b) the mass difference between the two methods is plotted for each event. The width of this distribution is  $24.3 \text{ GeV}/c^2$ . This



shows that the shift of  $11.5 \text{ GeV}/c^2$  found for the five SVX Double events using the two methods is well within expectation.

This study shows that fitting the dilepton events, which are underconstrained, using the technique described here is just as valid and precise as the completely constrained 2-C fit used for the lepton+jets sample. In addition, if we calculate the statistical correlation between the two methods, we obtain a correlation coefficient of 0.36, i.e., fitting the SVX Double events with this technique could improve the statistical uncertainty on the mass determination from this channel.

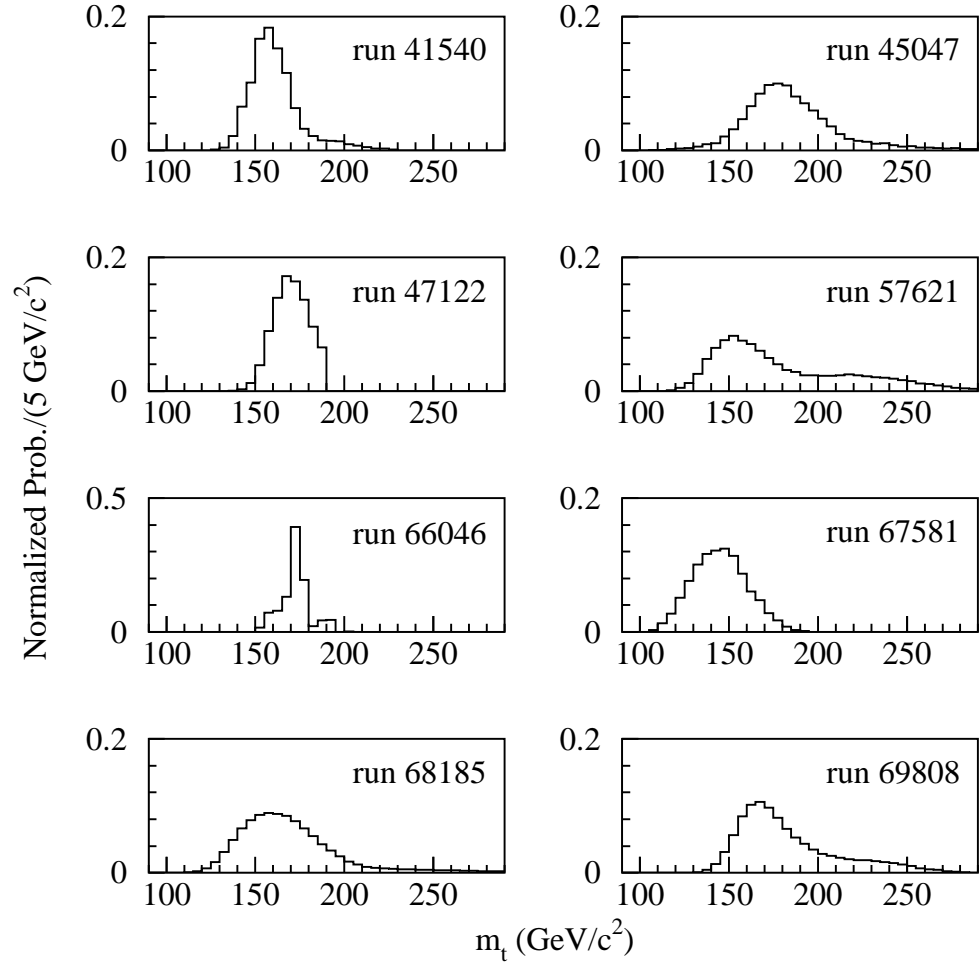


Figure C.1: Weight distribution  $f(m_t)$ , normalized to unity, for the eight observed dilepton events.

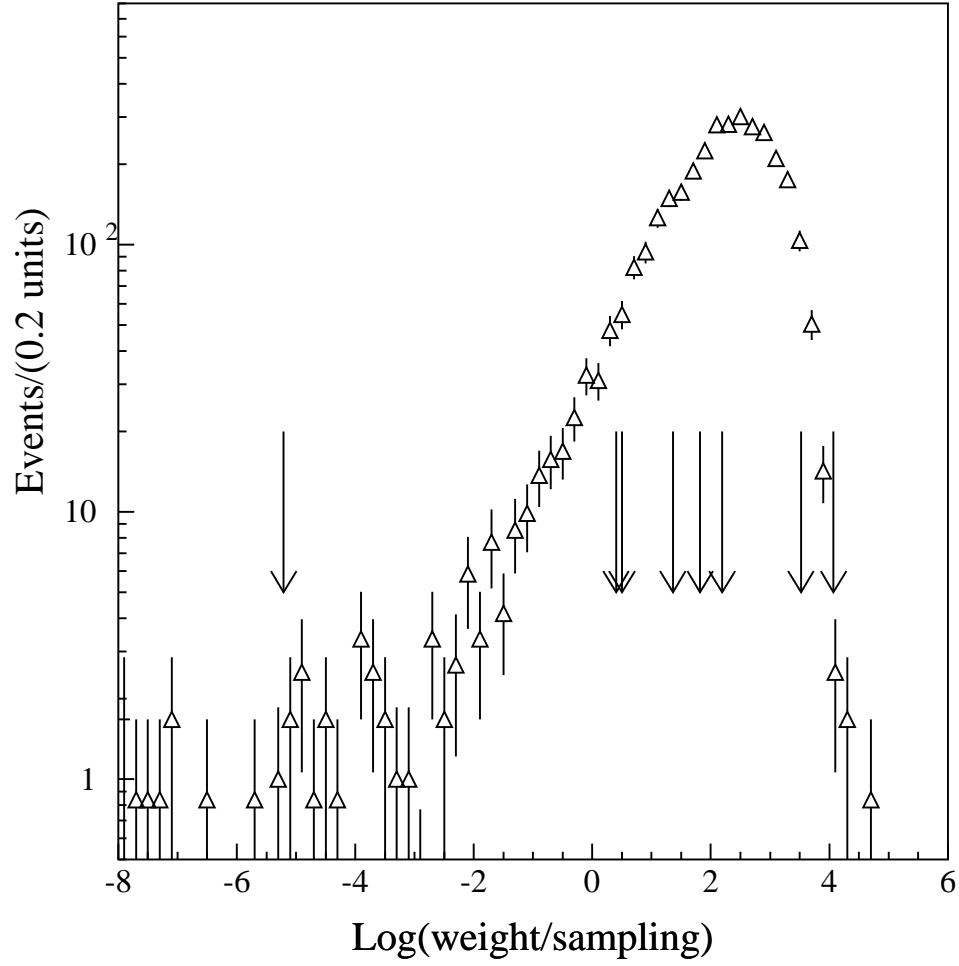


Figure C.2: Predicted distribution of  $\log(P_{ev})$ , the total weight sum per resolution sampling, for the expected  $t\bar{t}$  and background event mix in the dilepton sample. The arrows indicate the values for the eight observed events.

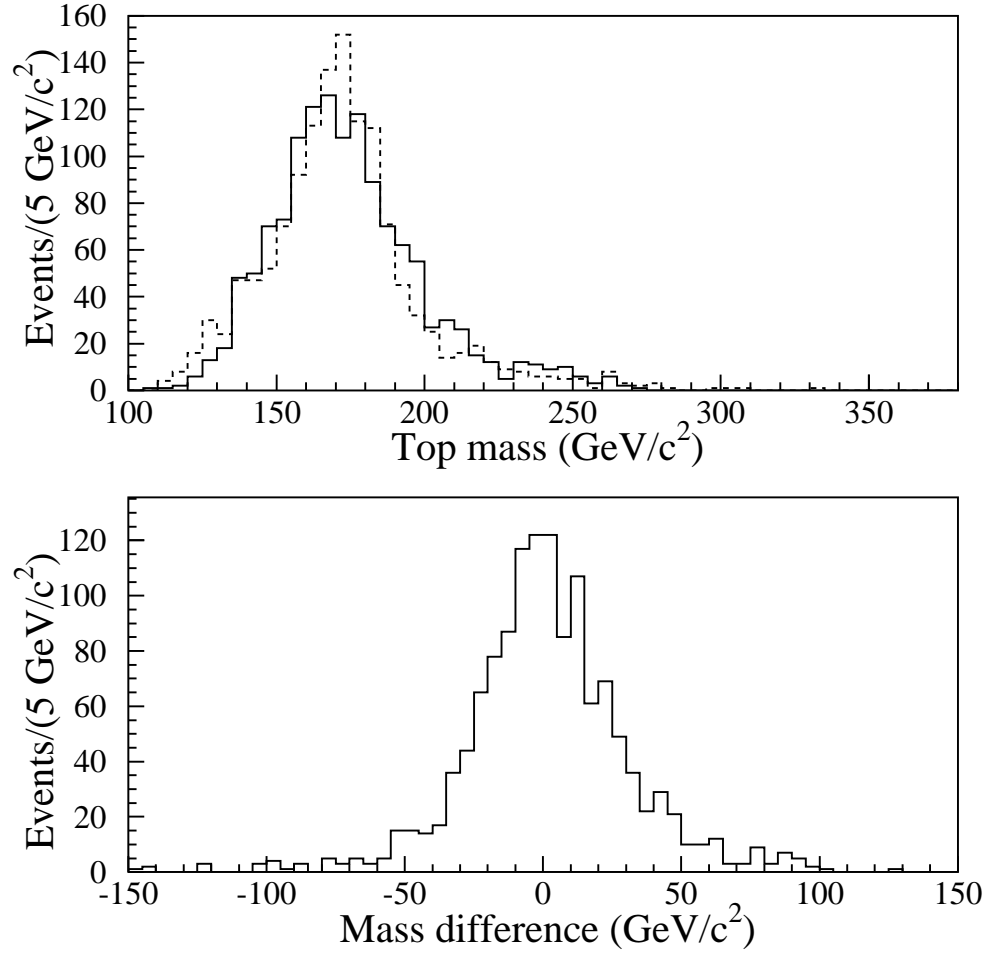


Figure C.3: (a) Top mass estimates for simulated  $t\bar{t}$  events (top mass 175  $\text{GeV}/c^2$ ) with two SVX tags using the lepton+jets kinematic fit (dashed) and the pseudo-dilepton (solid) methods. (b) The difference per event between the top mass estimates from the two methods.

# REFERENCES

- [1] F. Abe *et al.*, Phys. Rev. D **50**, 2966 (1994); Phys. Rev. Lett. **73**, 225 (1994).
- [2] F. Abe *et al.*, Phys. Rev. Lett. **74**, 2626 (1995).
- [3] S. Abachi *et al.*, Phys. Rev. Lett. **74**, 2632 (1995).
- [4] F. Abe *et al.*, Phys. Rev. Lett. **75**, 3997 (1995); F. Abe *et al.*, Phys. Rev. D. **51**, 4623 (1995).
- [5] S. Abachi *et al.*, Phys. Rev. Lett. **79**, 1197 (1997).
- [6] F. Abe *et al.*, Phys. Rev. Lett. **80**, 2767 (1998).
- [7] F. Abe *et al.*, Phys. Rev. Lett. **80**, 2773 (1998).
- [8] S. Abachi *et al.*, Phys. Rev. Lett. **79**, 1203 (1997).
- [9] F. Abe *et al.*, Phys. Rev. D. **59**, 092001 (1999).
- [10] F. Abe *et al.*, Phys. Rev. Lett. **79**, 1992 (1997).
- [11] B. Abbott *et al.*, Phys. Rev. Lett. **83**, 1908 (1999); Phys. Rev. D **60**, 012001 (1999).
- [12] F. Abe *et al.*, Phys. Rev. Lett. **80**, 2779 (1998).
- [13] B. Abbott *et al.*, Phys. Rev. Lett. **80**, 2063 (1998).

- [14] M. Jezabek and J.H. Kuhn, Phys. Rev. D **48**, 1910 (1993); Erratum, *ibid.* **49**, 4970 (1994).
- [15] I.I. Bigi, Yu L. Dokshitzer, V.A. Khoze, J.H. Kuhn, and P. Zerwas, Phys. Lett. B **181**, 157 (1986).
- [16] S.L. Glashow, Nucl. Phys. **22**, 579 (1961); S. Weinberg, Phys. Rev. Lett. **19**, 1264 (1967); A. Salam, in *Elementary Particle Theory: Relativistic Groups and Analyticity (Nobel Symposium No. 8)*, edited by N. Svartholm (Almqvist and Wiksell, Sweden, 1968), p. 367.
- [17] The LEP Collaborations, the LEP Electroweak Working Group and the SLD Heavy Flavor and Electroweak Groups, CERN-EP/99-15 (1999).
- [18] F. Abe *et al.*, Phys. Rev. Lett. **79**, 3835 (1997).
- [19] F.Abe *et al.*, Nucl. Instrum. Methods **A271**, 387 (1988).
- [20] F. Bedeschi *et al.*, Nucl. Instrum. Methods **A268**, 50 (1988).
- [21] The pseudo-rapidity  $\eta$  is defined as  $-\log(\tan(\theta/2))$ , where  $\theta$  is the polar angle measured relative to the positive  $z$ -axis (taken as the direction of the outgoing proton beam) assuming a  $z$ -vertex position of zero. For the mass fit discussed in Section 6 we recalculate  $\eta$  using the measured  $z$ -vertex position for each event.
- [22] F. Snider *et al.*, Nucl. Instrum. Methods **A268**, 75 (1988). This is the reference for the previous generation of the device. The replacement for the Run 1 data sample has more modules, each with a shorter drift length but is otherwise similar.
- [23] F. Abe *et al.*, Phys. Rev. Lett. **76**, 3070 (1996).
- [24] P. Azzi *et al.*, Nucl. Instrum. Methods **A360**, 137-140 (1995), for Run 1b. D. Amidei *et al.*, Nucl. Instrum. Methods **A350**, 73-130 (1994); D.

- Amidei *et al.*, Nucl. Instrum. Methods **A342**, 251-259 (1994); C. Haber *et al.*, Nucl. Instrum. Methods **A289**, 388 (1990); for Run 1a.
- [25] G. Ascoli *et al.*, Nucl. Instrum. Methods **A268**, 33 (1988); G. Ascoli *et al.*, Nucl. Instrum. Methods **A268**, 41 (1988).
- [26] L. Balka *et al.*, Nucl. Instrum. Methods **A267**, 272 (1988); S. R. Hahn *et al.*, Nucl. Instrum. Methods **A267**, 351 (1988); K. Yasuoka *et al.*, Nucl. Instrum. Methods **A267**, 315 (1988); R. G. Wagner *et al.*, Nucl. Instrum. Methods **A330**, 272 (1988); T. Devlin *et al.*, Nucl. Instrum. Methods **A267**, 24 (1988).
- [27] S. Bertolucci *et al.*, Nucl. Instrum. Methods **A267**, 301 (1988).
- [28] The unclustered energy consists of the total energy which is not contained in jets with  $E_T > 8$  GeV and  $|\eta| < 3.4$ .
- [29] The missing  $E_T$ ,  $\cancel{E}_T$  is defined to be the magnitude of the vector sum of the raw transverse energies in all calorimeter towers with  $|\eta| < 3.6$ . Only towers which exceed a detector-dependent energy threshold are included in the sum [1].
- [30] A fiducial lepton is required to be within a well-understood region of the CEM which allows for good lepton identification.
- [31] F. Abe *et al.*, Phys. Rev. D **52**, 4784 (1995); F. Abe *et al.*, Phys. Rev. Lett. **75**, 11 (1995).
- [32] The isolation,  $I$ , is defined as the  $E_T$  ( $P_T$ ) within a cone of  $\Delta R < 0.4$  centered on the lepton, but excluding the lepton energy, divided by the  $E_T$  ( $P_T$ ) of the lepton.
- [33] F. Abe *et al.*, Phys. Rev. D **45**, 1448 (1992).
- [34] D. Kestenbaum, Ph.D. Thesis (unpublished), Harvard University (1996).

- [35] F. Abe *et al.*, Phys. Rev. Lett. **73**, 2662 (1994).
- [36] K. Tollefson, Ph.D. Thesis (unpublished), University of Rochester (1997).
- [37] A.D. Martin, R.G. Roberts, and W.J. Stirling, Phys. Lett. B **306**, 145 (1993).
- [38] P. Avery, K. Read, G. Trahern, Cornell Internal Note CSN-212, March 25, 1985 (unpublished). We use Version 9.1 with a  $b$  lifetime of 1.45 ps.
- [39] G. Marchesini and B.R. Webber, Nucl. Phys. **B310**, 461 (1988); G. Marchesini *et al.*, Comput. Phys. Comm. **67**, 465 (1992).
- [40] T. Sjöstrand, Computer Physics Commun. **39**, 347 (1986) ; T. Sjöstrand and M. Bengtsson, Computer Physics Commun. **43**, 367 (1987); T. Sjöstrand and M. Bengtsson, Computer Physics Commun. **46**, 43 (1987).
- [41] F. Paige and S.D. Protopopescu, BNL Report No. 38034, 1986 (unpublished).
- [42] F.A. Berends, W.T. Giele, H. Kuijf and B. Tausk, Nucl. Phys. **B357**, 32 (1991).
- [43] J. Benlloch, Proceedings of the 1992 DPF Meeting, 10-14 Nov., 1992, Batavia, IL, ed. C.H. Albright *et al.*, World Scientific, (1993) p. 1091.
- [44] F. Abe *et al.*, Phys. Rev. Lett. **79**, 4760 (1997).
- [45] F. Ptohos (for the CDF Collaboration), Proceedings of the International Europhysics Conference on High Energy Physics 99, Tampere, Finland, July 17, 1999.
- [46] J. Ohnemus and J. F. Owens, Phys. Rev. D **43**, 3626 (1991).



- [47] T. Stelzer, Z. Sullivan and S. Willenbrock, Phys. Rev. D **58**, 3626 (1998);  
T. Stelzer, Z. Sullivan and S. Willenbrock, Phys. Rev. D **56**, 5919 (1997);  
T. Stelzer and S. Willenbrock, Phys. Rev. D **54**, 6696 (1996); T. Stelzer  
and S. Willenbrock, Phys. Lett. B **357**, 125 (1995).
- [48] Raw jet energies are the observed values after performing the jet cluster-  
ing, but prior to any corrections. The raw jet energies are used to select  
the data samples and are used in defining the four highest  $E_T$  jets.
- [49] F. Abe *et al.*, Phys. Rev. D **47**, 4857 (1993).
- [50] F. Abe *et al.*, Phys. Rev. Lett. **77**, 438 (1996).
- [51] P. Bagnaia *et al.*, Phys. Lett. **144B**, 283 (1984).
- [52] M. Lancaster, Proceedings of “Les Rencontres de Physique de la Vallée  
d’Aoste”, La Thuile, March 1997, ed. M. Greco.
- [53] MINUIT Reference Manual, CERN Program Library Entry **D506**, 1994.
- [54] O. Dahl, T. Day, F. Solmitz and N. Gould, Lawrence Berkeley Lab, Al-  
varez Group Programming Note P-126 (1968).
- [55] F. Abe *et al.*, Phys. Rev. Lett. **74**, 341 (1995).
- [56] L. Orr, T. Stelzer, and W. J. Stirling, Phys. Rev. D **52**, 124 (1995); Phys.  
Lett. B **354**, 442 (1995).
- [57] S. Bettelli, Ph.D. Thesis (unpublished), University of Pisa (1996).
- [58] N. Eddy, Ph.D. Thesis (unpublished), University of Michigan (1998).
- [59] G. Altarelli and G. Parisi, Nucl. Phys. **B126**, 298 (1977); Yu L. Dok-  
shitzer, Sov. Phys. JETP **46**, 641 (1977); V. N. Gribov and L. N. Lipatov,  
Sov. J. Nucl. Phys. **15**, 438 (1972).

- [60] H. L. Lai *et al.*, Phys. Rev. D **55**, 1280 (1997).
- [61] F. Abe *et al.*, Phys. Rev. D **50**, 5562 (1994).
- [62] F. Abe *et al.*, Phys. Rev. Lett. **82**, 271 (1999); Erratum *ibid.* **82**, 2008E (1999).
- [63] K. Kondo, J. Phys. Soc. Jpn. **57** 4126 (1988); *ibid.* **60**, 836 (1991).
- [64] E. W. Varnes, Ph.D. Thesis (unpublished), University of California, Berkeley (1997).
- [65] Particle Data Group, C. Caso *et al.*, Eur. Jour. Phys C **3**, 1 (1998), p. 173.
- [66] B. Abbott *et al.*, Phys. Rev. D **60**, 052001 (1998).
- [67] L. Demortier, R. Hall, R. Hughes, B. Klima, R. Roser and M. Strovink, Fermilab Report No. FERMILAB-TM-2084 (1999).
- [68] M. Lanzoni, University of Pisa Thesis (unpublished) (1996).
- [69] D. Buskulic *et al.*, Phys.Lett. B **313**, 535 (1992).
- [70] F. Abe *et al.*, Phys. Rev. D **53**, 1051 (1996).
- [71] D.Buskulic *et al.*, Phys. Lett. B **284**, 177 (1992); P.Abreu *et al.*, Phys. Lett. B **322**, 459 (1994); R.Akers *et al.*, Phys. Lett. B **327**, 411 (1994).
- [72] Monte Carlo studies showed that the jet probability distributions for light quark and gluon jets were similar, so that a single non-*b* probability distribution was used.
- [73] S. Aota, Ph.D. Thesis (unpublished), University of Tsukuba (1997).